

Ca_v3.2 T-type calcium channels modulate burst firing of mature
granule cells of the dentate gyrus

Dissertation

zur Erlangung des akademischen Grades

doctor rerum naturalium (Dr. rer. nat.)

genehmigt durch die Fakultät für Naturwissenschaften der Otto-von-
Guericke-Universität Magdeburg

von M. Sc. Maël Florent Duméniou

geb. am 21/04/1989 in Le Creusot, Frankreich

Gutachter: Prof. Dr. Eckart D. Gundelfinger

Prof. Dr. Josef Bischofberger

eingereicht am: 21/06/2017

verteidigt am: 19/04/2018

Acknowledgements

First of all, I would like to thank the Leibniz Institute for Neurobiology for granting me a Ph.D. fellowship and offering a pleasant working environment.

Thanks to Dr. Jeffrey López Rojas, Dr. Arthur Bikbaev, Dr. Michael R. Kreutz and Dr. Martin Heine for being accessible and concerned supervisors.

In this regard, I would like to further thank Dr. Jeffrey López Rojas, a truly dedicated scientist and a nice human being. This thesis would not have been possible without him. I respectfully salute him and wish him a successful career and a happy personal life. Many thanks as well to Dr. Arthur Bikbaev for actively participating in the success of this thesis. I enjoyed our enriching scientific discussions and additionally enriching verbal jousts. I wish him a happy russian life.

Thanks to Dr. Oleg Senkov for its friendly guidance during *in vivo* and behavioural experiments and its great help in designing, building and implanting *in vivo* recordings apparatus. I wish him as well a successfully career as a team leader. Further thanks to Dr. Andrey Mironov for providing additional help in implanting *in vivo* recordings apparatus.

Thanks to Dr. Martin Heine and Dr. Yulia Klyueva for advising me on specific technical issues.

Thanks to Dr. Emanuel Bourinet for kindly providing me with TTA-A2 and Ca_v3.2 KO mice and for welcoming me in Montpellier.

Thanks to Monika Marunde for technical support.

Thanks to Christina Spilker and animals' caretakers for taking an active care of my mice.

Thanks to Prof. Dr. Eckart Gundelfinger, for being a friendly and accessible director and for reviewing my Dissertation. In this regard, thanks as well to Dr. Arthur Bikbaev Dr. Martin Heine and Dr. Michael R. Kreutz for achieving the thesis revision.

I would like to thank all my colleagues and friends whose I enjoyed the company or who provided appreciated support when I was in need: Dr. Anna Karpova, Dr. Camilla Fusi, Dr. Carolina Montenegro, Dr. Daniela Asenova Ivanova, Eneko Antonio Pina, Gonca Bayraktar, Dr. Guilherme Kaiowá Gomes, Ioana Butnaru, Jeet Singh, Jennifer Heck, Dr. Johannes Hradsky, Jose Francisco Alfaro Sanchis, Katarzyna Maria Grochowska, Kritika Sudan, Dr. Maria Andres-Alonso, Marie Oulé, Marta Brocka, Dr. Michelle Melgarejo da Rosa, Dr. Mohamed "Al-Tunisi" Raafet Ammar, Dr. Pegah Azizi, Dr. Pingan Yuanxiang, Dr. Rahul Kaushik, Dr. Rajeev Raman, Sandra Fienko, Dr. Soumee Bhattacharya, Yaime Pérez Rivas, Zeynep Öztan and many more.

Finally, I would like to thank my mom and my parents for maintaining me alive by keeping me under constant perfusion of greetings cards, food and gifts trough the Deutsche Post.

I dedicate this thesis to my maternal grandparents, inspirational figures of courage and resilience in the face of adversity.

Summary

Dentate gyrus granule cells (DGGCs) convey sensory information from the layer II of the entorhinal cortex to the CA3 subfield of the hippocampus and underlie neuronal processing critical for hippocampal function. Because of adult neurogenesis, the global population of DGGCs at a certain time point of an adult animal's life is composed of a heterogeneous mix of newborn, immature granule cells (iGCs) and older, mature GCs (mGCs). iGCs and mGCs exhibit strong differences in their structural, molecular and electrophysiological characteristics. iGCs, which compose around 10% of the total DGGC population, are seen as highly excitable due to their high input resistance and enhanced sensitivity to synaptic plasticity. On the other hand, the more abundant mGCs (the remaining 90% of all DGGCs) have intrinsic electrical properties such as low input resistance, strong dendritic voltage attenuation and hyperpolarized resting potential that make them seemingly weakly excitable. Because of these features, it remains intriguing how mGCs can actively participate in DG function. In this thesis, I explored the impact of T-type low-voltage activated calcium channels, notably the $Ca_v3.2$ isoform, in regulating mGCs firing properties. The three T-type channel isoforms $Ca_v3.1$, $Ca_v3.2$, and $Ca_v3.3$ are expressed in the DG, with $Ca_v3.2$ being the most abundant. T-type channels are permeable to calcium and thus can have a double effect on neuronal excitability upon activation: depolarization of the membrane and/or triggering of intracellular calcium signaling. They are preferentially active at negative potentials below -60 mV and have specific properties, including low voltage threshold for activation and small conductance. In addition, they quickly inactivate upon depolarization, leading to transient calcium current. A well-documented effect of T-type channels on neuronal excitability is to endow neurons with a stereotypical pattern of action potentials (APs) generation in the form of high-frequency bursts. Interestingly, T-type channels have been shown in brainstem interneurons to localize at the level of the axon initial segment, a position critical to control neuronal firing. More recently, it was also reported that T-type channels are present in the axon initial segment of mGCs, where they are implicated in cholinergic-induced modulation of M-type potassium channels and subsequent changes in AP threshold. Performing current-clamp recordings of mGCs from rodent hippocampal slices *in vitro*, I show a critical contribution of T-type channels to burst firing of these neurons in response to stimulation by somatic current injection. I provide evidence of T-type mediated calcium influx both in a region of the proximal axon, which corresponds to the position of the axon initial segment of mGCs, and in the dendrites. Local application of T-type blockers on this axonal domain resulted in impairment of the burst firing of mGCs, indicating that T-type channels at the axon initial segment are involved into control of burst generation. Analysis of the firing properties of mGCs from $Ca_v3.2$ KO mice allowed me to identify a crucial role of the $Ca_v3.2$ subtype in modulation of bursting. I also stimulated the medial perforant path and observed that stronger excitatory post-synaptic potentials (EPSPs) were required for mGCs from $Ca_v3.2$ KO mice to exhibit production of several APs in the timescale of a single EPSP (around 20 ms) as compared to WT. Finally, *in vivo* recording of local field potential and single unit activity in the DG and in CA3 of WT and $Ca_v3.2$ KO mice, done in collaborative work, revealed an impairment of neuronal activity in both structures in $Ca_v3.2$ KO mice, in a manner suggesting altered DG-CA3 communication. Based on my findings and on the existing literature, I propose a model in which T-type calcium channels localized at the level of the axon initial segment of mGCs support low-threshold generation of bursts of high-frequency APs, a mechanism compatible with both the low excitability of mGCs and the firing requirements to trigger CA3 pyramidal cells.

Zusammenfassung

Körnerzellen des Gyrus dentatus übermitteln sensorische Informationen aus dem entorhinalen Kortex in die CA3-Region des Hippokampus. Der Gyrus dentatus ist eine der wenigen Hirnregionen in denen Neurogenese auch nach der Entwicklung stattfindet. Daher finden sich im adulten Gehirn sowohl ausgereifte als auch neu geborene Körnerzellen. Beide Zellpopulationen unterscheiden sich nicht nur morphologisch sondern auch in ihren elektrophysiologischen Eigenschaften. Junge Körnerzellen, die ca. 10% der gesamten Population ausmachen, sind aufgrund ihres höheren Eingangswiderstands leichter erregbar und ihre synaptischen Eingänge sind leichter modifizierbar. Ausgereifte Körnerzellen hingegen zeigen einen niedrigeren Eingangswiderstand, eine stärkere Abschwächung der dendritischen Erregungsleitung und ein hyperpolarisierendes Ruhepotential, was in der Summe ihre Erregbarkeit deutlich vermindert. Daher stellt sich die Frage, welche Rolle diese Zellen für die Funktion des Gyrus dentatus spielen. In der vorliegenden Arbeit wurde der Einfluss von T-Typ-Kalziumkanäle auf die Eigenschaften von ausgereiften Körnerzellen hippocampaler Hirnschnitte untersucht. Alle drei T-Typ Kalziumkanäle, Cav3.1, Cav3.2, und Cav3.3, werden im Gyrus dentatus exprimiert, wobei Cav3.2 stärker exprimiert ist als die beiden anderen T-Typ Kalziumkanäle. Mit Hilfe von Patch-clamp-Experimenten wurde die Verteilung von T-typ Kalziumkanälen in gereiften Körnerzellen in hippocampalen Hirnschnitten untersucht. Wir konnten zeigen dass T-typ Kanäle für das Entladungsmuster dieser Neurone wichtig sind. Hier haben die $Ca_v3.2$ Kanäle einen Einfluss auf die initiale repetitive Entladung von Aktionspotentialen. Darüber hinaus wurde gefunden dass diese Kalziumkanäle im initialen axonalen Segment und in Dendriten lokalisiert sind. Die Kontrolle des Entladungsmusters wird durch $Ca_v3.2$ Kanäle die im initialen axonalen Segment zu finden sind mitbestimmt. Hier scheint der $Ca_v3.2$ Kanal eine zentrale Rolle zu spielen, was durch Experimente in Knockout Mäusen bestätigt wurde. In Zusammenarbeit konnten wir in vivo Ableitungen lokaler Feldpotentiale und sogenannter 'single units' im Gyrus dentatus und der CA3 Region des

Hippokampus durchgeführt. Hier konnte eine $Ca_v3.2$ spezifische Störung der neuronalen Aktivität nachgewiesen werden.

Basierend auf diesen Resultaten schlagen wir ein Modell vor, bei dem T-Typ Kalziumkanäle im axonalen initialen Segment von reifen Körnerzellen niedrigschwellige, hochfrequente Aktionspotentiale generieren und damit den Informationstransfer zu CA3 Pyramidenzellen beeinflussen.

Table of contents

1. Introduction	7
1.1. The dentate gyrus	7
1.2. DG-dependent neuronal processing, pattern separation and pattern completion	7
1.3. Dentate gyrus neurogenesis: mature and immature granule cells	10
1.4. A focus on the question of mGC-CA3 connectivity	13
1.5. Voltage-gated T-type channels and neuronal intrinsic excitability	14
1.6. T-type channels in the DG	17
1.7. Impact of T-type channels on iGCs and mGCs intrinsic excitability	17
1.8. Aims of the study	18
2. Materials and Methods	19
2.1. Materials	19
2.1.1. Chemicals	19
2.1.2. Equipment	20
2.1.3. Analysis software	21
2.1.4. Animals	21
2.2. Methods	21
2.2.1. <i>In vitro</i> single cells recordings	21
2.2.1.1. Hippocampal slices	21
2.2.1.2. Current-clamp whole-cell recordings	22
2.2.1.3. Pharmacology	22
2.2.1.3.1. T-type channel blockers	22
2.2.1.3.2. R and L-type channels blockers	23
2.2.1.3.3. Synaptic transmission blockers	23
2.2.1.3.4. Considerations on pharmacology preparation and use	23
2.2.1.4. Characterization of mGCs firing phenotype	24
2.2.1.4.1. Characterization of burst firing following somatic current injection	24
2.2.1.4.2. Quantification of the ADP and correlation with firing phenotype	24
2.2.1.4.3. Medial perforant path stimulation-driven activity	25
2.2.1.4.4. Local blockade of T-type channels	25
2.2.1.5. 2-photon imaging	26
2.2.1.6. <i>In vitro</i> data analysis	27
2.2.2. <i>In vivo</i> recordings of DG and CA3 activity and contextual fear conditioning	27
2.2.2.1. Animals housing and procedures	27
2.2.2.2. Design and fabrication of headstages	28
2.2.2.3. Fabrication of tetrodes	28
2.2.2.4. Implantation	28
2.2.2.5. Contextual fear conditioning	30
2.2.2.6. Local field potential and units' activity recordings	30
2.2.2.7. <i>In vivo</i> recordings analysis	31
2.2.2.7.1. Network activity	31
2.2.2.7.2. Units activity	31
3. Results	32
3.1. <i>In vitro</i> experiments	32
3.1.1. Introduction to T-type channel antagonists	32
3.1.2. mGCs exhibit low-threshold high frequency burst firing blocked by T-type channels antagonists	33
3.1.3. T-type channels blockers do not affect AP threshold	

	and overall mGCs excitability.....	36
3.1.4.	mGCs burst firing is an intrinsic excitability mechanism.....	38
3.1.5.	mGCs burst firing is not determined by AP after-depolarization	39
3.1.6.	R and L-type channels blockers do not affect mGCs burst firing.....	40
3.1.7.	T-type channels exhibit specific patterns of distribution in dendrites and proximal axon of mGCs	42
3.1.8.	AIS-localized T-type channels control mGCs burst firing.....	45
3.1.9.	mGCs burst firing frequency reaches 100 Hz and more at physiological temperatures	51
3.1.10.	Ca _v 3.2 is the main determinant of mGCs burst firing.....	53
3.1.11.	mGCs high-frequency burst firing occurs during physiological synaptically-driven activity and is impaired in Ca _v 3.2 KO mice.....	57
3.2.	Behavioral and <i>in vivo</i> experiments	60
3.2.1.	Analysis of hippocampal network oscillations and neuronal firing <i>in vivo</i>	60
3.2.2.	Ca _v 3.2 KO mice show behavioral deficits in contextual fear conditioning	63
4.	Discussion.....	67
4.1.	mGCs burst firing.....	67
4.2.	mGCs burst firing is controlled by T-type channels in the axon initial segment.....	67
4.3.	Axon initial segment T-type channels and control of AP threshold.....	68
4.4.	Ca _v 3.2 has major impact on the burst-firing in mGCs.....	69
4.5.	T-type mediated burst firing of mGCs impacts on DG-CA3 communication	69
4.6.	Contextual foot-shock fear conditioning	71
4.7.	Proposed model.....	72
4.1.	Perspectives	72
5.	References	75
6.	Abbreviations	89

1. Introduction

1.1. The dentate gyrus

The major role of the hippocampal formation in learning and memory and its lamellar organization have made it a target of choice for neuroscientists seeking to understand the basis of brain function (Andersen, 2007). The dentate gyrus (DG) is a particular subfield of the hippocampal formation. The DG constitutes the main gateway for cortical information from entorhinal cortex (EC) and the first relay station in the classically described tri-synaptic circuit (EC→DG→CA3→CA1, Figure 1A). The processing of neuronal information performed by the DG is fundamental for the hippocampal formation function (Andersen, 2007; Scharfman, 2011).

The DG is composed of different neuronal types, and the granule cells represent the principal cells (dentate gyrus granule cells, DGGCs, Figure 1B and C). The DGGCs form a dense layer called the granule cell layer. DGGCs extend their dendrites in the molecular layer, where they receive their main excitatory input from pyramidal and non-pyramidal principal cells of the layer II of the medial and lateral EC through the perforant path. In turn, DGGCs send axonal projections to CA3 pyramidal cells in fascicles named mossy fibers (Scharfman, 2011) (Figure 1A). The CA3 pyramidal cells then further project to CA1 pyramidal cells through the Schaeffer collaterals (Andersen, 2007) (Figure 1A). The EC is the main interface between the hippocampal formation and the neocortex (Andersen, 2007; Canto et al., 2008). It notably receives multimodal sensory information from multiple cortical areas (Andersen, 2007; Canto et al., 2008). In other words, an important function of DGGCs is to receive, process and transmit sensory information to the hippocampus.

1.2. DG-dependent neuronal processing, pattern separation and pattern completion

Pattern separation refers to the neuronal processing that transforms overlapping inputs into segregated output encoded by non-overlapping neuronal networks. At the highest cognitive level, this translates into the ability of the brain to discriminate similar, yet different objects, contexts and situations. Pattern completion is in a way the opposite and reflects the ability to reactivate a specific neuronal network, such as one encoding a specific memory, from initially incoherent and/or fragmented information (Deng et al., 2010; Johnston et al., 2016).

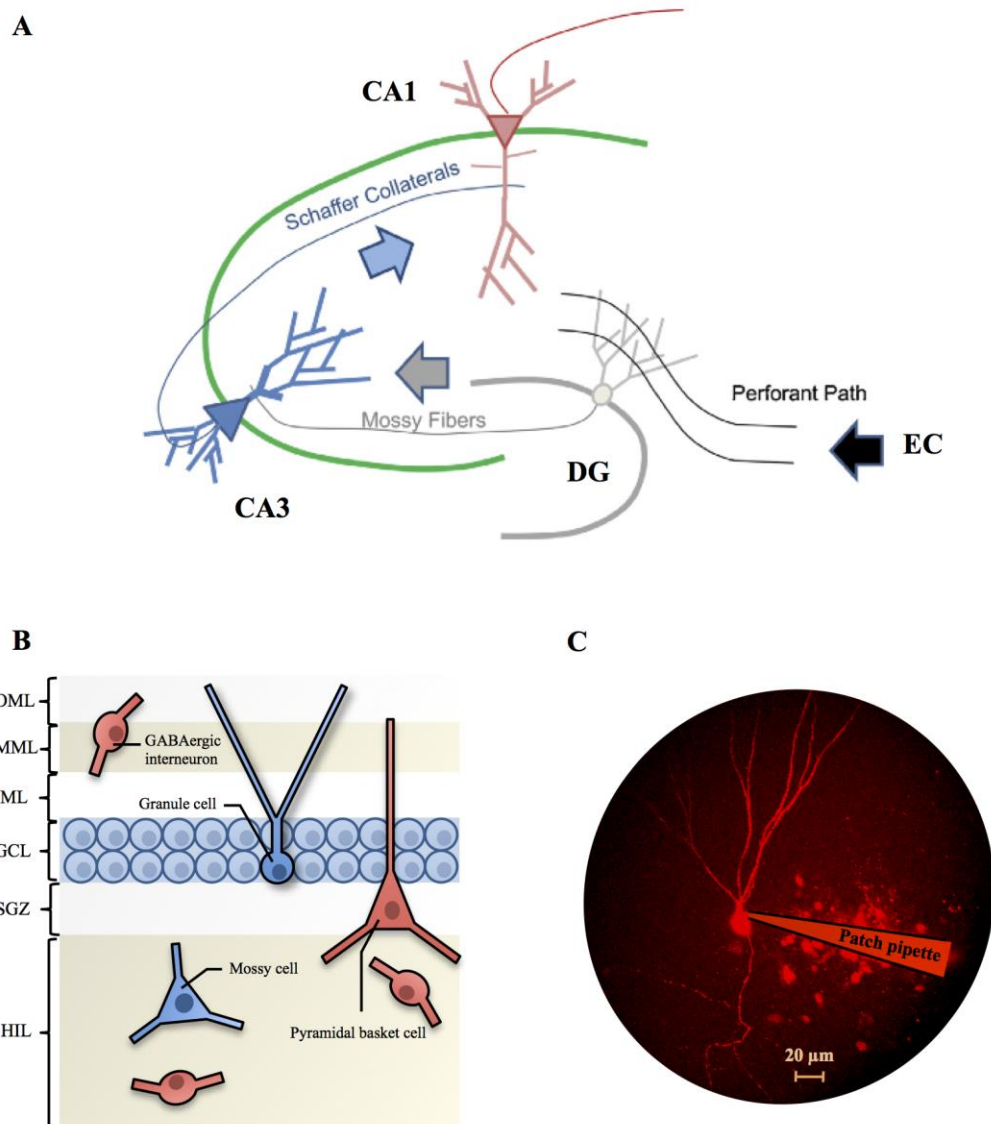


Figure 1: Simplified neuroanatomy and cellular composition of the DG. **A:** The classically described tri-synaptic circuit of the hippocampal formation. The perforant path axonic fibers originating mostly from pyramidal and stellate/fan cells of the layer II of the medial/lateral entorhinal cortex (EC) project to the DG and contact DGGCs dendrites. DGGCs send axonal projections named the mossy fibers to CA3 pyramidal cells, which in turn contact CA1 pyramidal cells through Schaffer collaterals. Reality is more complex and other connections exist within the hippocampal formation. For instance, the EC also sends direct projections to CA3 and CA1. Nevertheless, this simplified tri-synaptic circuit captures many of the hippocampal features. Modified from (Lopez-Rojas and Kreutz, 2016). **B:** Overview of the structural organization and neuronal composition of the DG. Red colors indicate GABAergic and blue colors glutamatergic neurons. The principal cells of the dentate are the granule cells, which are densely packed in the granule cell layer (GCL). Several interneurons subtypes, including basket cells, innervate all layers of the DG. Mossy cells are glutamatergic neurons distributed in the hilus, which contact both granule cells and interneurons and whose functions remain elusive. OML: outer molecular layer; MML: middle molecular layer; IML: inner molecular layer; GCL: granule cell layer; SGZ: subgranular zone; HIL: hilus. Reproduced from (Scharfman, 2016). **C:** A mGICs filled with Alexa594 (red) through a patch pipette, as it can be visualized with the help of 2-photon microscopy. (Personal collection).

Lesions of the DG profoundly affect associative and spatial learning (Sutherland et al., 1983; Walsh et al., 1986; Nanry et al., 1989; Lee and Kesner, 2004). In addition, the optogenetic

re-activation of DGGCs that were active in response to a specific context is enough to evoke or even create memories associated with this context (Liu et al., 2012; Ramirez et al., 2013). These studies confirm the importance of DG in processing sensory information and suggest that DGGCs are not only computational effectors but also constitutive components of memory engrams.

Early modeling studies of the hippocampal circuitry proposed that one of the main functions of the DG is to sort overlapping information from the EC and transmit this processed information to CA3 through orthogonal sets of DGGCs, thus performing pattern separation (Marr, 1971) (Figure 2). This model is notably supported by the neuroanatomical organization of the DG and the intrinsic electrophysiological properties of DGGCs. Indeed, DGGCs largely outnumber both their presynaptic and postsynaptic partners: DGGCs outnumber the pyramidal cells of the CA3 subfield by a ratio of ~5:1 and the neurons of the layer II of the EC by a ratio of ~11:1 in rats (Andersen, 2007). In addition, each DGGC contacts only few CA3 pyramidal cells, around 15 (Andersen, 2007). On the other hand, single CA3 pyramidal cells receive projections from many DGGCs (Andersen, 2007). Overall, this results in a convergence of information from EC to DG and a divergence from DG to CA3, already maximizing the ability of the DG to sort EC inputs into non-overlapping outputs (Amaral et al., 1990, 2007; Schmidt et al., 2012). Moreover, most of DGGCs have intrinsic electrophysiological properties, such as low input resistance and strong attenuation of EPSPs travelling in the dendrites from synaptic contacts to soma, that contribute to the sparse DGGCs firing (Krueppel et al., 2011; Mongiat and Schinder, 2011; Schmidt-Hieber et al., 2004a; Drew et al., 2013; Lopez-Rojas and Kreutz, 2016). Coupled with this, DGGCs exert strong lateral inhibition on neighboring granule cells mediated by interneurons (Scharfman, 2011; Dieni et al., 2013; Temprana et al., 2015). All together, these properties cause most of DGGCs to fire at very low frequency (around 0.2 – 0.5 Hz) in physiological conditions (Jung and McNaughton, 1993; Pernía-Andrade and Jonas, 2014). In turn, this overall low frequency firing of DGGCs theoretically increases the probability that different granule cells will encode similar inputs, *i.e.* improves pattern separation (sparse coding). Substantial experimental evidences confirmed this model of DG acting as a pattern separator (Gilbert et al., 2001; Bakker et al., 2008; Goodrich-Hunsaker et al., 2008; Berron et al., 2016).

In addition to pattern separation, recent studies suggest that DGGCs can also perform pattern completion, a process so far classically attributed to the CA3 subfield of the hippocampus (Nakashiba et al., 2012; Temprana et al., 2015; Kropff et al., 2015). These results are in agreement with the fact that the optogenetic stimulation of selective sets of DGGCs is enough to evoke complete memory engrams, as previously mentioned (Liu et al., 2012; Ramirez et al., 2013).

The latter results provide a good illustration of the fact that, apart from the now relatively well established role in pattern separation, the precise functions of the DG remain only partially understood (Treves et al., 2008).

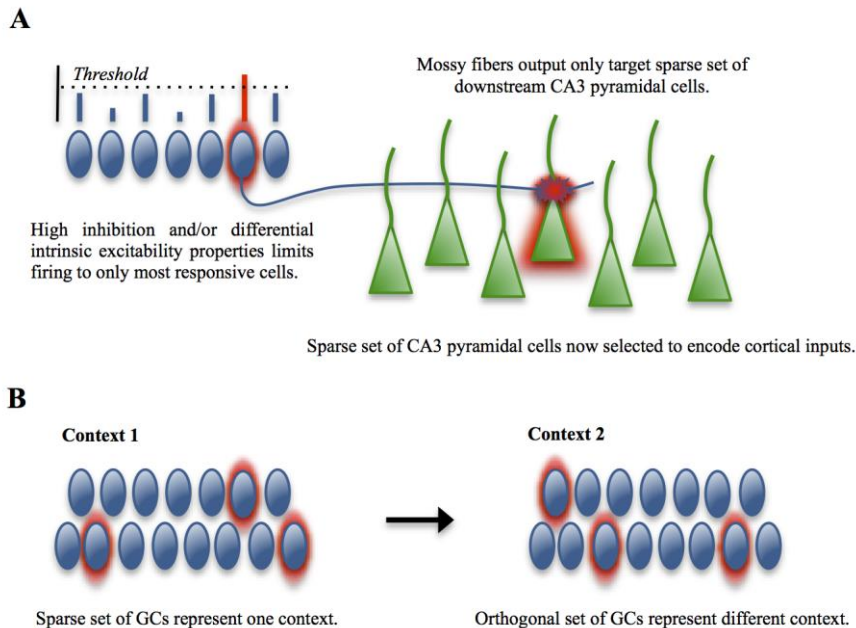


Figure 2: Models of the segregation of neuronal information by the DG underlying pattern separation. **A:** High inhibition and/or differential intrinsic excitability properties cause only small number of DGGCs to produce APs in response to information inflow from the entorhinal cortex (EC). Due to limited connectivity between single DGGCs and CA3 pyramidal cells, only sparse sets of postsynaptic CA3 pyramidal cells get activated. Information has been filtered. **B:** Due to divergence of input from EC to DG, high inhibition and lateral competition between DGGCs, different sensory contexts get encoded by segregated (= orthogonal) populations of DGGCs. A and B reproduced and modified from (Aimone et al., 2011).

1.3. Dentate gyrus neurogenesis: mature and immature granule cells

A topic that notably remains highly controversial is the functional impact of dentate gyrus neurogenesis and the respective roles of the heterogeneous population of DGGCs: newborn immature granule cells and older mature granule cells.

The DG is one of the few regions in the brain where adult neurogenesis has been described (Gage, 2002; Ming and Song, 2011). Newborn DGGCs are generated from neuronal stem cells located in the subgranular zone (Gonçalves et al., 2016). They undergo several maturation steps over the course of weeks during which they migrate in the granule cell layer, receive GABAergic inputs from interneurons then glutamatergic from the EC, develop their dendritic tree, mature their synapses, express increasingly complex arrays of voltage-gated channels and send axonal projections toward CA3 which stabilize later on (Mongiat and Schinder, 2011; Drew et al., 2013; Gonçalves et al., 2016; Lopez-Rojas and Kreutz, 2016). Interestingly, more than half of the adult-generated DGGCs fail to integrate into the network

and undergo apoptosis (Gould et al., 1999; Dayer et al., 2003; Sierra et al., 2010). Adult-generated DGGCs are considered to be functionally and morphologically mature eight weeks after birth and at this stage they are virtually indistinguishable from mGCs generated during embryonic life (Overstreet-Wadiche et al., 2006; Ge et al., 2007a; Laplagne et al., 2007; Sierra et al., 2010).

Due to adult neurogenesis, the global population of DGGCs at every time point of an adult brain's life is composed of a heterogeneous set of mGCs: older mature granule cells (mGCs) and immature granule cells (iGCs) with marked differences in structural, molecular and functional characteristics (Mongiat and Schinder, 2011; Drew et al., 2013) (Figure 3). The detailed comparison of mGCs and iGCs is topic of extensive reviewing and will not be covered in details in this thesis introduction (Mongiat and Schinder, 2011; Drew et al., 2013; Lopez-Rojas and Kreutz, 2016). Several important aspects can be highlighted to better understand the scientific questions underlying my work:

- iGCs are continuously generated, they are therefore well-suited for coding time-specific events (Rangel et al., 2014).

- iGCs are highly excitable in comparison with mGCs (Figure 3), notably because the iGCs have a high input resistance (in the range of the $G\Omega$ as compared to 100-300 $M\Omega$ for mGCs) (Drew et al., 2013), a depolarized resting potential (-40 to -70 mV as compared to -75 to -80 mV for mGCs) (Drew et al., 2013) and because mGCs dendrites function as voltage attenuators, very strongly limiting the propagation of individual EPSP from synapses to the soma (Krueppel et al., 2011).

- iGCs are weakly inhibited by interneurons in comparison with mGCs (Figure 3).

- mGCs are less sensitive to synaptic plasticity than iGCs. Indeed, stronger stimulation protocols are required to elicit long-term potentiation of EC - mGCs synapses (Wang et al., 2000; Snyder et al., 2001; Schmidt-Hieber et al., 2004b; Lopez-Rojas et al., 2016). This could be mediated by differential calcium buffering in the dendrites of iGCs and mGCs (Stocca et al., 2008) (Figure 4). iGCs notably exhibit a marked peak of sensitivity to synaptic plasticity when they are around 4-6 weeks old, which quickly falls down when the cells further age (Ge et al., 2007a).

The final consequence of these properties is that, for a given synaptic input, iGCs will reach threshold for firing much easier than mGCs and will also exhibit long-term synaptic potentiation upon weaker amount of presynaptic stimulation.

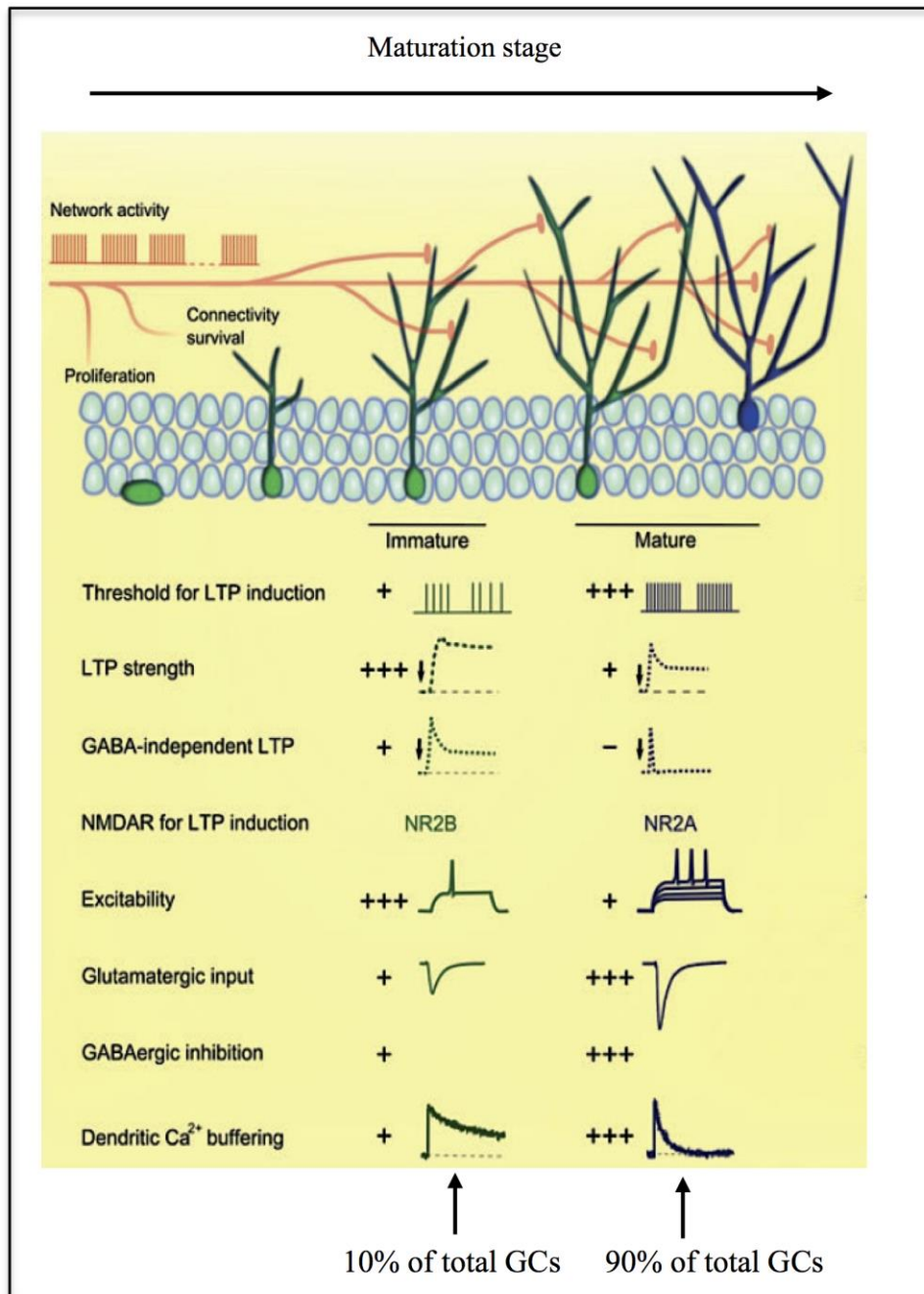


Figure 3: Comparison of structural, molecular and electrophysiological properties of iGCs and mGCs. Figure adapted from (Mongiat and Schinder, 2011), with additional proportions of iGCs and mGCs from (Kempermann et al., 1997; Cameron and McKay, 2001; Ninkovic et al., 2007).

However, some other significant factors should be considered:

- iGCs form a minor proportion of the global DG GCs (around 10% of all DG GCs) (Kempermann et al., 1997; Cameron and McKay, 2001; Ninkovic et al., 2007) (Figure 3).

- iGCs have a relatively undeveloped dendritic arbor in comparison to mGCs and are much less integrated in the DG and brain network for both GABAergic and glutamatergic inputs (Espósito et al., 2005; Ge et al., 2008; Gu et al., 2012) (Figure 3).

- mGCs express an enriched array of voltage-gated channels and thus exhibit more elaborated ionic conductance than iGCs, which ultimately endow them with more advanced intrinsic excitability properties such as sharp sodium spikes and active membrane repolarization conductance that allow them to sustain more efficiently high-frequency repetitive firing (Mongiat et al., 2009; Pedroni et al., 2014).

- mGCs could rely on other mechanism than synaptic plasticity, such as dynamic regulation of dendritic and axonal voltage-gated channels to contribute to hippocampal plasticity (Johnston and Narayanan, 2008; Martinello et al., 2015; Lopez-Rojas et al., 2016; Yamada and Kuba, 2016).

Several studies have supported a preferential role of iGCs in DG function, an equal participation of iGCs and mGCs, a preferential role of mGCs or a context-dependent cooperative action of iGCs and mGCs and the debate is still ongoing (Dieni et al., 2013; Toni and Schinder, 2015; Lopez-Rojas and Kreutz, 2016; Johnston et al., 2016; Becker, 2017).

1.4. A focus on the question of mGC-CA3 connectivity

As illustrated in the previous part of this introduction, DGGCs are mostly silent *in vivo* and their mean firing rate is very low (in the range of 0.2 to 0.5 Hz) (Jung and McNaughton, 1993; Pernía-Andrade and Jonas, 2014). But single DGGCs have to be able to robustly trigger neuronal firing of CA3 pyramidal cells in order to have any impact on hippocampal function.

In an elegant study, Henze and colleagues (Henze et al., 2002) performed intracellular recordings of DGGCs (with characteristics of mGCs) paired with extracellular single unit recordings of proximal CA3 (CA3c) pyramidal cells *in vivo*. They controlled granule cells firing with current injection and assessed the response of the downstream CA3c pyramidal cells. Using this technique, they demonstrated that these putative mGCs started to reliably trigger CA3 pyramids when they fired several APs at frequencies higher than 50 Hz. Increase of the firing frequency of DGGCs improved the probability and sharpness of excitation propagation between granule cells and CA3 pyramidal cells, reaching nearly a 1:1 transmission ratio for frequencies of 100 Hz. The mean number of spikes required for DGGCs to trigger CA3 at these frequencies was around 4, whereas single spikes were ineffective. Illustrative results of the study and schematized conclusions are presented in Figure 4.

In an *in vivo* study, Pernía-Andrade and Jonas (Pernía-Andrade and Jonas, 2014) showed that mGCs, even though mostly silent, preferentially fire very high-frequency (~140 Hz) bursts of 2 to 5 APs when they become active. This burst firing of mGCs would fulfill the requirements to reliably and efficiently trigger their CA3 postsynaptic targets. However, burst firing of DGGCs is not something extensively studied and tends to be associated with

pathological, epileptic conditions (Buckmaster and Dudek, 1997; Scharfman, 2011; Shao and Dudek, 2011; Dengler and Coulter, 2016; Kelly and Beck, 2017).

Thus, how mGCs could exhibit high-frequency firing required for triggering of CA3 pyramidal cells remains a topic to be explored.

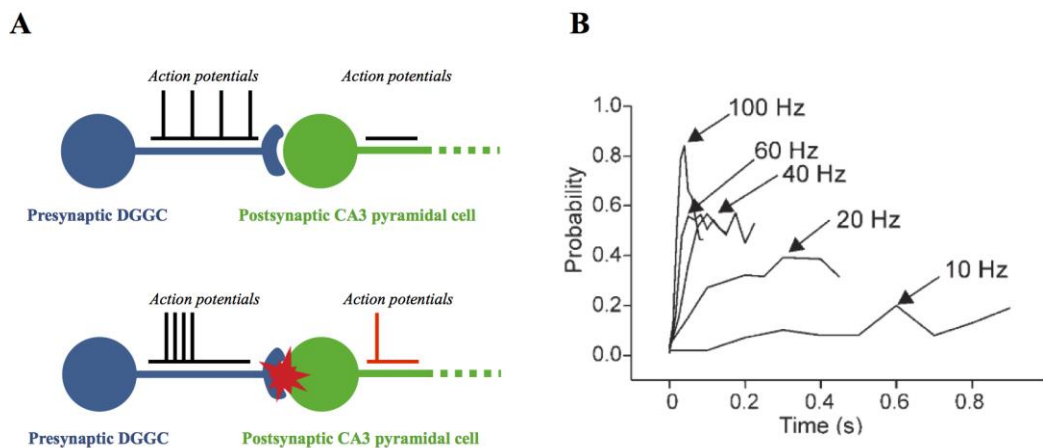


Figure 4: DGGCs need to fire at high-frequency to efficiently trigger their postsynaptic targets: the CA3 pyramidal cells. Figure presenting the results of (Henze et al., 2002). **A:** Illustrative scheme of the results of the study. *Top:* low frequency spikes produced by presynaptic DGGC are ineffective in triggering the firing of a postsynaptic CA3 pyramidal cell. *Bottom:* trains of APs at high frequency can efficiently trigger the firing of the CA3 pyramid. **B:** Actual quantification of frequency-dependent signal transmission efficiency in one DGGC-CA3 pyramidal cell pair from (Henze et al., 2002). X-axis represents the delay between DGGC firing and CA3 response. Y-axis represents the probability to trigger firing of the postsynaptic CA3 pyramidal cell, in other words the transmission of the activity. The different curves represent the effect on these parameters of variable intra-train frequencies of a train of 6 APs. Half-reliable and relatively fast transmission between the presynaptic DGGC and the postsynaptic CA3 pyramidal cell was attained when DGGC fired APs at 50 Hz. DGGC firing at 100 Hz resulted in an almost 1:1 ratio of signal transmission and a fast propagation in the range of few ms.

1.5. Voltage-gated T-type channels and neuronal intrinsic excitability

Intrinsic excitability is “the electrical excitability of a particular neuron. It is determined by the number and distribution of ion channels and receptors that contribute the electrical properties and depolarization potential of the neuron.” (Nature.com). In my study, I was interested in studying if mGCs possess intrinsic excitability mechanisms that could contribute to their high-frequency and short-lasting bursting activity reported *in vivo* (Pernía-Andrade and Jonas, 2014). An interesting candidate here are T-type voltage-gated calcium channels (Iftinca, 2011).

T-type channels comprise three subtypes, $Ca_v3.1$, $Ca_v3.2$ and $Ca_v3.3$ which differ in their molecular structure, voltage-dependence and kinetic properties, but share the common property to be low-voltage activated channels (Perez-Reyes, 2003) (Figure 5A). Low-voltage

activated means that these channels are preferentially active at negative potentials (below -60 mV) and that their threshold for opening is also relatively hyperpolarized as compared to other calcium channels such as L-, P/Q and N-type (oppositely named high voltage-activated channels) (Perez-Reyes, 2003) (Figure 5C). In addition, they quickly inactivate following depolarization and thus can have a stereotypical, short time-frame effect on firing (Figure 5D). The transient current they exhibit upon depolarization is partially at the origin of their name (T for transient). The other cause of their T-type denomination was their small conductance as compared to other high-voltage calcium channels (T for tiny) (Tsien and Barrett, 2013). Due to their permeability to calcium, a ion with two positive charges more concentrated in the extracellular space due to active pumping out of the cytosol (Brini and Carafoli, 2009) but also a major signaling molecule (Clapham, 2007), T-type calcium channels opening can acutely depolarize neuronal membrane but also trigger calcium-dependent intracellular mechanisms. As a consequence of strong voltage-dependent inactivation properties and small conductance to calcium, T-type channels opening produces spatially restricted membrane depolarization and intracellular calcium transients. Thus, they theoretically allow/require a precise subcellular localization and function. In line with this, they have a relatively simple molecular structure since physiologically functional T-type channels can be formed from only α_1 subunit, whereas other voltage-gated calcium channels are functionally formed of an assembly of several subunits (Figure 5B). T-type channels are able to “buddy up” with several types of potassium channels and regulate their activity, which, in turn affects neuronal excitability (Turner and Zamponi, 2014).

A well-documented effect of T-type channels on intrinsic excitability is to endow neurons with a burst firing phenotype. This has been shown in relay cells, the principal cells of the thalamus (Zhan et al., 1999; Kim et al., 2001), but also in cartwheel cells, the dominant type of interneuron in dorsal cochlear nucleus, where T-type channels localized at the level of the axon initial segment were shown to control this phenomenon (Bender and Trussell, 2009a; Bender et al., 2012; Bender and Trussell, 2012). Interestingly, the same authors demonstrated that this T-type channels control of cartwheel cells firing could be dynamically modulated by dopamine (Bender et al., 2010, 2012).

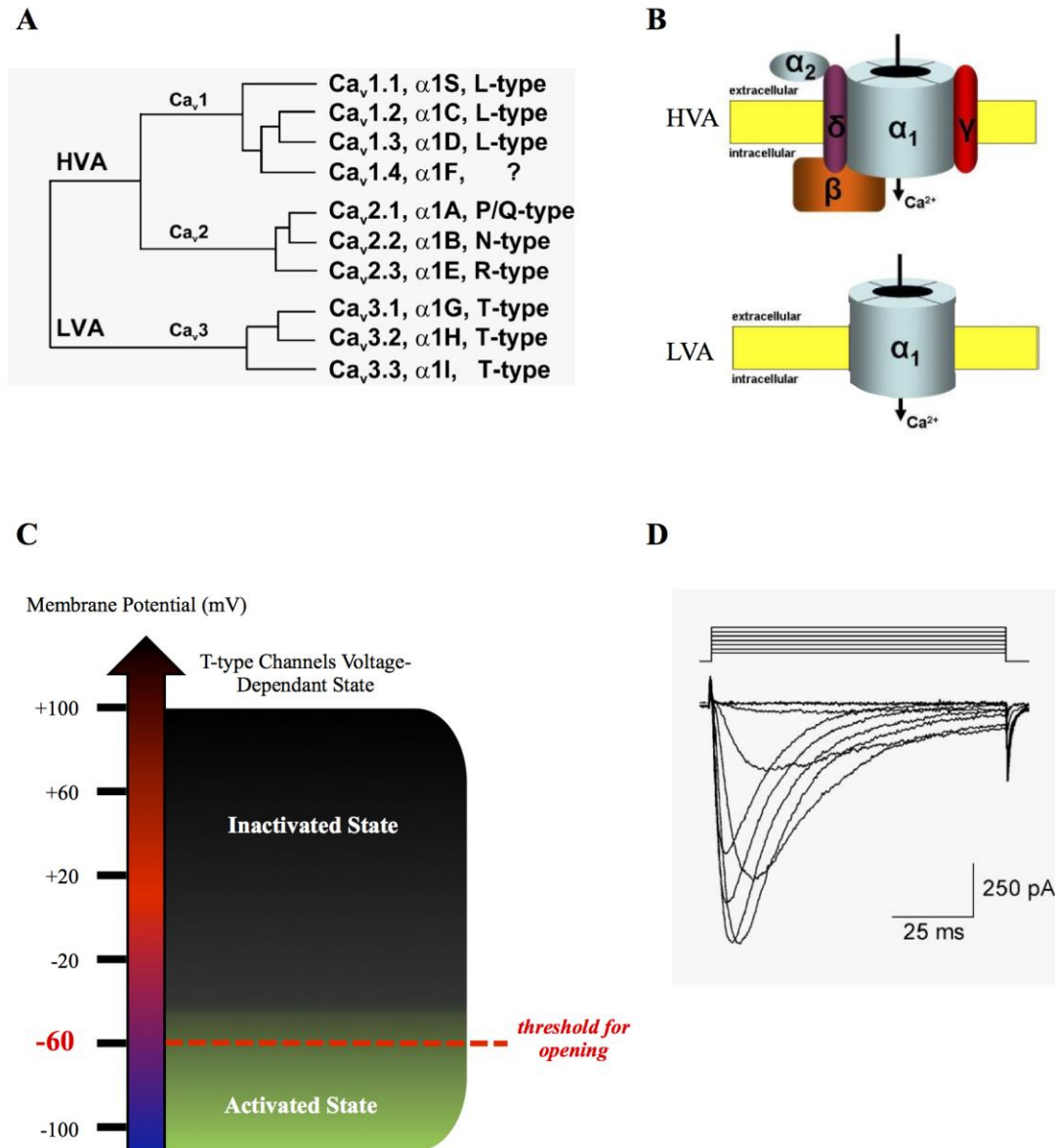


Figure 5: Classification, structure and functional properties of Low-voltage activated T-type calcium channels. **A:** Classification and terminology of voltage-gated calcium channels. T-type channels form the family of low-voltage activated channels (LVA) and comprise three members: $Ca_v3.1$, $Ca_v3.2$ and $Ca_v3.3$. They can also be denominated $\alpha1G$, $\alpha1H$ and $\alpha1I$ based on the gene encoding their α_1 subunit, the main and pore-forming subunit of voltage-gated calcium channels. They are molecularly and functionally segregated from other voltage-gated calcium channels L-, P/Q-, N- and R-type channels, which are high-voltage activated channels (HVA) and are encoded by different genes and formed by different subunits. Figure from (Perez-Reyes, 2003). **B:** Typical molecular composition of physiologically functional voltage-gated channels. HVA calcium channels are formed by an assembly of their α_1 subunit and additional regulatory subunits whereas LVA T-type channels are fully functional with only their α_1 subunit. Modified from (Iftinca, 2011). **C:** Voltage-dependence properties of T-type channels. T-type channels enter a ready-to-activate configuration at negative voltages and open at hyperpolarized potentials as low as around -60 mV. They undergo strong voltage-dependent inactivation and are mostly inactivated from voltages around -40 mV. Personal scheme. **D:** Typical T-type currents elicited by gradual depolarization from negative potentials. Note the fast voltage-dependent inactivation occurring in less than 100 ms. Traces from (Perez-Reyes, 2003).

1.6. T-type channels in the DG

T-type channels are strongly expressed in the DG, especially the Ca_v3.2 isoform (Talley et al., 1999; McKay et al., 2006; Francois, 2013; Aguado et al., 2016; Bernal Sierra et al., 2017). For Ca_v3.1, immunolabeling and *in situ* hybridization studies have reported somewhat conflicting expression levels. Talley and colleagues (Talley et al., 1999) observed significant staining for Ca_v3.1 mRNA in the granule cell layer but McKay et al. and Aguado et al. found negligible levels of Ca_v3.1 protein labeling (McKay et al., 2006; Aguado et al., 2016). Ca_v3.3 protein has been found significantly expressed at the level of DGGCs soma (McKay et al., 2006).

At a subcellular level, conflicting results of immunolabeling of Ca_v3.2 have also been reported in DGGCs. McKay et al. found a predominantly somatic expression of this isoform while Aguado et al. described a stronger labeling in the distal dendrites. Using a more precise immunogold labeling technique, Martinello and colleagues showed that Ca_v3.2 are more densely expressed in dendrites and in spines but are also present in the soma and in the axon of mGCs (Martinello et al., 2015).

1.7. Impact of T-type channels on iGCs and mGCs intrinsic excitability

In iGCs, activation of T-type channels produces a low-threshold calcium spike that can be visualized in whole-cell recordings without any pharmacological isolation (Schmidt-Hieber et al., 2004b). This is notably due to the high input resistance of iGCs, which allows small calcium fluxes mediated by T-type channels to have strong impact on membrane potential. In addition, the relatively limited variety of voltage-gated ion channels open at resting potential in iGCs contributes to the isolation of this phenomenon. These T-type channels-mediated low threshold calcium spike activates at lower voltages than sodium channels and produces a depolarizing drive that facilitates reaching APs threshold, thus strongly enhancing iGCs excitability (Schmidt-Hieber et al., 2004b).

Oppositely, no such low threshold calcium spike can be measured in whole-cell recordings of mGCs in standard conditions (Schmidt-Hieber et al., 2004b; Pedroni et al., 2014). In addition, acute blockade of T-type channels produces no changes in the sodium spike threshold and mGCs firing (Schmidt-Hieber et al., 2004b; Martinello et al., 2015). However, low threshold calcium spikes can be observed in mGCs in the presence of potassium channels blockers (Blaxter et al., 1989) and T-type channels localized at the level of their axon initial segment have been implicated in a cholinergic-induced modulation of axon initial segment M-type potassium channels and subsequent plasticity of AP threshold (Martinello et al., 2015).

1.8. Aims of the study

1. To study the impact of T-type channels on mGCs intrinsic excitability
2. To quantify the distribution of T-type channels-mediated calcium fluxes in mGCs dendrites and proximal axon
3. To further investigate the role of axon initial segment-localized T-type channels in controlling mGCs firing
4. To examine the individual function of the $Ca_v3.2$ isoform in regulating mGCs intrinsic excitability
5. To explore the importance of mGCs T-type channels in DG-CA3 communication

2. Materials and Methods

2.1. Materials

2.1.1. Chemicals

Anaesthetic	
<u>Name</u>	<u>Supplier</u>
Isoflurane Baxter	Baxter
Artificial Cerebro-Spinal Fluid (ACSF)	
<u>Name</u>	<u>Supplier</u>
NaCl	Carl Roth
KCl	Fluka Carl Roth
MgSo ₄ .7H ₂ O	Merck
CaCl ₂	Merck
KH ₂ PO ₄	Merck
NaHCO ₃	Carl Roth
D-Glucose	Fluka Carl Roth
Intracellular solution	
<u>Name</u>	<u>Supplier</u>
KOH	Carl Roth
HCl	Carl Roth
GTP	Sigma-Aldrich
ATP	Sigma-Aldrich
Potassium Gluconate	Fluka
EGTA	Carl Roth
HEPES	Carl Roth
Alexa594	Invitrogen
Fluo-5F	Invitrogen
Pharmacological antagonists	
<u>Name</u>	<u>Supplier</u>
TTX	Tocris Bioscience
CNQX	Tocris Bioscience
D-AP5	Tocris Bioscience Abcam
(-)-Bicuculline methiodide	Tocris Bioscience Sigma-Aldrich
NiCl ₂ .6H ₂ O	Sigma-Aldrich
TTA-A2	Kind gift from Dr. Emmanuel Bourinet, Institut de Génomique Fonctionnelle, Montpellier, France
NNC 55-0396	Tocris Bioscience

Mibefradil	Tocris Bioscience
Nifedipine	Abcam
SNX-482	Peptide Institute
DMSO	Carl Roth
Surgery and tetrodes implantation	
In details in the text	

2.1.2. Equipment

Brain slices preparation		
<u>Name</u>	<u>Details</u>	<u>Supplier</u>
Vibratome	Model VT 1000S	Leica
Slice storage insert		Warner instruments
Patch pipette preparation		
<u>Name</u>	<u>Details</u>	<u>Supplier</u>
Glass capillaries	1,50x0,86x100 mm with filament and fire polished	Biomedical instruments
Pipette puller	Flaming/Brown micropipette puller model P-97	Sutter Instruments
Main electrophysiology setup		
<u>Name</u>	<u>Details</u>	<u>Supplier</u>
Microscope	Water immersion upright microscope model BX50WI	Olympus
Light source	Halogen lamp	Osram
Light source power/transformer	Model TH3	Olympus
CCD camera	Model KP-M2RP	Hitachi Kokausai Electric Inc.
Temperature controller	Single channel automatic heater controller model TC-324B	Warner Instruments
Circulation system	Peristaltic tubing pump model Reglo	Ismatec
Fluorescence lamp	High pressure mercury burner model BH2-RFL-T3	Olympus
Amplifier	EPC9 amplifier	HEKA
Acquisition software	Patchmaster	HEKA
Micromanipulators	Model SM 5-9	Luigs and Neumann
Stimulator	Stimulus isolator, model ISO-Flex	A.M.P.I
Micro-pressure system	Model PDES-02DX	npi
2-photon imaging setup		
<u>Name</u>	<u>Details</u>	<u>Supplier</u>
2-photon microscope	Commercial 2-photon microscope, model Femto2D	Femtonics
Light source	Red-infrared LED	
Laser	Ti:Sapphire femtosecond laser, model Cameleon ultra I	Coherent

Temperature controller	Dual channel automatic heater controller model TC-344B	Warner Instruments
Headstage controller	Model MP285	Sutter Instruments
Micromanipulator	Model SMX	Sensapex
Amplifier	Model Multiclamp 700B	Molecular devices
Acquisition interface	Model digidata 1440A	Molecular devices
Acquisition software	Clampex	Molecular devices
<i>In vivo</i> experiments		
In details in the text		

2.1.3. Analysis software

<u>Name</u>	<u>Supplier</u>
Fitmaster	HEKA
Clampfit	Molecular devices
Mini Analysis	Synaptosoft
Anymaze	Stoelting Europe
Spike2	Cambridge Electronic Design
Excel	Microsoft
Prism	GraphPad Software

2.1.4. Animals

Wistar Han rats from Charles River and C57BL/6J mice from Charles River were bred in house. For local block of T-type channels, Wistar Han rats were ordered from Charles River and allowed to recover in house for 1-2 weeks before experiments. Ca_v3.2 KO mice originally described by Chen and colleagues (Chen et al., 2003) and backcrossed to C57BL/6J background by Janvier Labs, were a kind gift of Dr. Emmanuel Bourinet, Institut de Génomique Fonctionnelle (Montpellier, France) and were further bred in house.

2.2. Methods

2.2.1. *In vitro* single cells recordings

2.2.1.1. Hippocampal slices

Transversal acute brain slices were prepared from young adult Wistar Han rats (8-10 weeks), young adult C57 BL/6J mice (20-28 weeks) and young adult Ca_v3.2 KO mice (20-28 weeks). Animals were anesthetized with isoflurane and quickly decapitated. The brain was removed and the right hemisphere was isolated in ice-cold artificial cerebrospinal fluid (ACSF) containing in mM: 124 NaCl, 4.9 KCl, 2 MgSO₄, 2 CaCl₂, 1.2 KH₂PO₄, 25.6 NaHCO₃ and 20

glucose, equilibrated with 95% O₂/5% CO₂, pH=7.4, 310 mOsm. 400 µm-thick slices were subsequently cut in ice-cold ACSF and transferred to a holding chamber at 34°C for 25 minutes before further storage at room temperature. The slices were left to recover for minimum of 1 hour before the start of the experiment. The same composition of ACSF was used for the whole procedure from brain removal to storage.

2.2.1.2. Current-clamp whole-cell recordings

Patch pipettes were pulled from a flaming/brown horizontal micropipette puller (model P-97, Sutter instruments) and filled with an intracellular solution containing in mM: 130 potassium gluconate, 20 HEPES, 1 CaCl₂, 2 MgCl₂, and 10 EGTA. The pH was adjusted to 7.3 and the osmolarity to 290 mOsm. In corresponding experiments, the volume marker Alexa594 and the low-affinity calcium-sensitive dye Fluo-5F were added to the intracellular solution. The extracellular solution (ACSF) used for recordings was the same as for cutting, except for the presence of some pharmacological blockers mentioned and its temperature was adjusted to 25°C or 32°C depending on the experiment. Once transferred to the recording chamber, slices were left to incubate in the bath solution for 15 minutes prior to recordings. Whole-cell current clamp recordings on granule cells were established using the patch-clamp technique. Cells were held at -70mV by injecting a small holding current as required. Mature granule cells were selected based on their shape, size and distribution in the two outer thirds of the granule cell layer; and their identity was further confirmed by their input resistance (Wang et al., 2000; Schmidt-Hieber et al., 2004b; Ge et al., 2007b). Different slices were incubated with bath solutions according to the experimental conditions and corresponding pools of cells were compared independently. The amount of mature granule cells recorded from different slices and in different experimental conditions was equilibrated among days and animals. Electrophysiological data were acquired at 20 or 10 kHz.

2.2.1.3. Pharmacology

2.2.1.3.1. *T-type channel blockers*

Except for the experiments of local blockade with micro-pressure applied puffs, all T-type channels blockers were bath-applied at concentrations widely used in the literature and mostly selective for T-type channels and more specifically the Ca_v3.2 subtype:

- 100 µM NiCl₂ (Lee et al., 1999; Bijlenga et al., 2000; Joksovic et al., 2005; Obejero-Paz et al., 2008; Engbers et al., 2012; Zhang et al., 2012; Cui et al., 2014)

- 3 μ M mibefradil (McDonough and Bean, 1998; Martin et al., 2000; Todorovic et al., 2001; Perez-Reyes, 2003)
- 1 μ M TTA-A2 (Kraus et al., 2010; Todorovic and Jevtovic-Todorovic, 2011; Francois et al., 2013; Fernández et al., 2015)
- 50 μ M NNC 55-0396 (Huang et al., 2004; Li et al., 2005).

2.2.1.3.2. R and L-type channels blockers

In corresponding experiments, 10 μ M nifedipine, a relatively selective blocker of L-type calcium channels (Beck et al., 1997; Zhou and January, 1998; Shen et al., 2000) and 500 nM SNX-482 were used. SNX-482 is a potent blocker of Kv4.3 A-type potassium channels, but also blocks R-type calcium channels at higher concentrations (Newcomb et al., 1998; Wang et al., 1999; Bourinet et al., 2001; Myoga and Regehr, 2011; Kimm and Bean, 2014). The efficiency of R-type block by SNX-482 has been reported to be variable among cell types (Newcomb et al., 1998), but the concentration we used, 500 nM, has been successfully used on DGGCs (Sochivko et al., 2002; Breustedt et al., 2003).

2.2.1.3.3. Synaptic transmission blockers

In corresponding experiments, a classical cocktail of synaptic blockers consisting of 10 μ M CNQX, 50 μ M D-AP5 and 20 μ M bicuculline (antagonists of AMPA/kainate, NMDA and GABA_A receptors, respectively) were added in the bath solution to study intrinsic excitability of mGCs in isolation from the network.

2.2.1.3.4. Considerations on pharmacology preparation and use

Most of the pharmacological blockers and antagonists were prepared from high concentration stock solutions dissolved in water. TTA-A2 and nifedipine were dissolved in dimethyl sulfoxide (DMSO). The dilution factors were adjusted in a manner that the final concentration of DMSO in the extracellular solution did not exceed 0.1%, a concentration considered to be not toxic for cells. In the corresponding control experiments, DMSO at similar concentration was added to the ACSF. I did not observe any signs of DMSO-induced toxicity in my experiments.

2.2.1.4. Characterization of mGCs firing phenotype

10-30 M Ω tip resistance pipettes were used to limit the washout of the cells and recordings were made as fast as possible following establishment of the whole-cell configuration. Some other empirical factors such as the patching of the cells on somatic compartments distal from the axon also improved the occurrence of mGCs burst firing. In all experiments, repeated stimulations of mGCs were interleaved with an inter-sweep interval of 10-15 seconds to allow complete recovery of T-type channels from inactivation (Perez-Reyes, 2003).

2.2.1.4.1. *Characterization of burst firing following somatic current injection*

The standard protocol to characterize mGCs firing phenotype consisted in stimulating the cells by 250 ms-long depolarizing somatic current injections of 40 pA increasing intensity starting from 0 pA with respect to the holding current (Figure 6B). The first step intensity eliciting firing of the cell was termed rheobase (R+0) and the next +40 pA step was termed rheobase+1 (R+1) (Figure 6B). These two steps were used for quantification of burst firing as they allowed clear discrimination between bursting and non-bursting APs and produced low and mild stimulations arguably close to physiology. In my conditions, burst firing was mostly restricted to the first two spikes of the cells discharge while later spikes were usually elicited in a lower-frequency tonic pattern. This phenomenon correlates well with the fast voltage-dependant inactivation properties of the channels which most likely gets quickly inactivated in my protocol and thus can only strongly affect the initial spikes (Perez-Reyes, 2003). Accordingly, quantification of the burst firing was made by measuring the inter-spike interval (ISI) between the 1st and 2nd AP (1st ISI) and later tonic spikes coming at the end of the discharge, in these conditions the 4th and 5th AP (4th ISI) (Figure 6C).

2.2.1.4.2. *Quantification of the ADP and correlation with firing phenotype*

Single spikes were elicited by 5 ms-long 600 pA current injection (Figure 18A). The amplitude of the ADP following the AP was measured 6 ms and 20 ms after the peak of the AP (Figure 18A), values corresponding to the average timing of the peak of the ADP as calculated in all cells recorded for this experiment, and the average timing of the bursting spike observed in similar conditions (50 Hz) (Figure 6D). Firing phenotype in response to the 250 ms, Δ 40 pA stimulating protocol described above was also assessed in the same cells to calculate the correlation between the ADP amplitude and the 1st ISI at step R+1 in the Δ 40 pA protocol.

2.2.1.4.3. Medial perforant path stimulation-driven activity

A 6-10 M Ω patch pipette was filled with extracellular solution and placed in the molecular layer around 100 μ m from the cell body along a virtual line perpendicular to the granule cell layer. An ISO-Flex stimulator (A.M.P.I) was used to deliver short square-pulses of decreasing intensity from 100 to 10 μ A to elicit both subthreshold and suprathreshold EPSPs (Figure 22A). The EPSP slope and the number of spikes (which rarely exceeded 2 APs) were quantified. E-S curves (EPSP slope vs. Spike probability) for 1 AP and more or 2 APs and more were calculated individually for each cell from values of EPSP slopes and number of spikes and fitted with the following equation: $Y = \text{Bottom} + (\text{Top} - \text{Bottom}) / (1 + 10^{((E50 - X) * \text{HillSlope})})$ with constraints $\text{Bottom} = 0$ and $\text{Top} = 100$. The half-effective E50 values were stored for analysis. The extracellular solution contained 20 μ M bicuculline.

2.2.1.4.4. Local blockade of T-type channels

100 μ M Alexa594 was added to the intracellular solution to allow visualization of mGCs processes following green light illumination. The extracellular solution was the same as described previously except that KH_2PO_4 was removed to prevent NiPO_4 precipitation and that KCl was increased to 6.1 mM to compensate for it. The extracellular solution contained 10 μ M CNQX, 50 μ M D-AP5/D-APV and 20 μ M bicuculline. A 100-130 M Ω tip resistance patch pipette was filled with extracellular solution and also contained 10 mM NiCl_2 and 100 μ M Alexa594 -or only extracellular solution and 100 μ M Alexa594 for the control group- and was mounted on a micro-pressure system from npi (Tamm, Germany). Alexa594 fluorescence was used to ensure that no solution was leaking from the puff pipette, as well as to estimate the size of the puff. Following establishment of whole-cell configuration, the firing phenotype of the cell and the R+1 current injection intensity was assessed using the $\Delta 40$ pA protocol described previously. The position of the axon and proximal dendrites were quickly assessed using Alexa594 fluorescence. The puff pipette was then placed in close proximity to the axon or a proximal dendrite, 20 μ m away from the soma (Figure 14A, 15D and 15E). mGCs were stimulated with 250 ms-long depolarizing steps of somatic current injections of intensity corresponding to their R+1, ± 20 pA. After 4 repeats, 15-PSI pressure steps of 100 ms-increasing length, starting from 100 ms up to 800 ms were applied through the micro-pressure system, paired with 8 repeats of the somatic current injection protocol and terminating at the beginning of the somatic current injection stimulation. Due to the size of the pipette, the puff was local and encompassed an area of roughly 5-25 μ m diameter. The somatic injection protocol was then repeated every 15 seconds until stable recovery of the burst firing. The speed

of recovery was variable, ranging from tenth of seconds to couples of minutes but mostly occurred within a minute. To homogenize the data, only the 6 sweeps following stable recovery were used for quantification. Figure 14 illustrate the whole protocol. For puffs in the axon, another method consisting in empirically varying the puff length (300-1400 ms, average 767 ms) and the time between the puff and the somatic current injection (1000-1400 ms, average 1000 ms) was also used (Figure 16).

2.2.1.5. 2-photon imaging

A commercial two-photon laser-scanning Femto2D microscope from Femtonics (Budapest, Hungary) was used. Laser pulses at 810 nm were provided by a Ti:Sapphire femtosecond laser (Cameleon Ultra I, Coherent). Cells were stimulated with two 5 ms-long current injection of 600 pA intensity with 15 ms of interval to elicit a duplet of APs at 50 Hz that reliably propagated to distal dendrites and axon (Figure 12A). In another protocol, APs were blocked by bath application of 1 μ M TTX and cells were stimulated with current injections of 250 ms length and 40 pA increasing intensity to reproduce the standard protocol used to characterize burst firing (Figure 13A). Care was taken to not depolarize the cell further than -20 mV, providing maximal T-type channels activation with limited activation of HVA channels (Zhang et al., 2000; Perez-Reyes, 2003; Pourbadie et al., 2017). This protocol produced membrane potential changes that could not propagate reliably to distal processes and was used to assess more specifically T-type channels-mediated fluxes in the proximal axon. For measuring Ca^{2+} signals, green (Fluo 5F) and red (Alexa-Fluor 594) fluorescence were collected during 500 Hz line scans across the dendrites and in the proximal axon. Fluorescence changes were quantified as the increase in green fluorescence normalized to the average red fluorescence ($\Delta G/R$) (Yasuda et al., 2004). The Ca^{2+} transient peaks were estimated from exponential fits of the fluorescence traces. Fluorescence was collected through the objective (60×1.0 NA, Olympus) and the oil immersion condenser (1.4 NA, Olympus) with two pairs of photomultipliers (2 for collecting red band fluorescence and the other 2 for the green band fluorescence). An additional photomultiplier was used to collect the transmitted infrared light. The composition of the intracellular solution for these experiments was in mM: 130 potassium gluconate, 20 HEPES, 2 MgCl_2 , 2 Mg-ATP, 0.3 Na-GTP, 0.25 Fluo-5F and 0.02 Alexa 594. The pH was adjusted to 7.3 and the osmolarity to 290 mOsm. The extracellular solution was the same as in the other experiments and also contained 10 μ M CNQX, 50 μ M D-AP5/D-APV and 20 μ M bicuculline. Fluorescence data recording started 15 min after attaining the whole-cell configuration.

2.2.1.6. In vitro data analysis

Data acquired with Clampex (Molecular devices, Sunnyvale, USA) and Patchmaster (HEKA, Lambrecht, Germany) were analysed with Clampfit (Molecular devices, Sunnyvale, USA) and Fitmaster (HEKA, Lambrecht, Germany), respectively. Further analysis was carried out using Excel (Microsoft, Redmond, Washington, USA) and Prism (GraphPad Software, La Jolla, USA). For statistical analysis, normality of the data sets was assessed with D'Agostino & Pearson omnibus normality test prior to further parametric or non-parametric tests indicated in details in the text. In corresponding cases, data sets were fit with Boltzmann sigmoid functions and group comparisons were made based on the best-fit values of their respective Boltzmann fits.

2.2.2. In vivo recordings of DG and CA3 activity and contextual fear conditioning

Behavioral and *in vivo* recordings study were the result of a collaborative work. Headstages design and fabrication, fabrication of tetrodes, animals' surgery and implantation were performed with the help of Dr. Oleg Senkov (Deutsche Zentrum für Neurodegenerative Erkrankungen, DZNE, Magdeburg, Germany) and Dr. Andrey Mironov (Nizhny Novgorod State University, Nizhniy Novgorod, Russia). Contextual fear conditioning experiments and *in vivo* recordings of DG and CA3 neuronal activity were carried out by myself under the guidance of Dr. Oleg Senkov. Analysis of local field potential, multiunit and single unit activity was achieved with the help of Dr. Arthur Bikbaev (Leibniz Institut für Neurobiologie, LIN, research group Molecular Physiology, Magdeburg, Germany).

2.2.2.1. Animals housing and procedures

In these experiments I used adult (4-6-month-old) male Cav3.2 KO and wild type (C57Bl6J) mice. At least 2 weeks before starting the experiments, the mice were transferred from the major animal facility of LIN to a small vivarium in DZNE, where they were housed individually with food and water ad libitum on a reversed 12:12 light/dark cycle (light on at 9:00 p.m.). All behavioral experiments were performed at the afternoons during the dark phase of the cycle when mice are active, under constant temperature ($22\pm 1^\circ\text{C}$) and humidity ($55\pm 5\%$). All treatments and behavioral procedures were conducted in accordance with ethical animal research standards defined by German law and approved by the Ethical Committee on Animal Health and Care of the State of Saxony-Anhalt, Germany, license number: 42502-2-1316DZNE.

2.2.2.2. Design and fabrication of headstages

Lightweight headstages for tetrode implantation were built using an Ultimaker2+ 3D printer from Ultimaker. 3D models were designed using Fusion 360 3D CAD/CAM software from Autodesk and sliced by Cura free software provided by Ultimaker, prior to printing. Models were printed from 2.85 mm thick Polylactic Acid plastic filaments from Verbatim, which allow producing smooth, not toxic, eco-friendly, odorless and robust objects that can be autoclaved if needed. In short, headstage 3D model was designed to house 8 tetrodes and one 32-channels EIB (Electrode Interface Board, Neuralynx). The whole implant including 3D printed parts, EIB, tetrodes, pins, screws and copper adhesive tape around the headstage weighted only about 3 - 4 g; together with dental cement its weight reached 4 - 4.5 g. Adult wild type mice with weight of 30 g can easy tolerate up to 6 - 7 g on their heads, due to very strong neck muscles, so the designed implant could be used in behavior experiments.

2.2.2.3. Fabrication of tetrodes

For fabrication of tetrodes we used Formvar coated Nichrom wire (\varnothing 18 μ m/25 μ m) from Science Products. To make tetrodes, 4x wires were twisted together using a magnetic stir for spinning, and glued as one tetrode by melting Formvar with a heating gun adjusted to produce air flow at temperature not more than 220-240 °C.

2.2.2.4. Implantation

Chronic implantation of tetrodes in mice was performed similar as in (Senkov et al., 2006; Kochlamazashvili et al., 2012; Senkov et al., 2015, 2016; Minge et al., 2017) with minor changes. In brief, mice were anesthetized with a 1-3% Isoflurane delivered as a mixture with O₂ through a Vaporizer (Matrx VIP 3000, Midmark) and a mouse breathing mask. Prior to any surgical manipulation, the mouse was given the analgesic Carprofen (5 mg/kg b.w. s.c., Rimadyl, Pfizer Pharma GmbH), its head hairs were shaved by using a small clipper (Contura, HS61, Wella), its skin was cleaned by 75% Ethanol, followed by 10% Povidone Iodine (Dynarex, Orangeburg, Mexico) as a topical long-lasting antiseptic, then an additional analgesic Xylocain was used on skin (a pumpspray, 10 mg Lidocain, Astra Zeneca GmbH, Wedel, Germany). The mouse then was placed in a stereotaxic frame (Narishige, Japan), and all next procedures were performed under a surgical binocular microscope (Labomed Prima DNT, Labo America Inc., Fremont, USA, www.laboamerica.com) and on a heating pad (DC Temperature Controller, WPI) to maintain mouse body temperature constant (34 - 36° C) over

surgery. The mouse scalp skin was circular incised (\varnothing 10 mm) and removed. The edges of the skin were processed with 75% Ethanol and Xylocain. The scalp bone was carefully cleaned from tissue by using 75% Ethanol and 3% Hydrogen Peroxide, H_2O_2 , then, dried with a heating drier at the lowest temperature ($<40^\circ C$) and speed (Steinel GmbH, HG-2310 LCD, Herzebrock-Clarholz, Romania). Treated with H_2O_2 bone better reveals position of bregma, lambda, sutures and big capillaries under the bone. This helps to correctly position tetrodes in the brain, avoiding excessive bleeding. After marking coordinates for implantation, 4 small holes for anchoring and ground screws were drilled in two frontal bones and in the left and right parietal ones at the border with the interparietal bone by using a dental micro motor (Eickemeyer, Tuttlingen, Germany, www.eickemeyer.de). Then in frontal holes, two small screws (Plastic One) and in the parietal holes a screw with soldered ground/reference wire were gently inserted. Then all 4 screws and wire were covered with acrylic dental cement Paladur (Heraeus Kulzer GmbH, Hanau, Germany) leaving the marked areas for tetrodes free of acrylic. Implantation began with drilling of a small hole for the most anterior and closer to the middle line tetrode. The tetrode was stereotaxically implanted by using a self-made universal holder for cannulas and electrodes/tetrodes (a small curved tweezers from FST with a metal ring. During implantation, a tetrode gently touched the surface (Dura) of the brain (making "0" reference) and only then it was approached farther to its DV coordinate and secured with a small amount of acrylic. Coordinates for 8 tetrodes were the following, for 4x tetrodes in the mouse dorsal hippocampal Dentate Gyrus (DG) in both hemispheres: AP: -1.6 mm, L: $\pm 0.75-1$, DV: 2.0 mm; and AP: -2.5 mm, L: $\pm 1.5-2$, DV: 2.0 mm; and for 4x tetrodes in CA3 area of the hippocampus in both hemispheres: AP: -1.6 mm, L: $\pm 1.5-1.75$, DV: 2.0 mm; and AP: -2.5 mm, L: $\pm 2.5-3$, DV: 2.25-2.5 mm, were set according to the mouse brain atlas (Paxinos and Franklin, 2012).

After implantation of tetrodes, more dental cement was used to secure the whole system on the bone. Next step was to glue a bottom part of the headstage pedestal (using dental cement) to the skull, positioning it optimally for the mouse and implants, and as horizontally as possible. After the whole system is well secured, the Neuralynx EIB-32 headstage board with two screws was positioned on the top. Once this was done, all the tetrodes wire tails were gently inserted into channels holes on the EIB-32, and pinned by golden pins (Neuralynx). The pins provide mechanical connections between electrode wires and the EIB-32 channel inputs. Removal of insulation from wires was not necessary; golden pins perfectly do it themselves during insertion. After assembly was completed, all ground wires were soldered together and the upper cover "hat" was placed above the bottom pedestal and tetrodes and fixed to it with two small screws. The protecting "hat" with a Faraday cage was made by wrapping it with one-side-self-adhesive copper foil soldered with silver wire for grounding, and covered for protection if necessary with another layer of plastic self-adhesive tape. After the surgery lasting for about 4

- 5 hours, mice were placed back into their home cages and monitored until full awakening, which usually lasted about 15 - 20 min. Carprofen (5 mg/kg b.w. s.c., Rimadyl, Pfizer Pharma GmbH) was used as a postoperative analgesic. All behavioral investigations and recordings were performed after the mice had fully recovered at least 5 - 7 d after surgery, but usually 2 weeks. Recordings were done by using Neuralynx 32 channels preamplifier and 5 meters tether and a special setup with two rolling blocks for reducing the weight of the implant and the cable.

2.2.2.5. Contextual fear conditioning

Shortly, all mice were first recorded in a neutral context (CC-, 5 min) and then 2 hour later they were put into a conditioned context (CC+, 5 min) and given 3x footshocks, each with 0.5 mA, 1 s in duration, starting at minute 2 and separated by 1 min. Two contexts, CC+ and CC- were different in terms of walls (squared black-and-white pattern versus grey color), smell (different cleaning solutions) and CC+ had a metal grid (to deliver footshock), while CC- had a white plastic floor. Next day after contextual fear conditioning, for retrieval sessions, all mice were first put into CC+ for 5 min, then 2 hours later in CC- for 5 min. contextual fear conditioning memory in retrieval sessions was measured as amount of time (%) mice were freezing in CC+ and CC-. Freezing of mice was defined as total immobility of animals (except for breathing) with a characteristic tense fearful posture. The analysis of data was done by using AnyMaze software. Fear conditioning system was a touch-pad controller and a conditional sound-attenuated cabinet and chambers from Ugo Basile, Italy.

2.2.2.6. Local field potential and units' activity recordings

Intrahippocampal local field potentials (LFPs) were recorded by using a digital electrophysiological 64 channels recording system (Neuralynx, USA) with its original electrophysiological data acquisition software Cheetah (Neuralynx, USA). Multi-unit activity was sampled at 32 KHz at wide-band 0.1 Hz - 10 kHz range filter, and stored at the local network server. To be able to record a mouse in rather big open field (50x50 cm) we used a long (5 m) tether (Neuralynx) counterbalanced with an equal weight (20-30 g) of the headstage and the cable itself via a simple 2x rolling blocks system, that the mouse can freely move without any discomfort. To prevent twisting the tether cable over 10 min of recording, the cable must be at least 2 m long from the point where it is connected to the mouse to the point at the ceiling where it counterbalanced with the 2x blocks system.

2.2.2.7. *In vivo recordings analysis*

2.2.2.7.1. *Network activity*

Treatment and processing of signals was carried out in off-line mode using Spike2 software (Cambridge Electronic Design). To remove the 50 Hz AC noise, original wide-band recordings of the network activity with sampling rate 32 kHz were processed using forward fast Fourier transform (FFT), the power of 50 Hz component and its harmonics was set to 0, and the inverse FFT was applied to reconstruct the signals. Obtained records were low-pass filtered (gain 350 Hz) and down-sampled to 1 kHz (factor 32), and used for further analysis of the theta and gamma oscillatory activity. For analysis of the network oscillations in the theta (5.0 - 12.5 Hz) and gamma (30.0 - 100.0 Hz) frequency bands, LFP signals in individual electrodes were integrated for each tetrode in each animal. The spectral power of oscillatory components in the frequency range 0 - 500 Hz was obtained using sliding FFT (2^{11} points in 2.048 s epochs, Welch's method). For within- and between-group comparison, spectral power in each frequency bin was averaged per recorded area (DG or CA3) and side (left or right) and normalized for each animal to corresponding baseline value (taken as 100%).

2.2.2.7.2. *Units activity*

Action potentials were detected in a band-pass filtered signal (0.5 - 10.0 kHz) without 50 Hz noise. Events within a window of 1.25 ms (40 points at 32 kHz) with a magnitude exceeding 6 standard deviation above mean were detected, and spike waveforms were extracted and stored for further classification. Spike sorting using principal component analysis (PCA) was followed by visual inspection and manual adjustment of clusters. Later, the mean firing rate for classified units in the DG and CA3, as well as bursting properties for units in the DG with the mean bursting rate ≥ 0.5 burst/min, were computed. Units with the mean firing rate < 0.05 Hz were considered as inactive and discarded from analysis. The following burst criteria were used: number of spikes ≥ 2 , first ISI to trigger burst ≤ 20 ms. Finally, the spike shapes of obtained units were visually inspected, and inhibitory neurons were identified basing on their higher firing rate (generally above 10 Hz) and shorter latency as compared to respective values in principal cells. Throughout the text, the data only for putative excitatory neurons are presented as mean \pm s.e.m.

Statistical analysis included non-parametric Mann-Whitney U-test for single unit activity and ANOVA/MANOVA followed by Bonferroni *post hoc* test for spectral power of theta and gamma oscillations.

3. Results

3.1. *In vitro* experiments

3.1.1. Introduction to T-type channel antagonists

Pharmacological blockers have often a limited specificity, therefore I used in the present work different antagonists to confirm the implication of T-type channels in the studied phenomena. Ni²⁺ is a washable, easy to use, water-soluble component that principally acts by blocking the channels pore (Kang et al., 2006; Obejero-Paz et al., 2008). Ni²⁺ selectively blocks T-type channels at low micromolar concentrations over high-voltage calcium channels, but can also block R-type calcium channels in similar concentration range (Zamponi et al., 1996; Lee et al., 1999). In addition, Ni²⁺ can block voltage-gated sodium channels but at much higher concentrations (Yamamoto et al., 1993). Mibefradil is water-soluble and acts, as Ni²⁺, by competing with calcium at the pore level. It blocks T-type channels at low micromolar concentrations (Brogden and Markham, 1997; Martin et al., 2000; Strege et al., 2005; Huang et al., 2015) and similarly to Ni²⁺, Mibefradil at higher micromolar concentrations can also block L-type calcium channels (Brogden and Markham, 1997; Martin et al., 2000; Huang et al., 2015) or affect voltage-gated sodium channels (Eller et al., 2000; McNulty and Hanck, 2004; Strege et al., 2005). Despite the relatively close potency of mibefradil block on T-type, L-type and voltage-gated sodium channels, mibefradil most potent effect is on T-type channels (Strege et al., 2005). The inhibition of L-type channels by mibefradil has been shown to be caused by an hydrolyzed metabolite of its methoxy acetate side chain (Wu et al., 2000; Li et al., 2005). To address this issue, NNC 55-0396, a derivative of mibefradil lacking this methoxy acetate side chain has been created (Huang et al., 2004; Li et al., 2005). So far, no strong effect of NNC 55-0396 on sodium channels have been reported, making it a highly selective blocker of T-type channels (Huang et al., 2004; Alviña et al., 2009; Chen et al., 2010). TTA-A2 is the newest component with the highest selectivity for T-type channels with a potency roughly 300 times superior on T-type over high-voltage activated calcium channels (Kraus et al., 2010; Francois et al., 2013). TTA-A2 acts by maintaining T-type channels in an inactivated state (Kraus et al., 2010; Francois et al., 2013) and its high specificity for T-type has been recently suggested to be due to its action on a binding site not conserved between the T-type family and L-type channels (Chavez-Colorado et al., 2016). Up to date, no block of R-type or voltage-gated sodium channels by TTA-A2 has been evidenced. Unfortunately, TTA-A2 is hardly soluble in water-based solutions and tends to stick to organic materials such as plastic tubing, making its use trickier than the previous ones. In addition, TTA-A2 has only recently been commercially

available. The TTA-A2 I used in my experiments was a kind gift from Dr. Emmanuel Bourinet, Institut de Génomique Fonctionnelle, Montpellier, France.

To conclude, I used all four different T-type blockers to confirm the specific involvement of T-type channels and rule out as much as possible any side effects on R-type channels and other high-voltage activated calcium channels, notably L-type, and voltage-gated sodium channels.

3.1.2. mGCs exhibit low-threshold high frequency burst firing blocked by T-type channels antagonists

During the course of the work presented in this thesis, I used different species and strains of rodents, mostly Wistar Han rats but also wild type (WT) C57BL/6J mice and Ca_v3.2 KO mice, in which the gene coding for the Ca_v3.2 subtype of T-type channels was constitutively removed. Recordings were done in most of the experiments at a room temperature of 25°C but also at 32°C for additional characterization of rats mGCs firing phenotype and for recordings of mice brain slices. The following parts present results obtained from Wistar Han rats at a recording temperature of 25°C.

My first aim was to assess the firing phenotype of mGCs in response to somatic current injection, in control conditions (CTR) or when blocking T-type channels (Figures 6A and 6B, see materials and methods). In CTR conditions, I observed that mGCs produced high-frequency burst firing of usually two APs from the weakest stimulation that elicited APs (R+0, see methods) followed by single spikes elicited at slower frequencies and with a tonic pattern (Figures 6B). For the rest of the text, the term of burst-firing of mGCs will represent a short-time framed generation of APs (most often 2 APs in experiments performed at 25°C) at significantly higher frequencies than other APs of the discharge, resulting in a visual segregation of mGCs APs generation patterns (Figure 6C) and in a segregation of the interspike intervals (ISI) values (Figure 6C and 6D). To obtain a more stable firing and more APs for quantification, and because it still arguably represents a low/mild physiological stimulation, I chose the step R+1, corresponding to R+0 plus 40pA for analysis (Figure 6B and 6C). Measuring the ISIs between the 1st and 2nd APs (1st ISI) and 4th and 5th APs (4th ISI) of the discharge, I quantified the firing phenotype of mGCs, as indicated in the materials and methods and Figure 6C. The average value of mGCs 1st ISI at R+1 was around 18 ms (corresponding to an instantaneous frequency of the second AP of the discharge around 55 Hz) whereas the 4th ISI average frequency was around 40 ms (corresponding to an instantaneous frequency of the fifth AP of the discharge around 25 Hz) (Figure 6D left; 1st ISI average: 17.94 ± 1.701 ms; n=25 versus 4th ISI average: 41.07 ± 2.500 ms; n = 22; P < 0.0001; Wilcoxon signed rank test).

Remarkably, mGCs incubated with ACSF containing 100 μM Ni^{2+} rarely exhibited burst firing but rather a constantly tonic pattern of APs at lower frequencies (Figures 6C and 6D right; 1st ISI average: 31.12 ± 1.885 ms; n=26 versus 4th ISI average: 38.00 ± 1.697 ms; n = 26; $P < 0.0001$; Wilcoxon signed rank test). The predominant occurrence of burst firing in the first spikes of the discharge and the absence of effect of Ni^{2+} on later-coming, non-bursting spikes correlates well with the fast voltage-dependent inactivation of T-type channels (Perez-Reyes, 2003) which are thus likely to affect only the initial spikes of the discharge in my protocol due to the strong inactivation caused by the 250 ms-long depolarization. I quantified as well the ratio between the 1st and 4th ISI and plotted the frequency distribution of this ISI ratio (Figure 6E). ISI ratios of mGCs recorded in CTR conditions were centered around 0.5; reflecting the heterogeneity of APs frequencies between bursts and tonic spikes whereas ISI ratios of mGCs recorded in 100 μM Ni^{2+} were centered around 1, reflecting the relatively constant and tonic mode of firing of these cells (Figure 6E; $P < 0.0001$; χ^2 test). This difference in firing phenotype was due to a strong block of mGCs burst firing by 100 μM Ni^{2+} , which caused an almost 2-fold increase in the average ISI between 1st and 2nd spike (Figure 6F left; CTR 1st ISI average: 17.94 ± 1.701 ms; n = 25; versus 100 μM Ni^{2+} 1st ISI average: 31.12 ± 1.885 ms; n = 26; $P < 0.0001$; Mann-Whitney U-test), bringing the instantaneous frequency of the 2nd spike down to around 30 Hz, value close to non-bursting spikes in CTR conditions (Figures 6D and 6F). 100 μM Ni^{2+} had no significant effect on the ISI of later-coming APs that were already non-bursting in CTR conditions (Figure 6F right; CTR 4th ISI average: 41.07 ± 2.500 ms; n = 22 versus 100 μM Ni^{2+} 4th ISI average: 38.00 ± 1.697 ms; n = 26; $P = 0.303$; unpaired T-test). These effects of 100 μM Ni^{2+} on mGCs firing were further confirmed with the other T-type blockers (Figure 7, Mibefradil: 3 μM , Mibefradil 1st ISI average: 36.45 ± 2.642 ms; n = 32 versus CTR 1st ISI average: 22.42 ± 3.739 ms; n = 20; $P = 0.0010$; Mann-Whitney U-test. 3 μM Mibefradil 4th ISI average: 38.10 ± 1.636 ms; n = 24 versus CTR 4th ISI average: 43.66 ± 3.591 ms; n = 18; $P = 0.1332$; Unpaired T-test. TTA-A2: 1 μM TTA-A2 1st ISI average: 26.57 ± 2.451 ms; n = 18 versus CTR 1st ISI average: 16.18 ± 2.451 ms; n = 15; $P = 0.0079$; Mann-Whitney U-test. 1 μM TTA-A2 4th ISI average: 29.78 ± 2.289 ms; n = 12 versus CTR 4th ISI average: 36.68 ± 3.243 ms; n = 13; $P = 0.1027$; Unpaired T-test. NNC 55-0396: 50 μM NNC 55-0396 1st ISI average: 46.97 ± 3.738 ms; n = 14 versus CTR 1st ISI average: 27.14 ± 4.250 ms; n = 20; $P = 0.0018$; Mann-Whitney U-test. 50 μM NNC 55-0396 4th ISI average: 46.37 ± 2.637 ms; n = 9 versus CTR 4th ISI average: 42.19 ± 4.628 ms; n = 14; $P = 0.4687$; Mann-Whitney U-test).

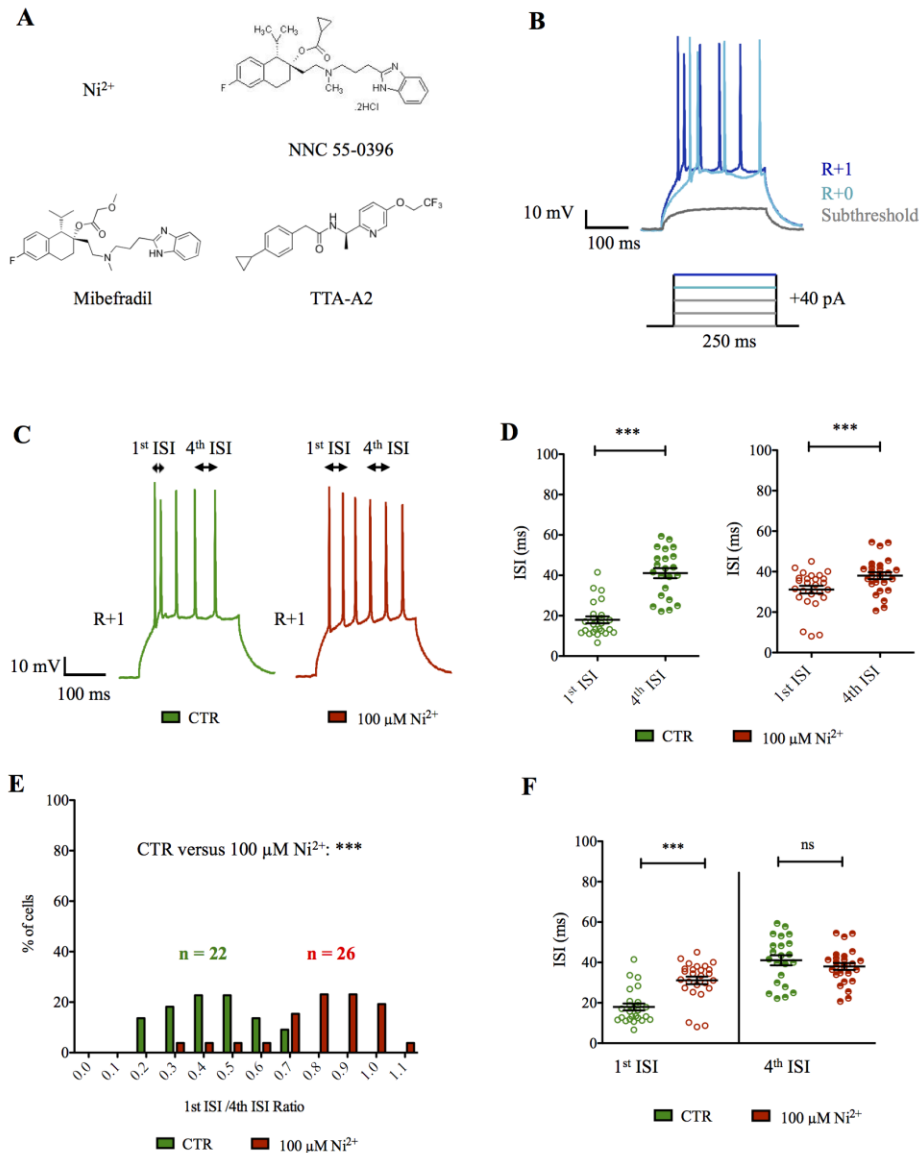


Figure 6: Characterization of mGCs firing phenotype in control conditions or upon pharmacological blockade of T-type channels. **A:** The four different T-type channels blockers used in my experiments. **B:** Stimulation protocol and corresponding mGCs response. Cells were stimulated with 250 ms-long direct somatic current injection of increasing 40 pA intensity. The first stimulation intensity producing firing of mGCs was named R+0 and the next step of 40 pA stronger stimulation was named R+1. R+1 was preferentially used for characterization of mGCs firing phenotype. **C:** Illustrative traces representing the firing of mGCs at R+1 in CTR conditions or when T-type channels were blocked using bath application of 100 μM Ni^{2+} . Arrows indicate the ISIs quantified for analysis. **D:** Quantification of the 1st and 4th ISI as indicated in C, in CTR conditions or in 100 μM Ni^{2+} . Asterisks and “ns” indicate results of Wilcoxon signed rank tests of 1st versus 4th ISI comparison. *** $P < 0.001$. **E:** Frequency distribution plot of the ratio 1st ISI/4th ISI used to quantify the bursting versus non-bursting character of mGCs firing. A low ratio indicates a heterogeneous, bursting discharge whereas a high ratio indicates a more homogeneous, tonic mode of firing. Asterisks indicate the results of χ^2 test comparison of ISIs ratios frequency distribution between CTR and Ni^{2+} groups. *** $P < 0.0001$. **F:** Direct comparison of the values of 1st and 4th ISIs between CTR and Ni^{2+} groups. Asterisks and “ns” indicate results to Mann-Whitney U-test or unpaired T-test comparison, depending on the normality of each data set. *** $P < 0.0001$. Error bars indicate s.e.m.

All together, these results indicate that mGCs can fire bursts of high-frequency APs following small and mild stimulations and that this burst firing is controlled by T-type calcium channels.

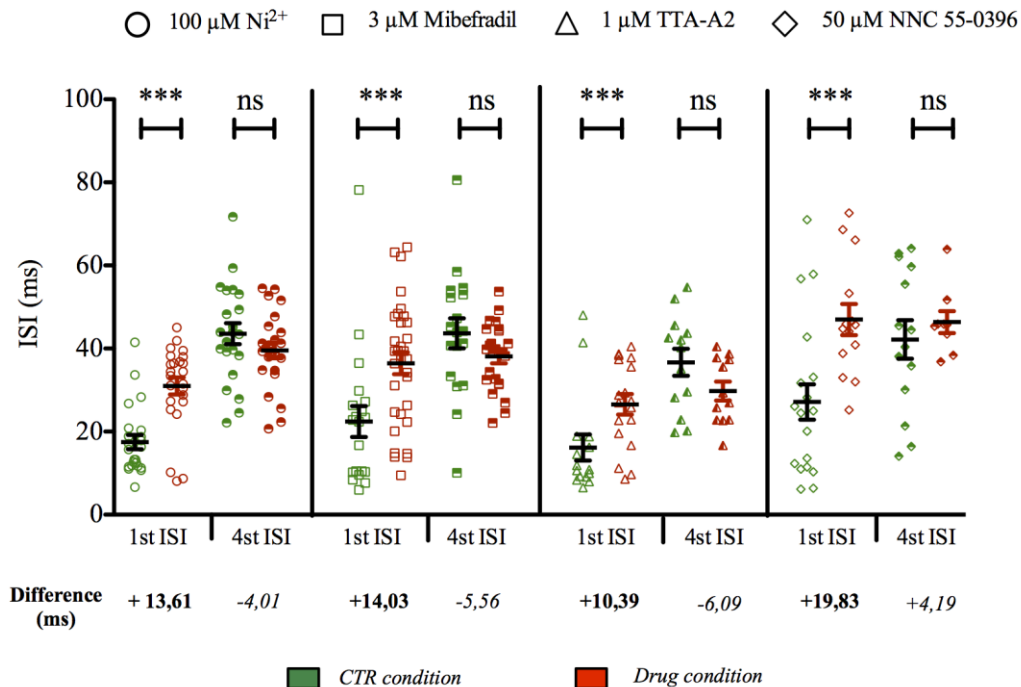


Figure 7: Quantification of the effects of four different T-type channels blockers on mGCs firing. Different symbols shapes represent different experimental groups, with 1st ISI presented as clear symbols and 4th ISI as half-filled symbols from individual cells. Green and red colors indicate CTR and drug-treated conditions, respectively. Within experimental groups, CTR and drug-treated cells were recorded from slices prepared from the same animals. Asterisks and “ns” indicate results of Mann-Whitney U-test or unpaired T-test comparison of CTR versus drug-treated data sets for 1st and 4th ISI, depending on the normality of each data set. *** P < 0.001. Error bars indicate s.e.m.

3.1.3. T-type channels blockers do not affect AP threshold and overall mGCs excitability

There was the concern of unspecific effects of the T-type blockers on sodium channels. To assess whether this suppression of burst firing was a specific mechanism or was due to some global changes in mGCs excitability I quantified the number of APs produced by the cells following increasing stimulation, the current injection intensity required to reach R+0 in each cell and the threshold of the 1st and 2nd AP at R+0 and R+1 (Figure 8). There was no difference between CTR cells and cells recorded in presence of 100 $\mu\text{M Ni}^{2+}$ in the number of APs (Figure 8A; CTR n = 25; 100 $\mu\text{M Ni}^{2+}$ n = 26; Comparison of Boltzmann Sigmoid fits: null hypothesis: one curve for all data sets; alternative hypothesis: different curve for each data set; P = 0.9243; conclusion with 95% confidence: do not reject null hypothesis); neither in the current injected to reach R+0 (Figure 8B; CTR current average: 150.4 ± 7.035 pA; n=25 versus 100 $\mu\text{M Ni}^{2+}$

current average: 147.7 ± 6.935 pA; $n = 26$; $P = 0.785$; Unpaired T-test), nor in APs threshold: (Figure 8C; 1st AP: R+0 CTR threshold average: -35.63 ± 0.76 mV; $n = 23$ versus $100 \mu\text{M Ni}^{2+}$ threshold average: -35.60 ± 0.80 mV; $n = 24$; $P = 0.523$; Mann-Whitney U-test. 1st AP: R+1 CTR threshold average: -35.29 ± 0.82 mV; $n = 23$ versus $100 \mu\text{M Ni}^{2+}$ threshold average: -35.69 ± 0.91 mV; $n = 24$; $P = 0.807$; Mann-Whitney U-test. 2nd AP: R+0 CTR threshold average: -32.27 ± 0.61 mV; $n = 23$ versus $100 \mu\text{M Ni}^{2+}$ threshold average: -33.88 ± 0.80 mV; $n = 21$; $P = 0.173$; Mann-Whitney T-test. 2nd AP: R+1 CTR threshold average: -29.75 ± 0.606 mV; $n = 23$ versus $100 \mu\text{M Ni}^{2+}$ threshold average: -31.66 ± 0.70 mV; $n = 24$; $P = 0.106$; Mann-Whitney U-test). The trend for the threshold of the 2nd AP to be higher in CTR conditions than in $100 \mu\text{M Ni}^{2+}$ reflects the impact of burst firing in CTR conditions, where the 2nd spike is triggered when voltage-gated sodium channels implicated in the generation of the 1st AP are not fully recovered from inactivation. This is well illustrated by the trace in figure 6B, where the 2nd spike exhibits smaller amplitude. The width of the 2nd (bursting) AP was also slightly larger in these conditions (not quantified).

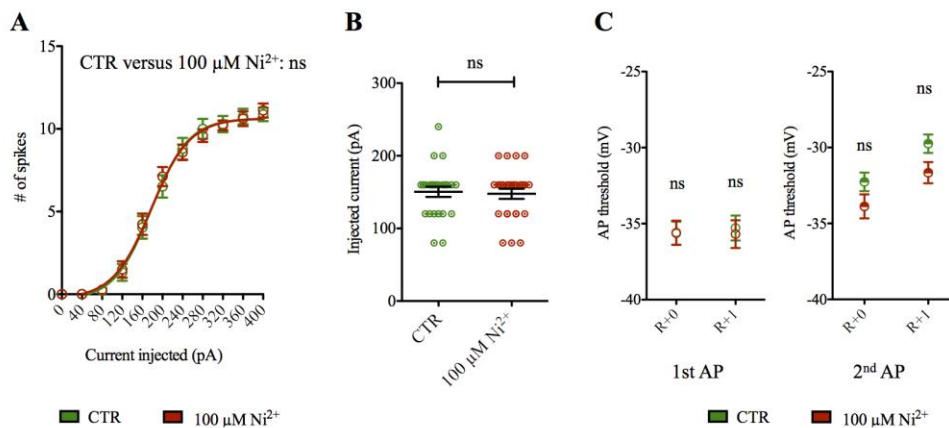


Figure 8: T-type blockade with $100 \mu\text{M Ni}^{2+}$ does not affect the general excitability of mGCs. **A:** Number of APs produced by mGCs in response to increasing somatic current injection. Symbols indicate average values for each stimulation intensity in CTR versus Ni^{2+} condition and curves represent Boltzmann sigmoid fits of both datasets. “ns” indicate the result of the comparison of Boltzmann fits with hypothesis “different curve for each data set”. Error bars indicate s.e.m. **B:** Minimal injected current required to reach R+0 in CTR versus Ni^{2+} condition. “ns” indicate the result of unpaired T-test. Error bars indicate s.e.m. **C:** Comparison of 1st and 2nd AP threshold in CTR versus Ni^{2+} condition, at R+0 and R+1. “ns” indicate the result of Mann-Whitney U-test. Error bars indicate s.e.m.

These results indicate that suppression of this form of mGCs burst firing, as I define it, by T-type antagonists is unlikely to be caused by unwanted side-effects on sodium channels. In addition, they suggest that the mechanisms controlling this form of mGCs burst firing are independent from the ones regulating the general excitability of these cells, such as those defining the AP threshold.

3.1.4. mGCs burst firing is an intrinsic excitability mechanism

As T-type channels can localize at the level of synapses, pre and post-synaptically (Urban et al., 1998; Wu and Leung, 1998; Weiss and Zamponi, 2013; Ly et al., 2016), I wanted to determine if T-type blockers effects on mGCs burst firing were due to alterations in network interactions, such as feedback inhibition and feed-forward inhibition (Amaral et al., 2007; Paz and Huguenard, 2015) or rather to intrinsic excitability mechanisms. I therefore repeated similar experiments but in the presence of 10 μM CNQX, 50 μM D-AP5 and 20 μM bicuculline, a classical cocktail of synaptic transmission blockers. As in previous experiment (Figure 7), T-type blockers induced a strong block of burst firing as quantified by the 1st ISI (Figure 9; 100 μM Ni^{2+} : CTR 1st ISI average: 16.73 ± 1.917 ms; n = 23 versus 100 μM Ni^{2+} 1st ISI average: 27.24 ± 2.785 ms; n = 24; P = 0.0035; Unpaired T-test. 3 μM mibefradil: CTR 1st ISI average: 20.90 ± 2.294 ms; n = 28 versus 3 μM mibefradil 1st ISI average: 28.99 ± 2.188 ms; n = 25; P = 0.0136; Mann-Whitney U-test. 1 μM TTA-A2: CTR 1st ISI average: 14.33 ± 1.661 ms; n = 40 versus 1 μM TTA-A2 1st ISI average: 27.06 ± 2.053 ms; n = 45; P < 0.0001; Mann-Whitney U-test. 50 μM NNC 55-0396: CTR 1st ISI average: 19.96 ± 2.229 ms; n = 20 versus 50 μM NNC 55-0396 1st ISI average: 43.35 ± 2.999 ms; n = 18; P < 0.0001; Unpaired T-test). There was a small effect on the 4th ISI for mibefradil and NNC 55-0396, but the effect was not consistent among the blockers (Figure 9; 100 μM Ni^{2+} : CTR 4th ISI average: 30.86 ± 2.789 ms; n = 23 versus 100 μM Ni^{2+} 4th ISI average: 31.03 ± 1.817 ms; n = 23; P = 0.5980; Mann-Whitney U-test. 3 μM mibefradil: CTR 4th ISI average: 42.36 ± 2.591 ms; n = 26 versus 3 μM mibefradil 4th ISI average: 34.90 ± 1.402 ms; n = 23; P = 0.0485; Mann-Whitney U-test. 1 μM TTA-A2: CTR 4th ISI average: 30.61 ± 1.661 ms; n = 40 versus 1 μM TTA-A2 4th ISI average: 27.06 ± 2.053 ms; n = 45; P < 0.3166; Mann-Whitney U-test. 50 μM NNC 55-0396: CTR 4th ISI average: 35.40 ± 1.939 ms; n = 20 versus 50 μM NNC 55-0396 4th ISI average: 42.87 ± 2.139 ms; n = 14; P = 0.0159; Unpaired T-test).

These results indicate that mGCs burst firing is an intrinsic excitability mechanism not due to network interactions such as feedback inhibition. To continue studying mGCs intrinsic excitability in isolation from the network, all following experiments were conducted in the presence of CNQX, D-AP5 and bicuculline, with the exception of medial perforant path stimulation experiments that were done in the presence of bicuculline only.

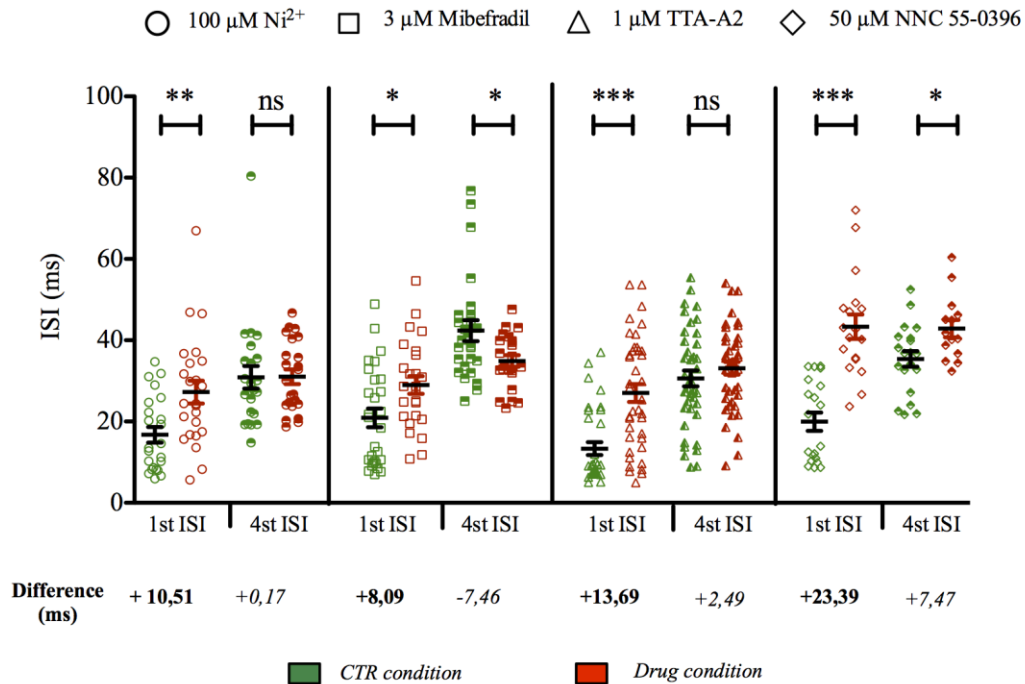


Figure 9: Quantification of the effects of four different T-type channels blockers on mGCs firing, in the presence of synaptic blockers. The data is presented as in figure 7. Asterisks and “ns” indicate results to Mann-Whitney U-test or unpaired T-test comparison of CTR versus drug-treated data sets for 1st and 4th ISI and within each experimental group, depending on the normality of each data set. *** P < 0,001. ** P < 0.01. * P < 0.05. Error bars indicate s.e.m.

3.1.5. mGCs burst firing is not determined by AP after-depolarization

An intrinsic excitability mechanism that can support burst firing is the after-depolarization (ADP); a rebound of depolarizing potential that follows APs and that is partly caused by activation of somatodendritic calcium channels (Jensen et al., 1996; Metz et al., 2005). To test whether mGCs burst firing was supported by similar mechanism, I assessed the effect of my T-type blockers on the ADP and the correlation between the ADP and burst firing, as quantified with the 1st ISI. Single spikes were elicited by brief somatic current injection and the amplitude of the following ADP was measured at its peak and after 20 ms, corresponding to the average timing of the 2nd spike in bursts of 50 Hz as quantified in figure 6 (Figure 10A, see materials and methods). There was overall no difference in ADP amplitude neither at its peak nor after 20 ms in CTR conditions and when T-type channels were blocked with the antagonists (Figure 10B; 100 μM Ni^{2+} : CTR ADP 6 ms average: 23.06 ± 0.56 mV; n = 20 versus 100 μM Ni^{2+} ADP 6 ms average: 21.26 ± 0.68 mV; n = 21; P = 0.1031; Mann-Whitney U-test. CTR ADP 20 ms average: 11.35 ± 0.46 mV; n = 20 versus 100 μM Ni^{2+} ADP 20 ms average: 11.25 ± 0.58 mV; n = 21; P = 0.7842; Mann-Whitney U-test. 1 μM TTA-A2: CTR ADP 6 ms average: 23.24 ± 0.55 mV; n = 38 versus 1 μM TTA-A2 ADP 6 mV average: 23.12 ± 0.43 mV; n = 42; P = 0.4789; Mann-Whitney U-test. CTR ADP 20 ms average: 9.795 ± 0.48 mV; n = 38

versus 1 μM TTA-A2 ADP 20 ms average: 11.30 ± 0.4772 mV; $n = 42$; $P = 0.0288$; Mann-Whitney U-test. 50 μM NNC 55-0396: CTR ADP 6 ms average: 24.79 ± 0.65 mV; $n = 18$ versus 50 μM NNC 55-0396 ADP 6 ms average: 23.12 ± 0.43 mV; $n = 42$; $P = 0.4617$; Unpaired T-test. CTR ADP 20 ms average: 15.65 ± 0.63 mV; $n = 18$ versus 50 μM NNC 55-0396 ADP 20 ms average: 15.92 ± 0.52 mV; $n = 17$; $P = 0.7438$; Unpaired T-test). Furthermore, there was no positive correlation between the amplitude of the ADP at 6 or 20 ms and the 1st ISI at step R+1 quantified from the $\Delta 40$ protocol tested in the same cells in CTR conditions (Figure 10C; Linear regression fits, p-value characterizes the test to the hypothesis slope is significantly non-zero. ADP 6 ms all CTR: $n = 76$; $R^2=0.0045$; $F = 3,647$; $P = 0.06$. ADP 20 ms all CTR: $n = 76$; $R^2 = 0.0353$; $F = 2.71$ $P = 0.104$).

Together, these results indicate that the ADP does not control mGCs burst firing.

3.1.6. R and L-type channels blockers do not affect mGCs burst firing

To further confirm the involvement of T-type channels and further rule out any ADP-mediated burst mechanism, I tested the effect of R-type and L-type calcium channels blockers on mGCs burst firing (SNX-482 and nifedipine, respectively). R-type calcium channels are classified as high-voltage activated but can also activate at low-medium range voltages in certain conditions (Wormuth et al., 2016). In addition, R-type channels get functionally blocked by Ni^{2+} in similar concentration range as T-type channels, as noted previously (Zamponi et al., 1996; Lee et al., 1999). They have been involved in CA1 pyramidal cells ADP-controlled burst firing (Metz et al., 2005) and have been found localized at the level of the AIS of dorsal cochlear nucleus interneurons, in a location strategic to regulate neuronal firing (Bender and Trussell, 2009a). L-type calcium channels are mostly known as high-voltage activated channels, but the $\text{Ca}_v1.3$ subtype of this family has been shown to exhibit low-voltage activation properties (Lipscombe et al., 2004) and could also mediate low-threshold calcium fluxes controlling the mGCs burst firing that I describe. Neither 10 μM nifedipine nor 500 nM SNX-482 suppressed mGCs burst firing as quantified with the 1st ISI measured from $\Delta 40$ pA somatic injection protocol (Figure 11, clear symbols; 10 μM nifedipine: CTR 1st ISI average: 15.52 ± 2 ms; $n = 20$ versus 10 μM nifedipine 1st ISI average: 20.06 ± 2.8 ms; $n = 18$; $P = 0,299$; Mann-Whitney U-test. 500 nM SNX-482: CTR 1st ISI average: 21.33 ± 4.18 ms; $n = 18$ versus 500 nM SNX-482 1st ISI average: 18.15 ± 2.50 ; $n = 18$; $P = 0,99$; Mann-Whitney U-test). SNX-482 induced a significant reduction in the 4th ISI, possibly reflecting the impact of $\text{Kv}4.3$ blockade (Kimm and Bean, 2014) (Figure 11, half-filled triangles; 500 nM SNX-482: CTR 4th ISI average: 45.19 ± 3.31 ms; $n = 14$ versus 500 nM SNX-482 4th ISI average: 36.70 ± 2.17 ; $n = 18$; $P = 0.034$;

Unpaired T-test) but nifedipine had no significant effect (Figure 11, half-filled circles; 10 μ M nifedipine: CTR 4th ISI average: 35.04 ± 3.51 ms; n = 20 versus 10 μ M nifedipine 4th ISI average: 41.90 ± 2.85 ms; n = 17; P = 0.148; Unpaired T-test).

These results support a specific effect of T-type channels in mGCs burst firing and further rule out a role of the ADP.

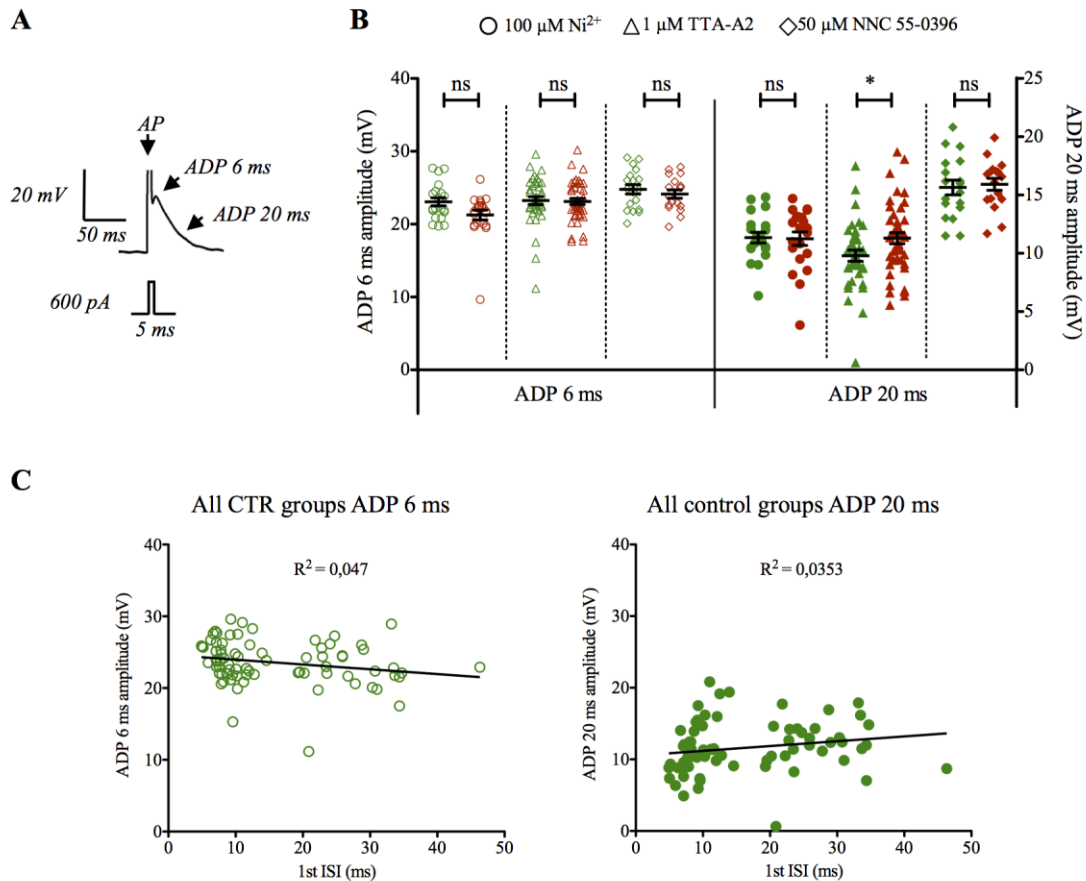


Figure 10: Effect of T-type channel blockers on spike ADP and correlation between ADP amplitude and burst firing. **A:** Illustrative scheme and trace representing the protocol to elicit and measure the ADP at its maximum (6 ms after AP peak) and at a time point corresponding to the theoretical upcoming of a 2nd AP at 50 Hz (20 ms after AP peak). **B:** Impact of T-type channels antagonists on ADP measured at 6 or 20 ms after AP peak. Symbols shapes represent different experimental groups. Green and red colors indicate CTR values and drug-treated values. Clear and half-filled symbols represent amplitude of the ADP at 6 and 20 ms after AP peak, respectively. Asterisks and “ns” indicate results to Mann-Whitney U-test or unpaired T-test comparison of CTR versus drug-treated data sets for ADP amplitudes and within each experimental group, depending on the normality of each data set. * P < 0.05. Error bars indicate s.e.m. **C:** Correlation between 1st ISI and ADP amplitude 6 and 20 ms after AP peak, quantified from same cells. Values from mGCs recorded in CTR conditions of the three experimental groups Ni²⁺, TTA-A2 and NNC 55-0396 were pooled together. Symbols indicate individual values and black bars represent linear regression fits. R² of linear fits are indicated on the figure.

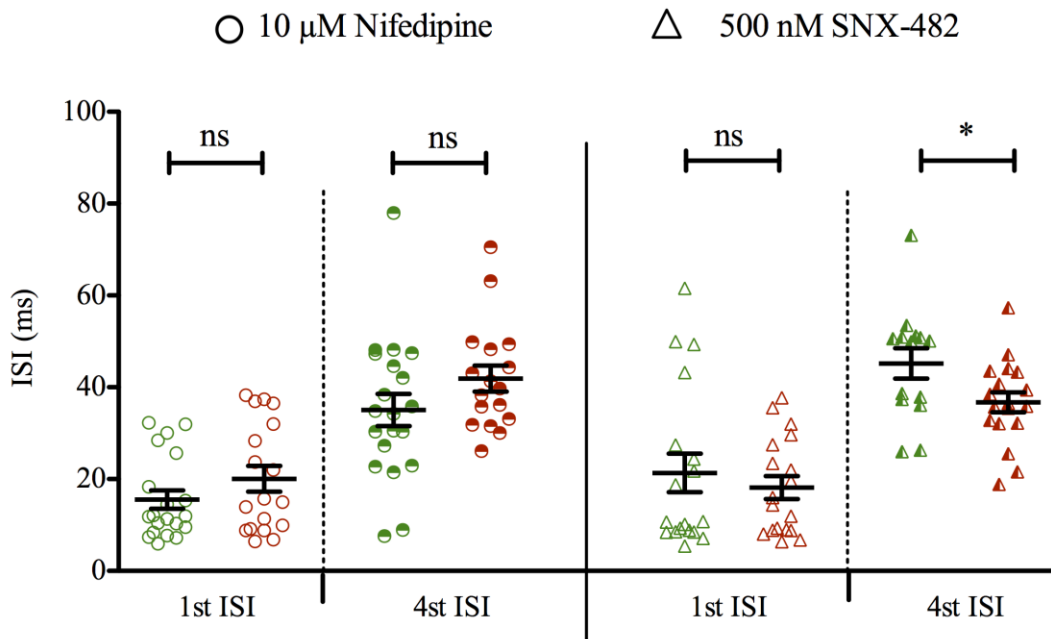


Figure 11: Effect of L-type and R-type calcium channels blockers nifedipine and SNX-482 on mGCs firing. Green and red colors represent CTR and drug-treated conditions. Circles represent values values of 1st (clear circles) and 4th ISI (half-filled circles) for the nifedipine group. Triangles represent values of 1st (clear triangles) and 4th ISI (half-filled triangles) for the SNX-482 group. Asterisks and “ns” indicate results to Mann-Whitney U-test or unpaired T-test comparison of CTR versus drug-treated data sets, depending on the normality of each data set. * P < 0.05. Error bars indicate s.e.m.

3.1.7. T-type channels exhibit specific patterns of distribution in dendrites and proximal axon of mGCs

I then indirectly assessed the distribution of T-type channels in dendrites and axon of mGCs by comparing the calcium fluxes in CTR conditions or in the presence of T-type blockers (mibefradil and NNC 55-0396), with the help of 2-photon microscopy (Figure 12A and 13A). To elicit calcium fluxes measurable up to distal parts of dendrites and axon, and mimicking the burst-firing mode, I stimulated mGCs with short somatic current injection producing a duplet of APs at 50 Hz (Figure 12B, see materials and methods) that reliably propagated in the cell processes. Using this suprathreshold protocol, two different patterns of T-type mediated calcium fluxes in dendrites and axon were apparent (Figure 12C and 12D). In the dendrites, T-type calcium channels-mediated calcium fluxes were observed throughout the segments scanned, up to the maximal distance assessed in my experiments: 120 μm away from the soma (Figure 12C; 0-60 μm CTR $\Delta G/R$ average: 0.956 ± 0.096 ; n = 29 versus 0-60 μm 3 μM Mibefradil $\Delta G/R$ average: 0.563 ± 0.057 ; n = 15; P = 0.0079; unpaired T-test; and versus 0-60 μm 50 μM NNC 55-0396 $\Delta G/R$ average: 0.421 ± 0.057 ; n = 11; P = 0.0024; unpaired T-test. 60-120 μm CTR $\Delta G/R$ average: 0.906 ± 0.134 ; n = 21 versus 60-120 μm 3 μM Mibefradil $\Delta G/R$ average: 0.353 ± 0.078 ; n = 5; P = 0.023; Mann-Whitney U-test; and versus 60-120 μm

50 μM NNC 55-0396 $\Delta\text{G/R}$ average: 0.185 ± 0.080 ; $n = 3$; $P = 0,029$; Mann-Whitney U-test). There was a trend suggesting that T-type channels-mediated calcium fluxes increase with distance to the soma but it appeared not significant, possibly due to the limited number of data points for these farther distances (0-60 μm CTR $\Delta\text{G/R}$ average: 0.956 ± 0.096 ; $n = 29$ versus 60-120 μm CTR $\Delta\text{G/R}$ average: 0.906 ± 0.134 ; $n = 21$; $P = 0,76$; unpaired T-test. 0-60 μm 3 μM Mibefradil $\Delta\text{G/R}$ average: 0.563 ± 0.057 ; $n = 15$ versus 60-120 μm 3 μM Mibefradil $\Delta\text{G/R}$ average: 0.353 ± 0.078 ; $n = 5$; $P = 0.067$; Mann-Whitney U-test. 0-60 μm 50 μM NNC 55-0396 $\Delta\text{G/R}$ average: 0.421 ± 0.057 ; $n = 11$ versus 60-120 μm 50 μM NNC 55-0396 $\Delta\text{G/R}$ average: 0.185 ± 0.080 ; $n = 3$; $P = 0,061$; Mann-Whitney U-test). In the axon, T-type channels-mediated calcium fluxes seemed to be restricted to the proximal axon, up to 60 μm away from the soma (Figure 12D; 0-60 μm CTR $\Delta\text{G/R}$ average: 1.129 ± 0.096 ; $n = 29$ versus 0-60 μm 3 μM Mibefradil $\Delta\text{G/R}$ average: 0.563 ± 0.24 ; $n = 20$; $P < 0,0001$; unpaired T-test; and versus 0-60 μm 50 μM NNC 55-0396 $\Delta\text{G/R}$ average: 0.404 ± 0.054 ; $n = 6$; $P = 0.0023$; unpaired T-test. 60-140 μm CTR $\Delta\text{G/R}$ average: 1.01 ± 0.135 ; $n = 14$ versus 60-140 μm 3 μM Mibefradil $\Delta\text{G/R}$ average: 0.867 ± 0.145 ; $n = 5$; $P = 0,571$; Mann-Whitney U-test and versus 60-140 μm 50 μM NNC 55-0396 $\Delta\text{G/R}$ average: 0.434 ± 0.163 ; $n = 4$; $P = 0,063$; Mann-Whitney U-test).

This protocol allowed me to measure calcium fluxes along axon and dendrites as it produces a robust depolarization of membrane potential that propagated to distal cellular compartments. However, it can produce activation of high-voltage calcium channels and lead to important calcium influx in the cell. Because calcium sensitive-dyes diffuse more in the cytoplasm than the unbound calcium itself (Gabso et al., 1997; Sabatini et al., 2002), this can potentially lead to an overestimated and artificially spread definition of calcium fluxes distribution.

Thus, to refine the characterization of T-type mediated calcium fluxes, I conducted a second subset of experiments consisting in blocking voltage-gated sodium channels with 1 μM TTX and stimulating mGCs with subthreshold stimulations using the $\Delta 40$ pA protocol described previously (Figure 13A and 13B). Care was taken to not depolarize the cell further than -20 mV, providing maximal T-type channels activation with limited activation of HVA channels (Zhang et al., 2000; Perez-Reyes, 2003; Pourbadie et al., 2017). Due to limited propagation of such subthreshold depolarization along neuronal membrane, this protocol was used only to more accurately assess T-type channels-mediated calcium fluxes in the proximal axon.

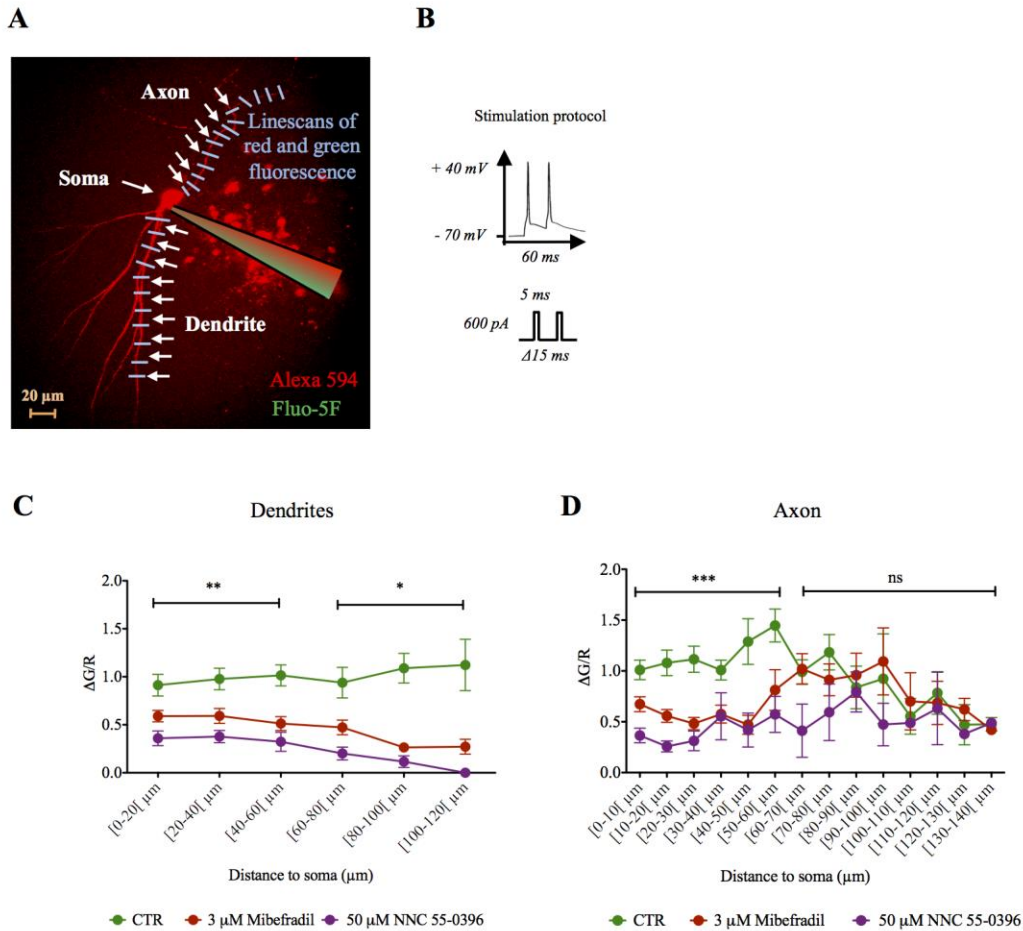


Figure 12: T-type mediated calcium fluxes in mGCs dendrites and axon elicited by a duplet of AP at 50 Hz frequency. **A:** Illustrative picture of a mGC filled with the volume marker Alexa 594 and the low-affinity calcium-sensitive dye Fluo-5F as visualized with 2-photon microscopy (z-stack, maximum projection). Position of the axon, soma and one dendrite are indicated with white arrows. Blue lines schematize the linescans of green and red fluorescence along mGC axon and dendrite. **B:** Illustrative scheme of the stimulation protocol to elicit a duplet of AP at 50 Hz and corresponding mGC firing. **C:** Values of peak green fluorescence normalized by red fluorescence measured from linescans across dendrites. Data were grouped by segments of 20 μm increasing distance to the soma. Green, red and purple colors indicate values from CTR group and groups in which T-type channels were blocked with 3 μM Mibefradil or 50 μM NNC 55-0396, respectively. Asterisks indicate common results of Mann-Whitney or unpaired T-test comparison between CTR and drug-treated groups of averaged values for distances of 0–60 μm and 60 – 120 μm away from the soma. * P < 0.05. ** P < 0.01. Error bars indicate s.e.m. **D:** Values of peak green fluorescence normalized by red fluorescence measured from linescans across the axon. Data were grouped by segments of 10 μm increasing distance to the soma. Green and red and purple colors code similarly for conditions as in C. Asterisks and “ns” indicate common results of Mann-Whitney U-test or unpaired T-test comparison between CTR and drug-treated groups of averaged values for distances of 0–60 μm and 60 – 140 μm away from the soma. *** P < 0.001. Error bars indicate s.e.m.

Using this protocol, I evidenced T-type-mediated calcium fluxes that were restricted to a location situated 15.5 – 30 μm away from the soma (Figure 13B; Hillock CTR Max ΔG/R average: 0.427 ± 0.056 ; n = 6 versus Hillock 100 μM Ni²⁺ Max ΔG/R average: 0.422 ± 0.063 ; n = 7; P = 1.000; Mann-Whitney U-test. [5-15.5 μm] CTR Max ΔG/R average: 0.200 ± 0.058 ; n = 6 versus [5-15.5 μm] 100 μM Ni²⁺ Max ΔG/R average: 0.117 ± 0.030 ; n = 5; P = 0.329;

Mann-Whitney U-test. [15.5-30 μm] CTR Max $\Delta\text{G/R}$ average: 0.117 ± 0.030 ; $n = 5$ versus [15.5-30 μm] 100 $\mu\text{M Ni}^{2+}$ Max $\Delta\text{G/R}$ average: 0.134 ± 0.02 ; $n = 6$; $P = 0.0112$; Mann-Whitney U-test. [30-51 μm] CTR Max $\Delta\text{G/R}$ average: 0.0278 ± 0.020 ; $n = 7$ versus [30-51 μm] 100 $\mu\text{M Ni}^{2+}$ Max $\Delta\text{G/R}$ average: 0.166 ± 0.071 ; $n = 5$; $P = 0,091$; Mann-Whitney U-test), strongly correlating with the position of the AIS as it has been determined in dentate gyrus granule cells (Schmidt-Hieber and Bischofberger, 2010).

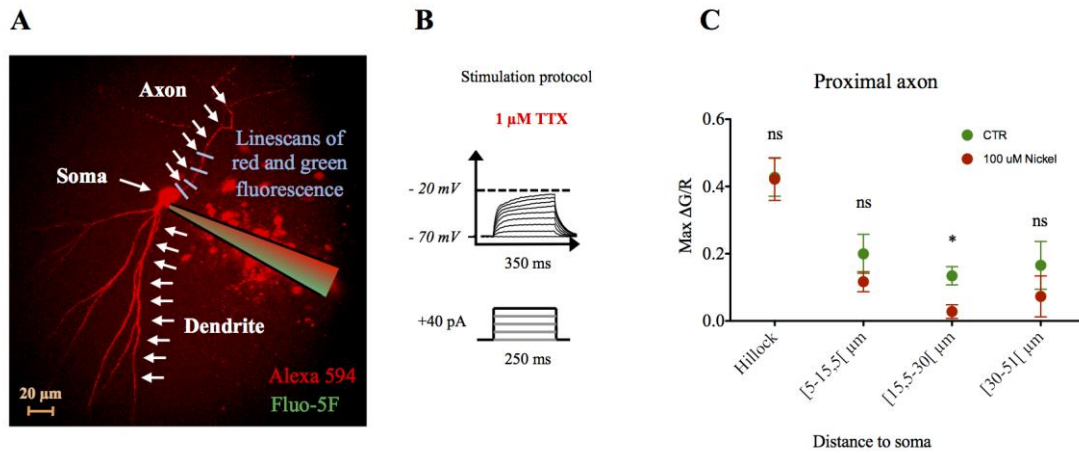


Figure 13: T-type mediated calcium fluxes in mGCs proximal axon elicited by subthreshold stimulations. **A:** Illustrative picture of a mGC with blue lines schematizing the linescans of green and red fluorescence along mGC proximal axon. **B:** Illustrating scheme of the stimulation protocol and corresponding effect on mGC Vm. Cell were stimulated with 250 ms-long somatic current injection of 40 pA increasing intensity reproducing the protocol initially used to characterize mGC firing phenotypes and calcium fluxes were measured for each stimulation-induced depolarization of the cells. **C:** Averages of maximum green fluorescence elicited by intracellular injection bringing cells Vm to between -45 mV and -20 mV measured from linescans across the proximal axon and normalized by red fluorescence, in cells recorded in CTR conditions (green filled circles) or upon blockade of T-type channels with bath application of 100 $\mu\text{M Ni}^{2+}$ (red filled circles). Data were grouped in 4 segments corresponding to linescans at the level of the axon hillock and at distances between 5-15.5 μm , 15.5-30 μm and 30-51 μm away from the soma. Asterisks and “ns” indicate results of Mann-Whitney U-test comparison between CTR and 100 $\mu\text{M Ni}^{2+}$ averages for each proximal axon location. * $P < 0.05$. Error bars indicate s.e.m.

Together, these results indicate that T-type channels are distributed throughout the dendrites up to distances scanned in my experiments (120 μm away from the soma) and are concentrated at the level of the AIS in the proximal axon. My data suggest an increasing gradient of T-type mediated calcium fluxes with distance to the soma within the dendrites. This could reflect an increasing concentration of T-type channels, an enhancement of their functional state, or an increased degree of partnering with -and calcium-mediated regulation of- other calcium sources (Moreno et al., 2016).

3.1.8. AIS-localized T-type channels control mGCs burst firing

Having established that T-type-mediated calcium fluxes are present in the dendrites and the AIS, I then wanted to determine which of these channel population is involved in controlling mGCs burst firing. The lack of the correlation between the ADP and the burst firing (Figure 9) already suggested that dendritic T-type channels might not be implicated in this mechanism but the involvement of AIS-localized T-type still needed to be demonstrated. For this, I performed targeted blockade of T-type channels at the level of the AIS by applying local puffs of Ni^{2+} through a micro-pressure system onto the axon, 20 μm away from the soma while simultaneously recording the firing phenotype of mGCs (Figure 14A). A first protocol consisted in testing the effect of increasingly long puffs from 100 ms to 800 ms on firing of mGCs as compared with pre-puff and post-wash firing of mGCs (Figure 14B, materials and methods). Increasing puffs of 10 mM Ni^{2+} onto the AIS induced an impairment of burst firing as quantified by measuring the 1st ISI (Figure 6A). The strongest effect was attained with 700 and 800 ms-long puffs that brought down the instantaneous frequency of the 2nd AP of the discharge from an average CTR frequency of ~ 70 Hz to ~ 30 Hz (Figure 15A, right, blue full circles; All CTR 1st ISI average: 12.73 ± 0.783 ms; $n = 8$ versus 700-800 ms Ni^{2+} puff 1st ISI average: 30.61 ± 4.797 ; $n = 8$; $P = 0.0083$; paired T-test). This block of burst firing was paralleled by an increase in delay of appearance of APs following stimulation, as quantified for the 1st spike AP delay (Figure 15A, right, patterned grey circles; All CTR latency to 1st AP average: 48.34 ± 3.313 ms; $n = 8$ versus 700-800 ms Ni^{2+} puff latency to 1st AP average: 68.87 ± 13.36 ms $n = 8$; $P = 0.0391$; Wilcoxon signed rank test). There was a weak but significant correlation between the increase in 1st ISI and latency to 1st spike, raising the concern that block of burst firing might be caused by an increase of spike threshold in this experiment (Figure 15B; Linear regression fits, p-value characterizes the test to the hypothesis slope is significantly non-zero. $n = 72$; $R^2=0.1838$; $F=15.76$; $P = 0.0002$). Indeed, quantification of the threshold for the 1st AP evidenced this Ni^{2+} -mediated gradual impairment (Figure 15C; All CTR relative 1st threshold: 0.0077 ± 0.082 mV; $n = 8$ versus 700-800 ms Ni^{2+} relative 1st AP threshold: 1.97 ± 0.512 mV $n = 8$; $P = 0.0023$; Wilcoxon signed rank test). In comparison, control experiments consisting in puffing a vehicle solution composed of ACSF without T-type antagonist to the axon and puffing 10 mM Ni^{2+} onto proximal dendrites, similarly 20 μm from the soma, had little to no effect on mGCs firing (Figure 15D and 18E; Vehicle: All vehicle CTR 1st ISI average: 11.66 ± 1.17 ms; $n = 4$ versus 700-800 ms vehicle puff 1st ISI average: 9.62 ± 0.58 ; $n = 4$; $P = 0.125$; Wilcoxon signed rank test; all vehicle CTR latency to 1st AP average: 51.89 ± 7.73 ms; $n = 4$ versus 700-800 ms vehicle puff latency to 1st AP average: 42.49 ± 5.602 ms $n = 4$; $P = 0.125$; Wilcoxon signed rank test. 10 mM Ni^{2+} dendrites: All dendrites Ni^{2+} CTR 1st ISI average: 10.33 ± 1.463 ms; $n = 4$ versus 700-800 ms Ni^{2+} puff 1st ISI average: 13.30 ± 3.441 ; $n = 4$; $P = 0.25$; Wilcoxon signed rank test; all dendrites Ni^{2+} CTR latency to 1st AP average:

65.52 ± 8.154 ms; $n = 4$ versus 700-800 ms Ni^{2+} puff latency to 1st AP average: 66.93 ± 10.03 ms $n = 4$; $P = 0.625$; Wilcoxon signed rank test).

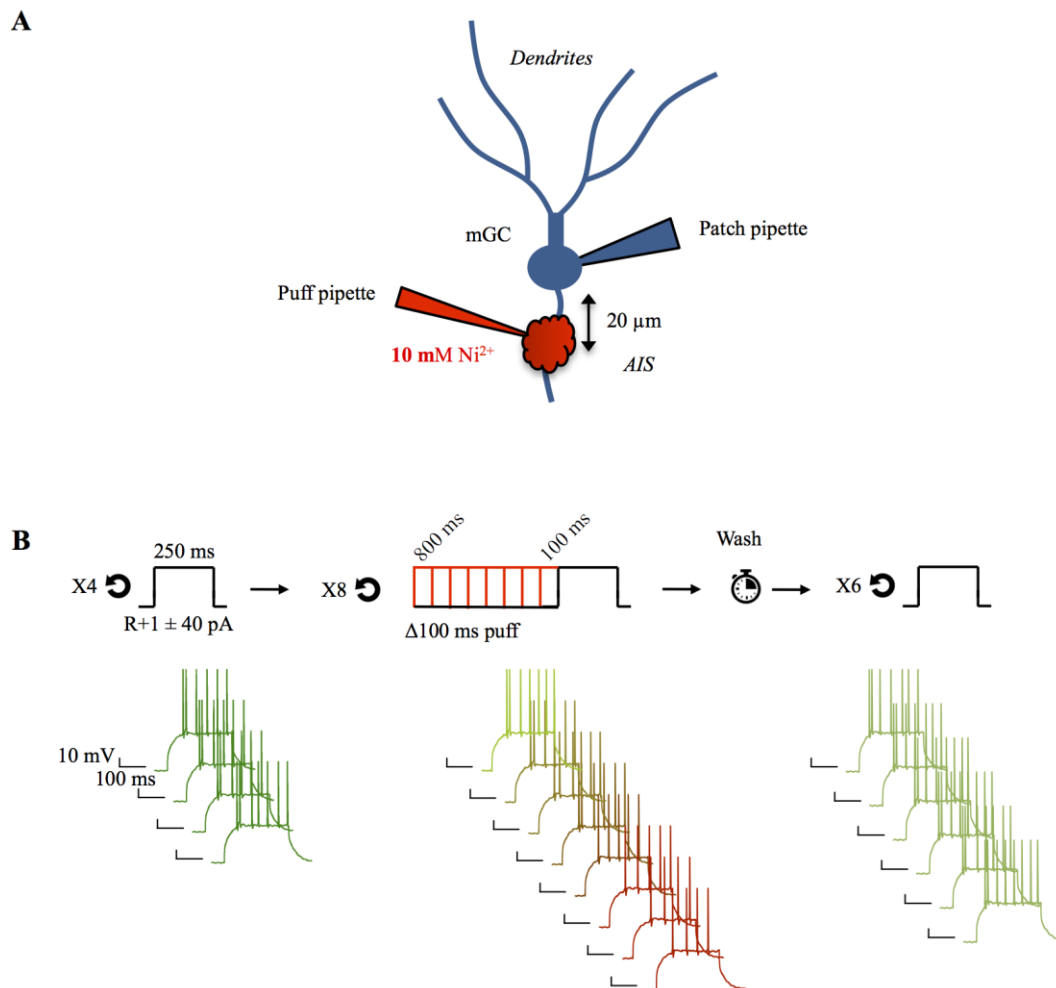


Figure 14: Effect of gradually increasing Ni^{2+} local puff onto mGCs AIS: general view. **A:** Illustrative scheme representing a mGC recorded and stimulated through a patch pipette while a second pipette filled with extracellular solution containing 10 mM Ni^{2+} and connected to a micro-pressure system is used to locally block T-type channels at the level of the AIS (20 μm away from the soma). **B:** Schemes representing the stimulation and puff protocol and corresponding traces from one mGCs. *Left:* a 250 ms-long current injection of intensity equal to $R+1 \pm 20$ pA, as determined for each cell prior to puff manipulations; was used to trigger mGC's firing. This protocol was repeated 4 times to obtain the firing phenotype of the cells in CTR conditions. *Center:* The stimulation was repeated 8 times and paired with increasingly long puffs of 10 mM Ni^{2+} , from 100 ms to 800 ms ($\Delta 100$ ms) finishing just before the depolarizing current injection. *Right:* wash of the Ni^{2+} was monitored with repeated stimulations and once stable, 6 repeats of the protocol were stored for analysis.

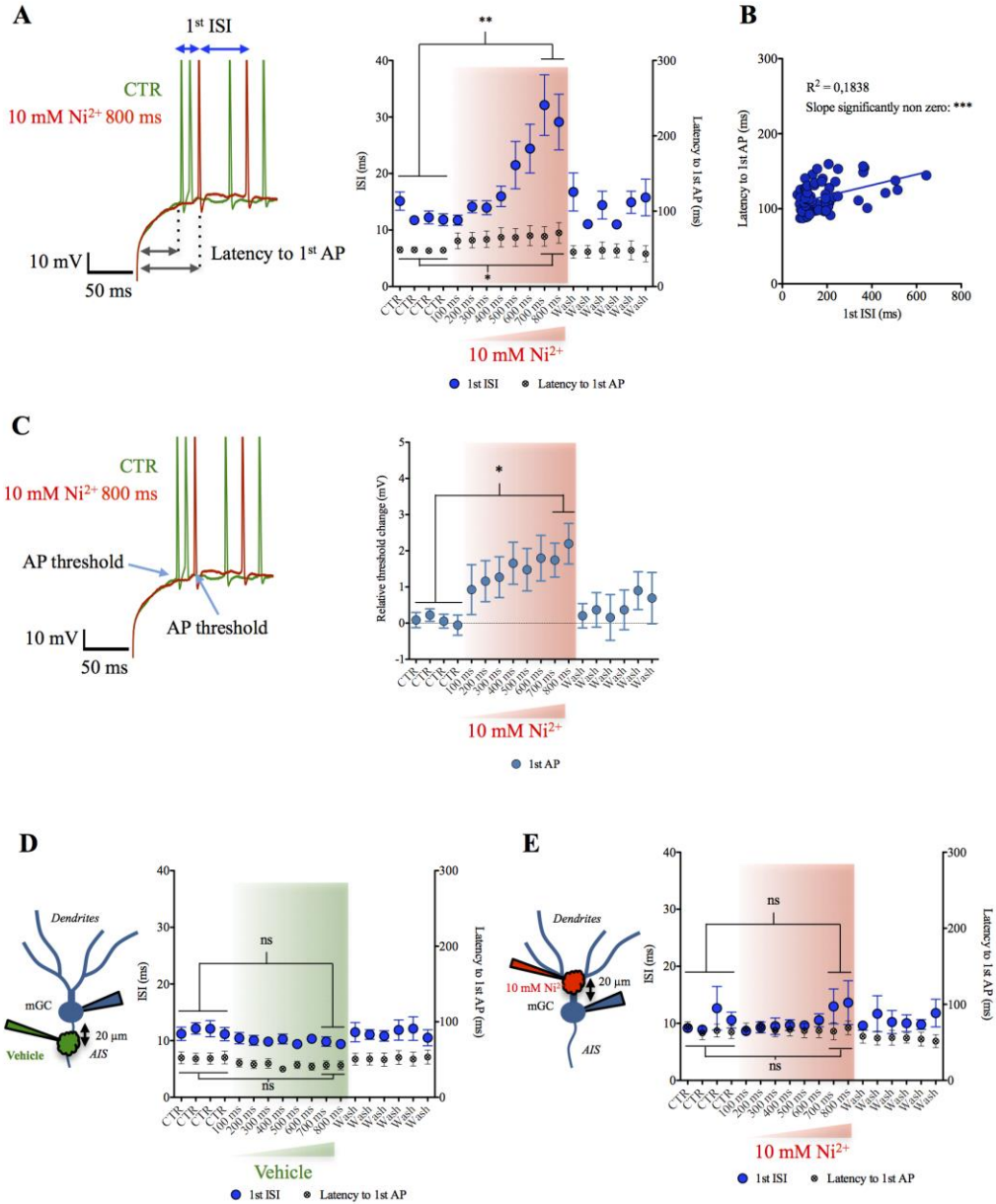


Figure 15: Effect of gradually increasing Ni²⁺ local puff onto mGCs AIS: quantification and control experiments. **A:** *Left:* superimposed traces of initial firing of mGC in one CTR recording and following 800 ms-long puff of 10 mM Ni²⁺ onto the AIS. Arrows and dotted lines indicate the firing parameters measured for quantification, the 1st ISI and the timing of appearance of the 1st AP following the start of the somatic current injection stimulation, termed latency to 1st AP. Note the important increase of 1st ISI and the noticeable increase of the latency to 1st AP. *Right:* Values of 1st ISI (blue full circles) and latency to 1st spike (grey patterned circles) over the course of the CTR, puff and wash parts of the protocol, averaged from the sequential traces of all cells (n=7). Red gradient highlights the increasing length of puff, meaning in fine the increasing concentration of Ni²⁺ applied onto the AIS. Asterisks indicate the results of Wilcoxon signed rank test between the average of the 4 CTR and the average of 700 and 800 ms-long puffs. ** P < 0.01. * P < 0.05. Error bars indicate s.e.m. **B:** Correlation between 1st ISI and latency to 1st spike. Blue filled circles indicate individual values from same cells (n = 72) and the blue line represents the linear regression fit of the data set. R² is indicated on the figure. Result of the test to the hypothesis “slope is significantly non-zero” is indicated on the figure. *** P < 0.001. **C:** *Left:* superimposed traces of initial firing of mGC in one CTR recording and following 800 ms-long puff of 10 mM Ni²⁺ onto the AIS. Arrows indicate the AP threshold measured for quantification. *Right:* Quantification of the 1st AP threshold over the course of the experiment. Asterisks indicate the results of Wilcoxon signed rank test between the average of the 4 CTR and the average of 700 and 800 ms-long puffs. * P < 0.05. Error bars indicate s.e.m. **D:** Puff of vehicle solution onto the AIS. 1st ISI and latency

to 1st AP are quantified as in A. “ns” indicate the results of Wilcoxon signed rank test between the average of the 4 CTR and the average of 700 and 800 ms-long puffs. Error bars indicate s.e.m. **E:** Puff of 10 mM Ni²⁺ onto proximal dendrites, 20 μm away from the soma. “ns” indicate the results of Wilcoxon signed rank test between the average of the 4 CTR and the average of 700 and 800 ms-long puffs. Error bars indicate s.e.m.

Because I did not observe any changes in AP threshold with bath application of 100 μM Ni²⁺ (Figure 8) and because I used 10 mM Ni²⁺ for local application, a concentration that can affect voltage-gated sodium channels (Yamamoto et al., 1993), I hypothesized that the combined effect of AIS-puffs of Ni²⁺ on burst firing, AP latency and AP threshold in this experiment was due to cumulative block of T-type channels and sodium channels by acute high concentration of Ni²⁺. To address this issue, I empirically determined optimal ranges of puff length and interval between puff and intracellular current injection for individual cells and quantified the effect on 1st ISI, and AP threshold in repeated trials of this protocol (Figure 16). This protocol allowed me to produce a strong block of mGCs burst firing with no to minimal changes of the latency to 1st AP and 1st AP threshold (Figure 17; CTR 1st ISI average: 11.73 ± 0.79 ms; n = 4 versus 10 mM Ni²⁺ 1st ISI average: 28.86 ± 3.478 ms; n = 4 versus Wash 1st ISI average: 12.25 ± 1.024. P = 0,0417; Friedman test. Dunn’s multiple comparison tests: CTR versus 10 mM Ni²⁺ P < 0.05. CTR versus Wash: P > 0.05. CTR latency to 1st AP average: 32.90 ± 5.363 ms; n = 4 versus 10 mM Ni²⁺ 1st ISI average: 36.36 ± 7.622 ms; n = 4 versus Wash 1st ISI average: 29.54 ± 5.523. P = 0.0694; Friedman test. CTR 1st AP relative threshold average: -1.184e-015 ± 1.389e-015 mV; n = 4 versus 10 mM Ni²⁺ 1st ISI average: 1.228 ± 0.8669 mV; n = 4 versus Wash 1st ISI average: -1.438 ± 0.7254. P = 0,0694; Friedman test). A likely explanation of these results is that the empirically defined length of both puff and puff-stimulation interval allows to apply on the axon a concentration of Ni²⁺ that remains high enough to block T-type channels at the time of the stimulation, whereas the concentration required to block sodium channels is rapidly washed away. However, a dual effect of T-type channels on mGCs firing, an acute change in AP threshold and a more long-lasting effect of burst firing cannot be completely excluded. Because I never notified any changes in AP threshold in the bath application of T-type antagonists’ experiments, I preferentially support the former hypothesis.

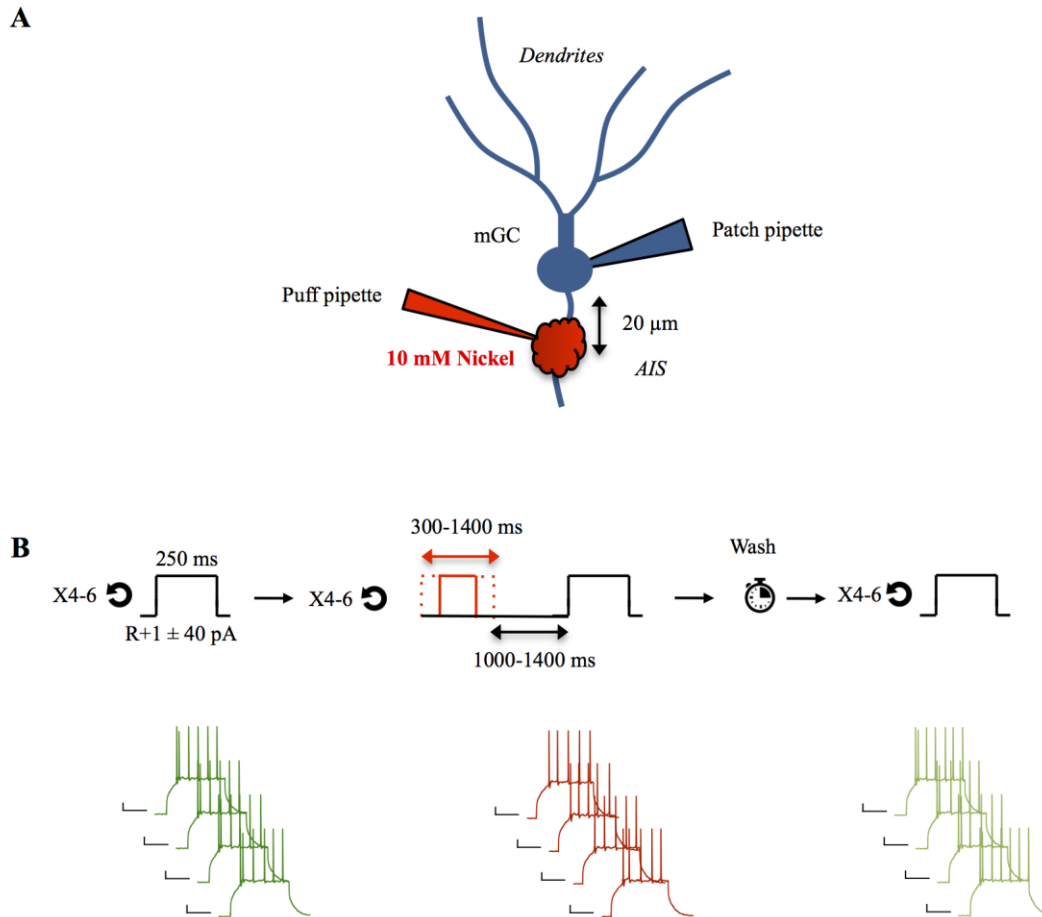


Figure 16: Effect of empirically defined Ni^{2+} local puff onto mGCs AIS: general view. **A:** Illustrating scheme of a mGC during experiment. **B:** Schemes representing the stimulation and puff protocol and corresponding traces from one mGCs. *Left:* cells are stimulated with current injection corresponding to $R+1 \pm 20$ pA for 4-6 repeats prior to puff to obtain CTR firing. *Center:* The stimulation is repeated 4-6 times and paired with puffs of 10 mM Ni^{2+} of fixed duration, interleaved with the current injection depolarization for a fixed duration. The precise values of puff and puff-stimulation interval were determined empirically for each cell, based on the length of puff producing the highest block of burst firing with the gradually increasing puff protocol. *Right:* wash of the Ni^{2+} is monitored with repeated stimulations and once stable, 4-6 repeats of the protocol were stored for analysis.

All together, these results demonstrate T-type channels localized at the level of the axon initial segment control burst firing of mGCs and further suggest that this mechanism does not involve modulation of AP threshold.

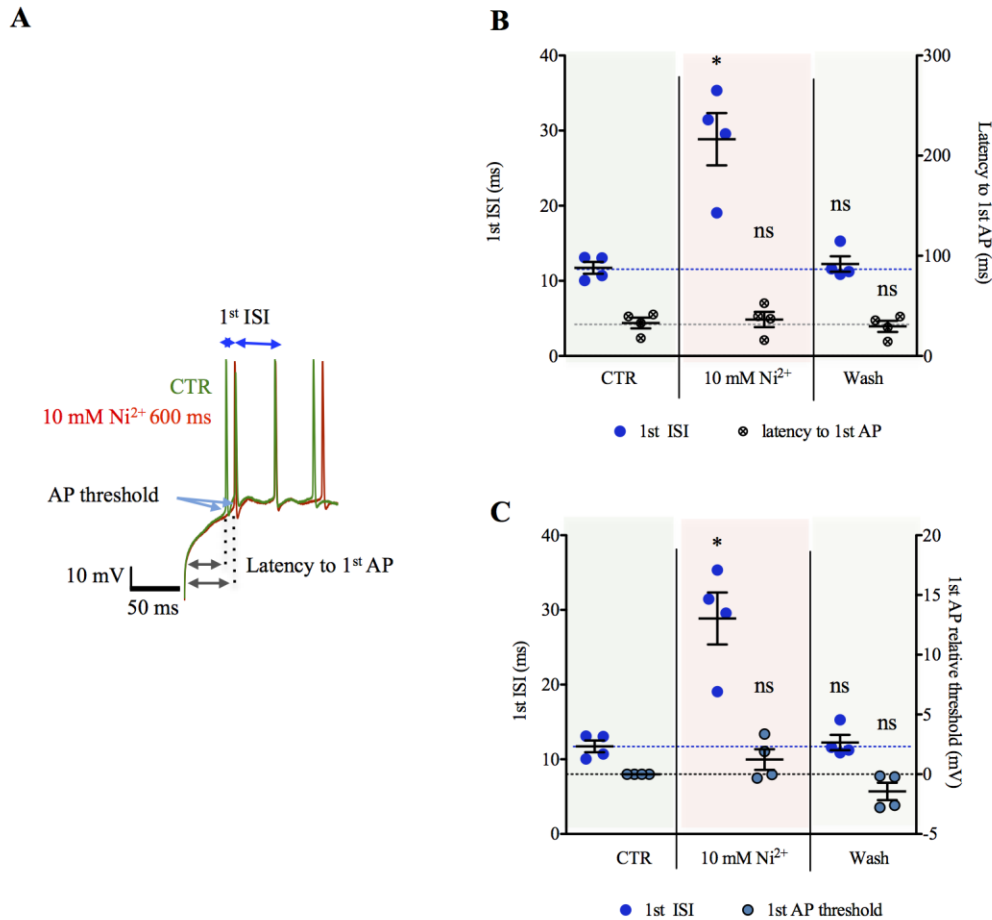


Figure 17: Effect of empirically defined Ni²⁺ local puff onto mGCs AIS: quantification. Effect of gradually increasing Ni²⁺ local puff onto mGCs AIS: quantification and control experiments. **A:** Superimposed traces of initial firing of mGC in one CTR recording and following 600 ms puff of 10 mM Ni²⁺ onto the AIS, 1000 ms prior to stimulation. Arrows and dotted lines indicate the firing parameters measured for quantification, the 1st ISI, the latency to 1st AP and the 1st AP threshold. Note the important increase of 1st ISI and the minimal increase of the latency to 1st AP. **B:** Values of 1st ISI (blue full circles) and latency to 1st spike (grey patterned circles) over the course of the CTR, puff and wash parts of the protocol, averaged from the repeated traces of all cells (n = 4). Green, red and greenish background highlights the CTR, puff and wash conditions, respectively. Asterisks and “ns” indicate the results of Friedman test followed by Dunn’s multiple comparison tests for each data set. * P-value <0,05. Error bars indicate s.e.m. **C:** Values of 1st ISI (blue full circles) and 1st AP threshold (light blue full circles) over the course of the CTR, puff and wash parts of the protocol, averaged from the repeated traces of all cells (n = 4). Asterisks and “ns” indicate the results of Friedman test followed by Dunn’s multiple comparison tests for each data set. * P < 0.05. Error bars indicate s.e.m.

3.1.9. mGCs burst firing frequency reaches 100 Hz and more at physiological temperatures

In my experiments performed at a recording temperature of 25°C, the T-type-mediated burst firing of mGCs that I characterized at R+1 in my somatic current injection protocol had an average frequency of ~50-60 Hz (Figure 6D, Figure 7). Because the frequency of granule cells burst firing recorded *in vivo* had a frequency of ~150 Hz (Pernía-Andrade and Jonas, 2014), I wanted to determine the impact of T-type channels on mGCs firing at more

physiological temperatures. For this, I recorded mGCs at 32°C and assessed their firing phenotype in response to somatic current injection in CTR conditions or in the presence of the T-type channels antagonists Ni²⁺ and TTA-A2. Compared to 25°C, burst firing in CTR conditions was much more pronounced at 32°C and reached frequencies of ~140 Hz (Figure 18A and 18B; 25°C CTR 1st ISI average: 16.73 ± 1.917 ms; n = 23 versus 32°C CTR 1st ISI average: 6.934 ± 1.449 ms; n = 8; P = 0.0007; Mann-Whitney U-test). The frequency distribution plot of the 1st / 4th ISI ratio also illustrates the difference in firing phenotype of mGCs at 32°C compared to 25°C (Figure 18C, P < 0.0001; χ^2 test). In addition, burst firing at 32°C was not always restricted to the initial spikes of the discharge and two or (less often) multiple episodes of burst firing could be observed over the 250 ms length of the stimulation, separated by short periods of electric silence (Figure 18D). In addition, whereas bursts mostly comprised only 2 APs in experiments made at 25°C, bursts elicited by mGCs recorded at 32°C regularly contained 3 APs (Figure 18D). These results correlate well with the enhanced recovery from inactivation of T-type channels at these temperatures (Iftinca et al., 2006) which will thus be more available to mediate multiple episodes of burst firing in my 32°C experiments as compared to 25°C. Moreover, it parallels the observations of Pernía-Andrade and Jonas who showed that burst firing is the preferential mode of activity of mGCs *in vivo* (Pernía-Andrade and Jonas, 2014).

Finally, the effect of the T-type antagonists Ni²⁺ and TTA-A2 on mGCs firing was similar at 32°C as at 25°C, with a strong reduction of the 1st ISI and no effect on the 4th ISI (Figure 18E and 21F, 32°C CTR 1st ISI average: 6,934 ± 1,449 ms; n=8 versus 32°C Ni²⁺ 1st ISI average: 21.91 ± 2.3 ms; n = 8; P = 0.0003; Mann-Whitney U-test and versus 32°C TTA-A2 1st ISI average: 24.66 ± 3.049 ms; n = 8; P = 0.0003; Mann-Whitney U-test. 32°C Ni²⁺ 1st ISI average: 21.91 ± 2.3 ms; n = 8; versus 32°C TTA-A2 1st ISI average: 24.66 ± 3.049 ms; n = 8; P = 0.4827; Unpaired T-test; 32°C CTR 4th ISI average: 25.44 ± 5.013 ms; n = 8 versus 32°C Ni²⁺ 4th ISI average: 23.01 ± 2.704 ms; n = 8; 32°C TTA-A2 4th ISI average: 31.78 ± 3.499 ms; n = 8; P = 0,2745; 1-way ANOVA).

Together, these results indicate that T-type channels mediate very high-frequency firing at physiological temperatures and parallels observations *in vivo* suggesting that burst firing is the preferential mode of activity of mGCs.

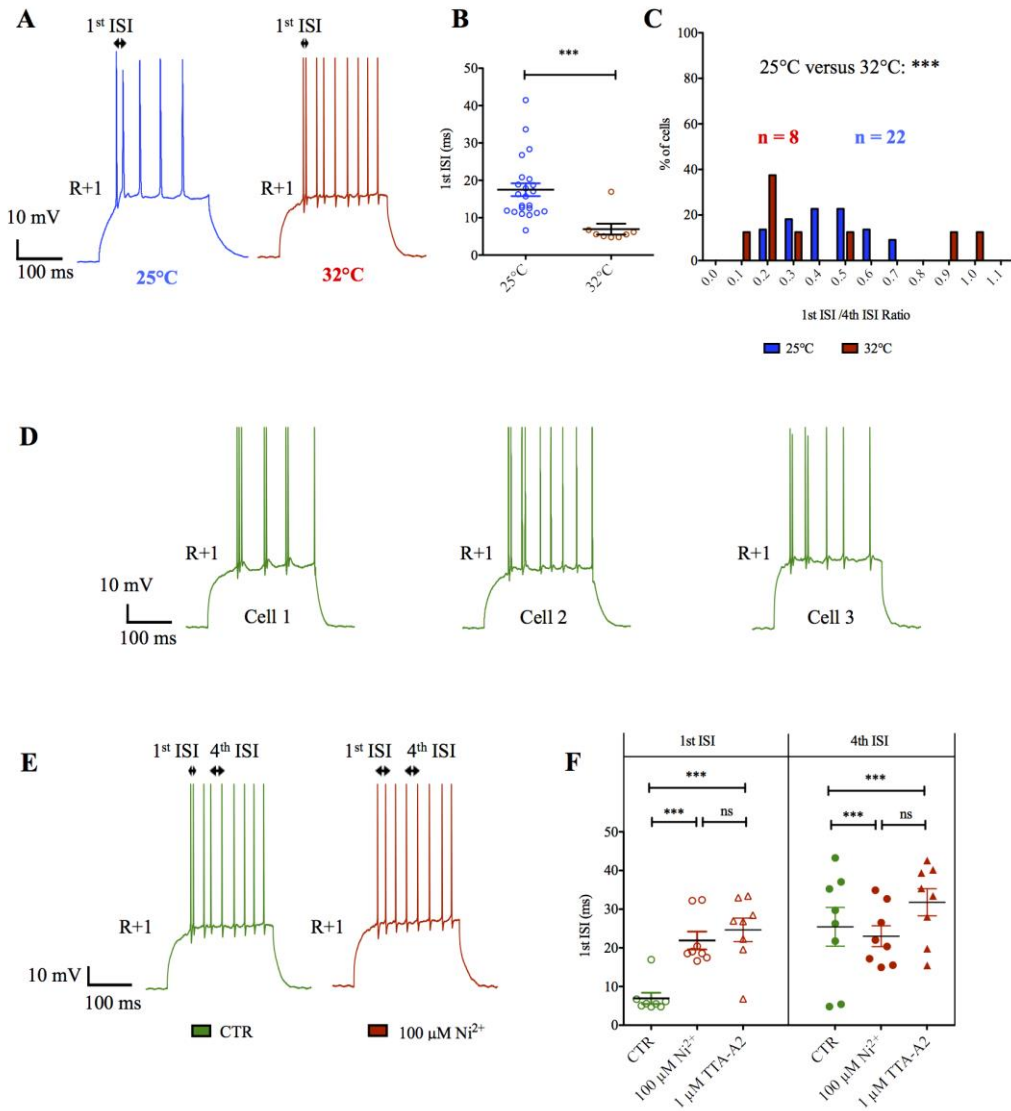


Figure 18: mGCs firing phenotype at physiological temperatures. **A:** Traces of mGCs burst firing at 25°C versus 32°C recording temperatures in CTR conditions. Arrows indicate quantification of the 1st ISI. **B:** Comparison of 1st ISI averages between mGCs recorded at 25°C and at 32°C in CTR conditions. Asterisks indicate the result of Mann-Whitney U-test. *** P < 0.001. Error bars indicate s.e.m. **C:** Frequency distribution plot of 1st ISI/4th ISI ratio measured for individual cells recorded at 25°C or 32°C in CTR conditions. Asterisks indicate the results of χ^2 test comparison of ISIs ratios frequency distribution between 25°C and 32°C groups. *** P < 0.0001. **D:** Illustrative traces of multiple bursts elicited by different cells recorded at 32°C in CTR conditions. **E:** Traces representing the effect of T-type channels block by 100 μM Ni^{2+} on mGCs firing recorded at 32°C. Green: CTR conditions, red: 100 μM Ni^{2+} . Arrows indicate 1st and 4th ISIs measured for quantification. **F:** Effect of T-type channels blockade by 100 μM Ni^{2+} and 1 μM TTA-A2 on 1st and 4th ISI. Green points represent values from cells recorded in CTR conditions. Asterisks and “ns” represent the results of Mann-Whitney U-test or unpaired T-test comparison between CTR and each drug-treated condition for 1st and 4th ISI quantification, depending on the normality of the data sets. *** P < 0.001. Error bars represent s.e.m.

3.1.10. $\text{Ca}_v3.2$ is the main determinant of mGCs burst firing

To genetically confirm the involvement of T-type channels in mGCs burst firing over other voltage-gated channels, avoiding any side effects of the pharmacology, but also to address

which subtype of T-type channels, Ca_v3.1, Ca_v3.2 or Ca_v3.3 is responsible for this mechanism, I compared the firing phenotype of mGCs between wild-type (WT) C57BL/6J mice and Ca_v3.2 KO mice lacking the gene coding for the Ca_v3.2 α 1 subunit (Chen et al., 2003). All experiments with mice slices were done at a recording temperature of 32°C.

mGCs from WT mice showed similar firing phenotype as in rats with very high-frequency bursts of APs accompanied with lower-frequency, tonic single spikes (Figure 19A; and 22B, WT CTR 1st ISI average: 8.369 ± 1.048 ms; n = 20 versus WT CTR 4th ISI average: 34.66 ± 3.608 ms; n = 20; P < 0.0001; Wilcoxon ranked sign test). In WT mice, 100 μ M Ni²⁺ similarly blocked burst firing similarly as in rats, as quantified with the effect on the 1st ISI (Figure 20C, WT CTR 1st ISI average: 8.369 ± 1.048 ms; n = 20 versus WT 100 μ M Ni²⁺ 1st ISI average: 28.10 ± 1.950 ms; n = 18; P < 0.0001; Mann-Whitney U-test). These results already indicate that T-type-mediated burst firing of dentate gyrus mGCs is a phenomenon conserved across these rat and mouse strains and suggest a high degree of preservation of this mechanism across species, with possible implications for human physiology. In contrast, mGCs from Ca_v3.2 KO mice mainly exhibited a more tonic pattern of APs at lower frequency (Figure 19D and 19E, Ca_v3.2 KO CTR 1st ISI average: 19.18 ± 1.995 ms; n = 21 versus Ca_v3.2 KO CTR 4th ISI average: 24.55 ± 1.937 ms; n = 21; P < 0,0001; Paired T-test). Note the striking similarity between mGCs firing from WT in presence of 100 μ M Ni²⁺ and mGCs from KO animals (Figure 19A and 19D). The direct comparison between WT and Ca_v3.2 KO 1st ISI further highlight the impairment of burst firing of mGCs in the absence of Ca_v3.2 (Figure 19F, WT CTR 1st ISI average: 8.369 ± 1.048 ms; n = 20 versus Ca_v3.2 KO CTR 1st ISI average: 19.18 ± 1.995 ms; n = 21; P = 0.0005; Mann-Whitney U-test). In Figure 19G is presented the 1st ISI/4th ISI ratio used previously to quantitatively compare the firing behavior of mGCs at a population level. This figure further evidence the difference between WT and Ca_v3.2 KO mGCs firing phenotype and the similarity between the impact of pharmacological blockade and the genetic ablation of the Ca_v3.2 gene. This major effect of Ca_v3.2 deletion on mGCs burst firing correlates well with the predominant expression of this subtype in the dentate gyrus (Talley et al., 1999; McKay et al., 2006; Francois, 2013; Aguado et al., 2016; Bernal Sierra et al., 2017). Apart from the impairment in burst firing, the overall excitability of mGCs in Ca_v3.2 KO animals was similar as in WT, as quantified with the number of spikes produced by cells in response to increasing current injection intensities, the current injected to reach rheobase and the APs threshold (Figure 20). As for experiments in rats, the trend for the 2nd AP threshold to be higher in WT group than in Ca_v3.2 KO reflects the impact of burst firing.

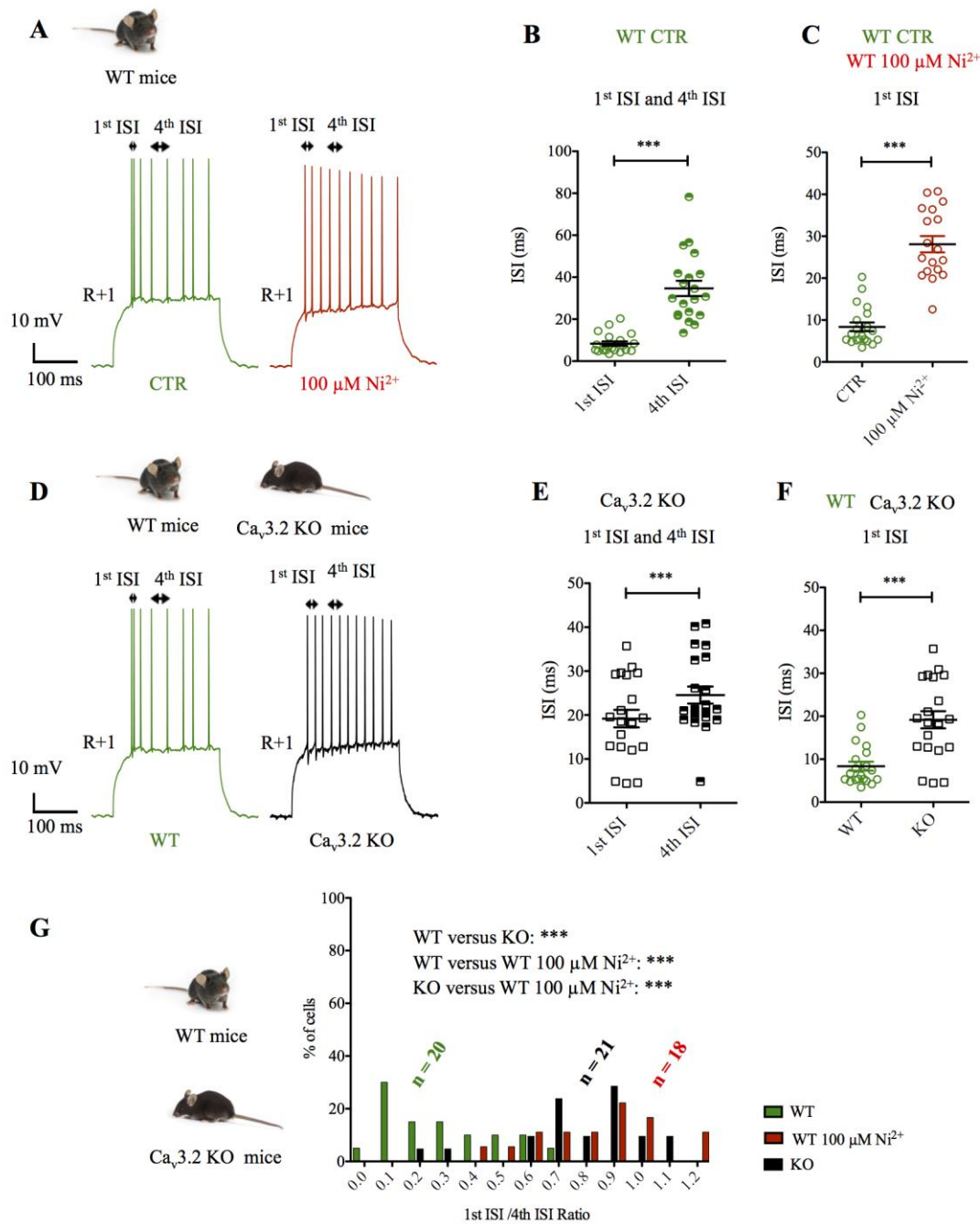


Figure 19: Dominant impairment of mGCs burst firing in Ca_v3.2 KO mice. **A:** Traces of mGCs firing phenotype in WT mice in CTR conditions and upon blockade of T-type channels with 100 μM Ni²⁺. Arrows indicate the 1st and 4th ISIs used for quantification. **B:** Comparison between 1st ISI (clear circles) and 4th ISI (half-filled circles) in WT animals in CTR conditions. Asterisks indicate the result of Wilcoxon signed rank test. *** P-value < 0,001. Error bars represent s.e.m. **C:** Effect of 100 μM Ni²⁺ on WT mGCs firing 1st ISI. Asterisks indicate the result of Mann-Whitney U-test. *** P < 0.001. Error bars represent s.e.m. **D:** Comparative traces illustrating the dominant impairment of mGCs burst firing in Ca_v3.2 KO animals. Arrows indicate the 1st and 4th ISIs used for quantification. **E:** 1st and 4th ISIs quantification from Ca_v3.2 KO mice. Asterisks indicate the result of Wilcoxon signed rank test. *** P < 0.001. Error bars indicate s.e.m. **F:** Direct comparison between WT and Ca_v3.2 KO 1st ISI. Asterisks indicate the result of Mann-Whitney U-test. *** P < 0.001. Error bars indicate s.e.m. **G:** Frequency distribution plot of 1st ISI/4th ISI ratio measured for individual cells recorded from Ca_v3.2 KO mice in CTR conditions and from WT animals in CTR conditions and in the presence of 100 μM Ni²⁺. Asterisks indicate the results of χ^2 test comparison of ISIs ratios frequency distribution between each pair of groups. *** P < 0.0001.

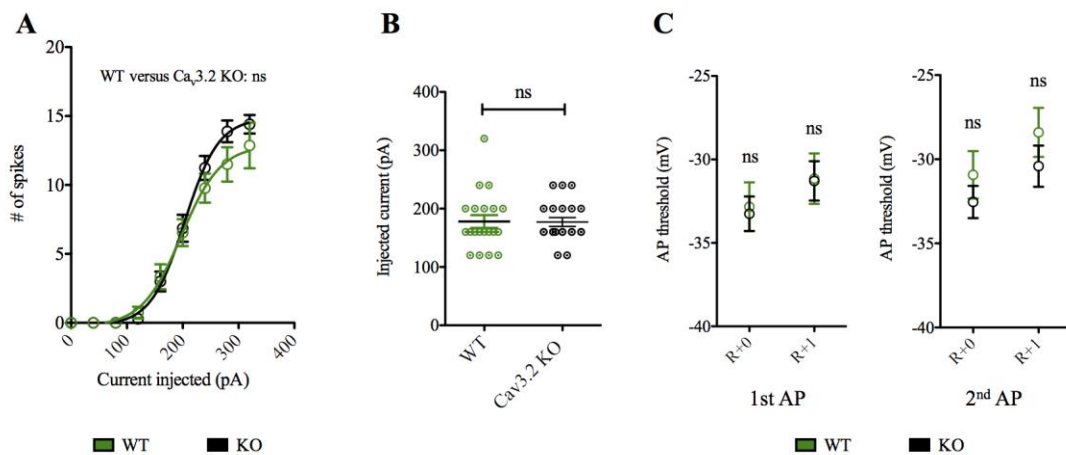


Figure 20: Similar overall excitability of mGCs from WT and Ca_v3.2 KO mice. **A:** Number of APs produced by mGCs in response to increasing somatic current injection stimulation. Symbols indicate average values for each stimulation intensity from WT versus Ca_v3.2 KO mGCs in CTR condition. Curves represent Boltzmann sigmoid fits of both datasets. “Ns” indicate the result of the comparison of Boltzmann fits with hypothesis “different curve for each data set”. Error bars indicate s.e.m. **B:** Minimal injected current required to reach R+0 for WT versus Ca_v3.2 KO mGCs in CTR condition. “ns” indicate the result of unpaired T-test. Error bars indicate s.e.m. **C:** Comparison of 1st and 2nd AP threshold for WT versus Ca_v3.2 KO mGCs in CTR condition, at R+0 and R+1. “ns” indicate the result of Mann-Whitney U-test. Error bars indicate s.e.m.

A small proportion of mGCs were still able to produce burst firing at frequencies higher than 100 Hz (Figure 21A) as illustrated by the 1st ISI values <10 ms in figure 19E (fraction of 1st ISI <10 ms: 3/21) and the percentage of 1st ISI/4th ISI ratio <0.5 in figure 19G (~10%). Interestingly, this proportion of bursting mGCs was not changed in 100 μM Ni²⁺ condition (Figure 21B; % of 1st ISI <10 ms: 8/21; P = 0.1589; Fisher’s exact test) and Ni²⁺ had no effect on the average 1st ISI (Figure 21B, Ca_v3.2 KO CTR 1st ISI average: 19.18 ± 1.995; n = 21 versus Ca_v3.2 KO 100 μM Ni²⁺ 1st ISI average: 15.78 ± 1.844; n = 21; P = 0.209; Mann-Whitney U-test). This differential effect of Ni²⁺ on WT and Ca_v3.2 KO mGCs firing confirms the impairment caused by the lack of Ca_v3.2 channels. The persistence of burst firing in a small proportion of mGCs in KO animals is difficult to interpret but could possibly reflect compensatory mechanism such as up-regulation of other Ca_v3 isoforms. Correlating with this hypothesis, Ca_v3.1 is much less sensitive to Ni²⁺ than Ca_v3.2 channels and its compensatory implication in KO mice mGCs persistent burst firing would explain the lack of effect of 100 μM Ni²⁺ (Zamponi et al., 1996; Lee et al., 1999; Kang et al., 2006). Why such compensatory mechanism occurs only in a small fraction of mGCs is more elusive but could reflect a strong involvement of these cells in recent cognitive processes and a dire need to produce high-frequency burst firing.

All together these results genetically confirm the control of mGCs burst firing by T-type channels and further indicate that the principal responsible of this mechanism is the $Ca_v3.2$ subtype.

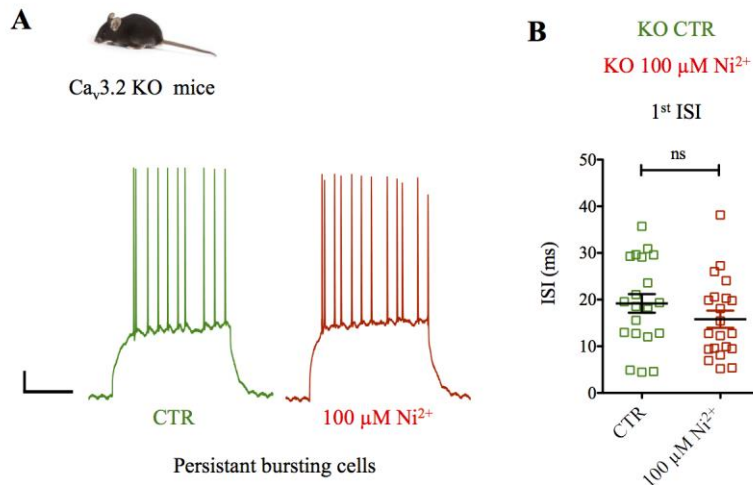


Figure 21: Persistent burst firing in a small proportion of $Ca_v3.2$ KO mGCs. **A:** Illustrating traces of mGCs still able to produce burst firing in $Ca_v3.2$ KO mice, both in CTR conditions and in presence of 100 μ M Ni^{2+} . **B:** Effect of 100 μ M Ni^{2+} on average 1st ISI from $Ca_v3.2$ KO mGCs. “ns” indicate the result of Mann-Whitney U-test. Error bars indicate s.e.m.

3.1.11. mGCs high-frequency burst firing occurs during physiological synaptically-driven activity and is impaired in $Ca_v3.2$ KO mice

To further explore the impact of T-type channels on mGCs firing phenotype in physiological conditions, I performed another set of experiments consisting this time in stimulating the cells not by using direct somatic current injection but through the “normal” synaptic pathway. For this purpose, I performed patch clamp of mGCs from WT and $Ca_v3.2$ KO mice and positioned a stimulating electrode in the molecular layer, ~100 μ m away from the cell body to activate the medial perforant path (MPP) formed by the axon fascicles of cells from the medial entorhinal cortex and projecting onto mGCs dendrites (Figure 22A). I stimulated the MPP with various intensities from 100 μ A down to 10 μ A to elicit firing of mGCs as well as subthreshold EPSPs (Figure 22A and 22B). I could observe that WT mGCs robustly elicited duplets of APs (or less often 3 APs) at very high frequency (~100-200 Hz) from my starting intensity of 100 μ A down to stimulations of 60 μ A (Figure 22B and 25C). For lesser suprathreshold intensities (60-40 μ A), mGCs mostly produced a single AP (Figure 22B and 22C). In contrary, $Ca_v3.2$ KO mGCs were mostly stuck to producing only a single AP, even for the upper set of stimulation intensities (Figure 22B and 22C). The direct comparison of the profile of firing response to stimulation between WT and $Ca_v3.2$ KO mGCs evidences this

different phenotype at a population level (Figure 22C, WT $n = 17$; $Ca_v3.2$ KO $n = 24$; Comparison of Boltzmann Sigmoid fits: null hypothesis: one curve for all data sets; alternative hypothesis: different curve for each data set; $P < 0.0001$; conclusion with 95% confidence: do not reject null hypothesis). As in experiments with somatic current injection stimulation, the basal excitability of the cells, measured as the ability of the cells to fire APs in response to the various stimulation intensities used was similar in WT and $Ca_v3.2$ KO mice (Figure 22D, Probability of firing with respect to MPP stimulation intensity; WT versus $Ca_v3.2$ KO; $P = 0.182$; 2-way ANOVA; strain effect; $P = 0.7475$; 2-way ANOVA; interaction effect). In addition, the slopes of the EPSPs elicited by MPP stimulation were similar in both strains, indicating similar functional synaptic transmission machinery between WT and $Ca_v3.2$ KO (Figure 22E, EPSP slope with respect to MPP stimulation intensity; WT versus $Ca_v3.2$ KO; $P = 0.916$; 2-way ANOVA; strain effect; $P = 0.6109$; 2-way ANOVA; interaction effect). To further characterize the impairment of burst firing, I quantified for each cell the probability of firing at least 1 AP or a burst of 2 APs and more with respect to slope of the EPSPs. From these values, I calculated the half maximal effective EPSP slope ($E50_{slope}$) required to elicit 1 AP or a burst of 2 APs and more. Correlating with Figure 22D, there was no significant difference between the average $E50_{slope}$ for at least 1 AP between WT and $Ca_v3.2$ KO mGCs (Figure 22F left, WT $E50_{slope}$ average: 8.586 ± 0.623 mV/ms; $n = 17$ versus $Ca_v3.2$ KO $E50_{slope}$ average: 9.475 ± 0.516 ; $n = 24$. $P = 0.277$; Unpaired T-test). Oppositely, the average $E50_{slope}$ for a burst of 2 APs or more was significantly higher in the $Ca_v3.2$ KO, indicating that stronger EPSPs are required to elicit high-frequency bursts of APs in $Ca_v3.2$ KO mGCs and confirming the specific impairment of this mechanism (Figure 22F right, WT $E50_{slope}$ average: 12.05 ± 1.227 mV/ms; $n = 14$ versus $Ca_v3.2$ KO $E50_{slope}$ average: 18.58 ± 1.334 mV/ms; $n = 11$; $P = 0.0016$; unpaired T-test).

All together, these results demonstrate that high-frequency bursting is a mode of firing elicited by mGCs in response to activation of the physiological pathway of synaptic input integration – axonal production of APs, and is thus not an aberrant behavior caused by direct somatic current injection. In addition, they confirm the impairment of this mechanism in $Ca_v3.2$ KO animals.

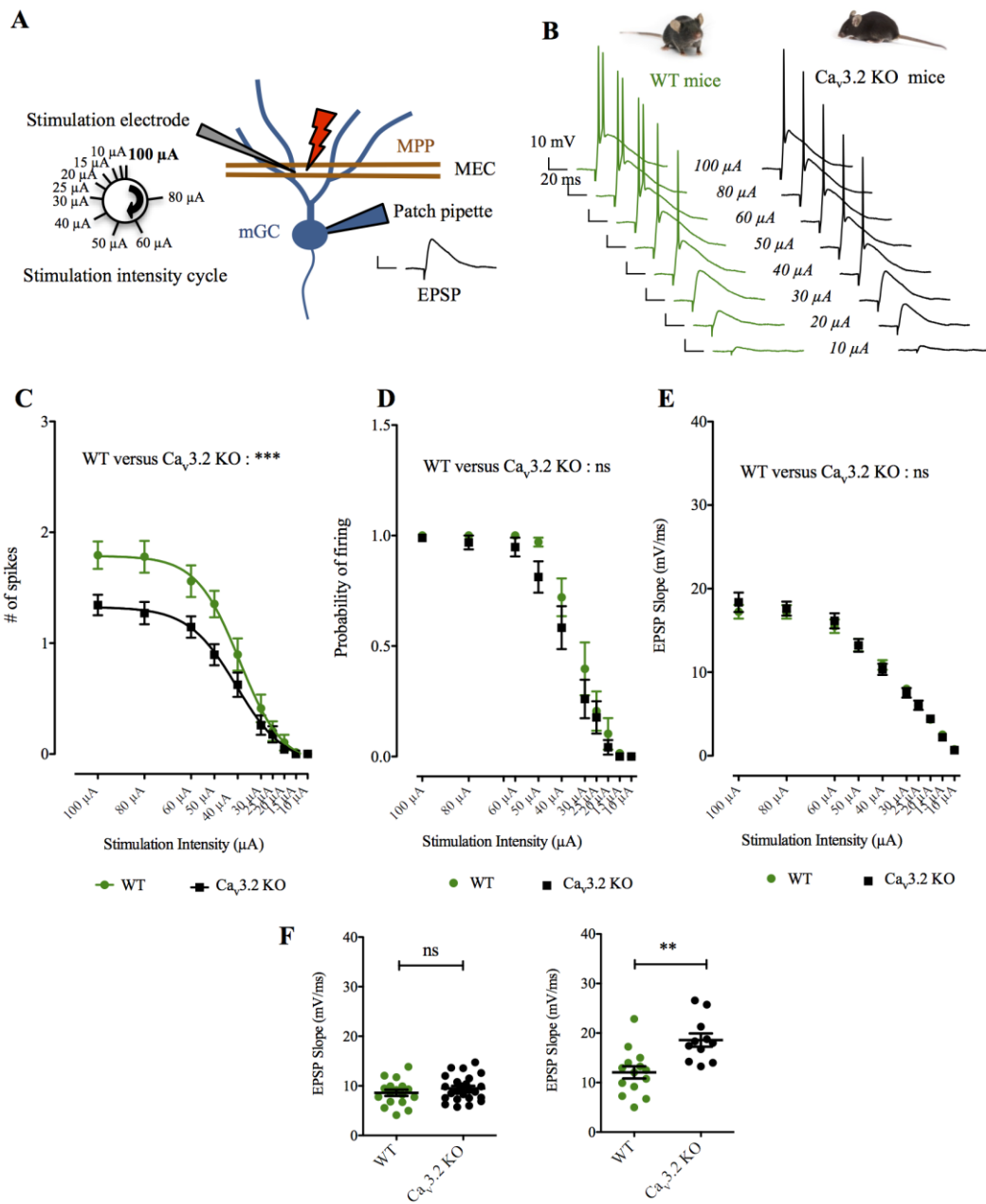


Figure 22: Response of WT and $Ca_v3.2$ KO mice mGCs to medial perforant path stimulation. **A:** Illustrative scheme of the experimental design. mGCs were recorded with the classical patch-clamp technique and the medial perforant path (MPP) was stimulated with a stimulation electrode placed within the molecular layer, $\sim 100 \mu\text{m}$ away from the cell body, at decreasing intensities from $100 \mu\text{A}$ to $10 \mu\text{A}$. Subthreshold and suprathreshold EPSPs were measured and quantified, as well as the number of APs triggered by suprathreshold EPSPs. **B:** Representative traces of the stereotypical response of WT and $Ca_v3.2$ KO mGCs to different stimulation intensities. Note that most of the stimulus artifacts are partly cropped out of the traces and thus do not reflect the strength of the stimulation. **C:** Number of APs produced by mGCs from WT and $Ca_v3.2$ KO in response to variable stimulation intensity. The profile of response of both groups was fit with a Boltzmann sigmoid curve. Asterisks indicate the result of the comparison of Boltzmann fits with hypothesis “different curve for each data set”. *** $P < 0.001$. Error bars indicate s.e.m. **D:** Probability of firing of mGCs from WT and $Ca_v3.2$ KO in response to variable stimulation intensity. “ns” indicate the result of the test of an effect of the strain from a 2-way ANOVA. Error bars indicate s.e.m. **E:** Quantification of the slopes of the EPSPs measured from WT and $Ca_v3.2$ KO in response to variable stimulation intensity. “ns” indicate the result of the test of an effect of the strain and interaction from a 2-way ANOVA. Error bars indicate s.e.m. **F:** Half maximal effective EPSP slope producing firing in general (1 AP or more, left) or firing of a burst of APs (2 APs and more, right).

Asterisks and “ns” indicate the results to unpaired T-test comparison between WT and Ca_v3.2 KO groups for each figure. Error bars indicate s.e.m.

3.2. Behavioral and *in vivo* experiments

Behavioral and *in vivo* recordings study were the result of a collaborative work. Headstages design and fabrication, fabrication of tetrodes, animals' surgery and implantation were performed with the help of Dr. Oleg Senkov (Deutsche Zentrum für Neurodegenerative Erkrankungen, DZNE, Magdeburg, Germany) and Dr. Andrey Mironov (Nizhny Novgorod State University, Nizhny Novgorod, Russia). Contextual fear conditioning experiments and *in vivo* recordings of DG and CA3 neuronal activity were carried out by myself under the guidance of Dr. Oleg Senkov. Analysis of local field potential, multiunit and single unit activity was achieved with the help of Dr. Arthur Bikbaev (Leibniz Institut für Neurobiologie, LIN, research group Molecular Physiology, Magdeburg, Germany).

3.2.1. Analysis of hippocampal network oscillations and neuronal firing *in vivo*

To analyze the effects of Ca_v3.2 gene deletion on the neuronal firing and the connectivity between the DG and CA3 area *in vivo*, I performed recordings of local field potentials and multiunit activity in WT (n = 7) and Ca_v3.2 KO (n = 5) mice. Each animal underwent the implantation of up to 8 tetrodes, with 2 tetrodes in the DG and CA3 area in both left and right hemispheres. Given that *in vitro* recordings were performed in the right hemisphere, *in vivo* analysis was carried out exclusively for the activity recorded on the right side.

Earlier, hippocampal network oscillations in theta (θ : 5 - 12 Hz) and gamma (γ : 30 - 100 Hz) frequency ranges have been shown to be associated with various cognitive processes and reflect the network interaction of neurons forming functional ensembles (reviewed in (Buzsáki, 2002; Csicsvari et al., 2003; Buzsáki and Draguhn, 2004; Colgin and Moser, 2010). Therefore, we quantified the mean spectral power of theta and gamma oscillations in freely moving WT and Ca_v3.2 KO mice. As expected, we observed theta and gamma oscillatory activity in mice of both strains (Figure 23A and 23B). The quantification revealed no significant difference in the mean theta power in the DG between these strains (Figure 23C WT: $0.40 \pm 0.02 \times 10^{-3} \text{ mV}^2$, KO: $0.45 \pm 0.04 \times 10^{-3} \text{ mV}^2$; P = 0.16 ANOVA), although the power distribution by frequencies indicated a slight enhancement of slow theta oscillations in Ca_v3.2 KO mice (Figure 23D). However, the mean theta power in the CA3 area was markedly lower in Ca_v3.2 KO mice ($0.18 \pm 0.02 \times 10^{-3} \text{ mV}^2$) when compared to WT ($0.26 \pm 0.02 \times 10^{-3} \text{ mV}^2$; P

= 0.0016 ANOVA & Bonferroni test), without an indication of suppression of particular frequencies within theta range (Figure 23H).

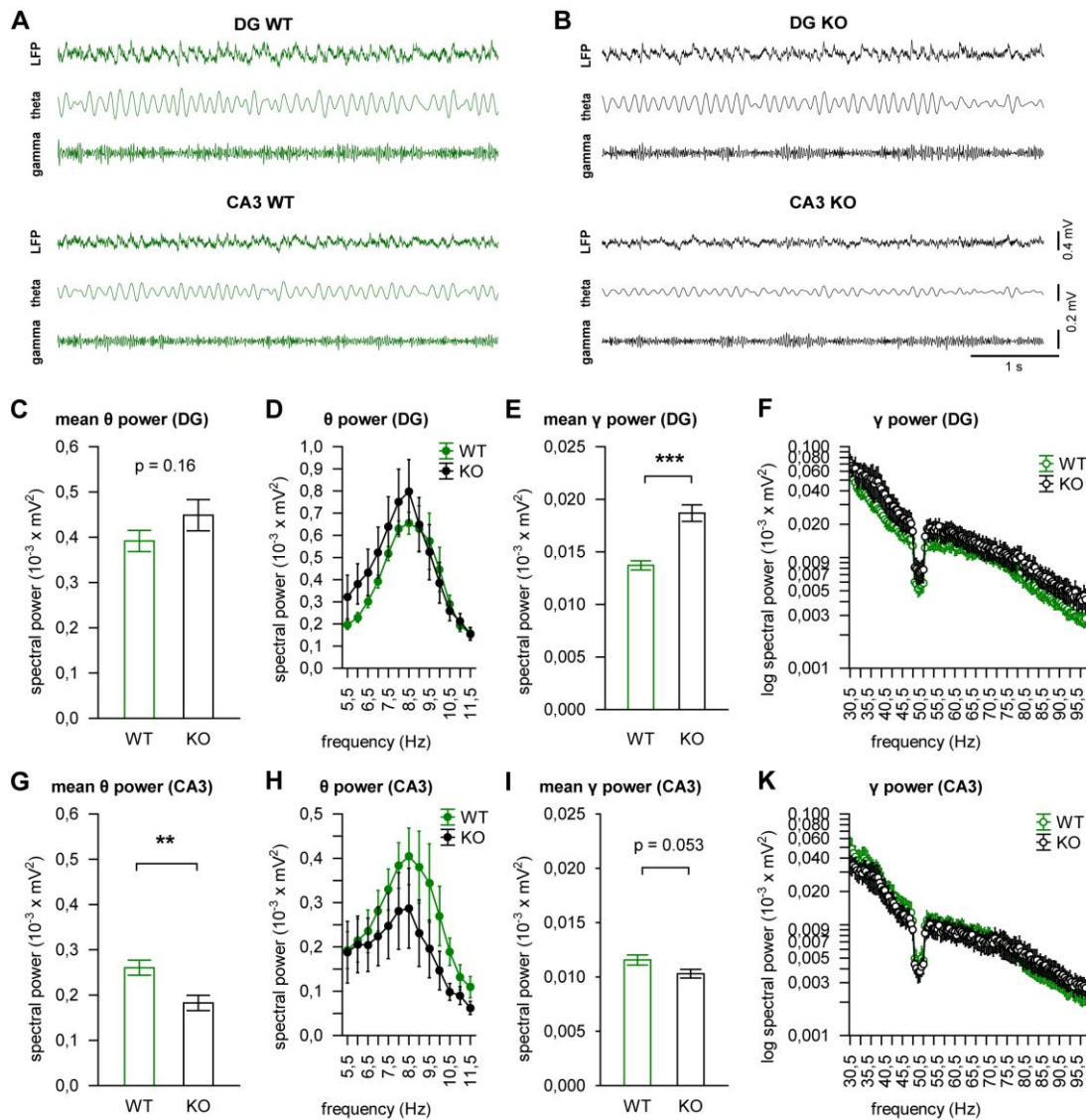


Figure 23: Analysis of hippocampal theta (5 - 12 Hz) and gamma (30 - 100 Hz) network oscillations in the DG and CA3 area of WT and $\text{Ca}_v3.2$ KO mice. **A-B:** Representative traces of local field potential recorded in freely behaving WT (A) and $\text{Ca}_v3.2$ KO (B) mice. **C, G:** Mean power of theta oscillations in the DG (C) and CA3 area (G). **D, H:** Distribution of the spectral power within theta frequency range in the DG (D) and CA3 area (H). **E, I:** Mean power of gamma oscillations in the DG (E) and CA3 area (I). **F, K:** Distribution of the spectral power within theta frequency range in the DG (F) and CA3 area (K). ** $p < 0.01$, *** $p < 0.001$ (protected ANOVA followed by Bonferroni test). Error bars indicate s.e.m. Data was quantified with the help of Dr. Arthur Bikbaev (LIN, Magdeburg, Germany).

In contrast to theta oscillations, we found that the mean gamma power was higher in the DG of $\text{Ca}_v3.2$ KO mice ($0.0186 \pm 0.0008 \times 10^{-3} \text{ mV}^2$) as compared to WT ($0.0137 \pm 0.0004 \times 10^{-3} \text{ mV}^2$; $P < 0.0001$ ANOVA & Bonferroni test) (Figure 23E). Intriguingly, the mean gamma power in CA3 area in KO mice was lower ($0.0103 \pm 0.0004 \times 10^{-3} \text{ mV}^2$) that that in

WT ($0.0116 \pm 0.0005 \times 10^{-3} \text{ mV}^2$), but the difference failed to reach significance ($P = 0.053$ ANOVA) (Figure 23I).

Extra-hippocampal inputs drive the frequency and amplitude (and therefore spectral power) of theta and gamma oscillations in the DG, which, in turn, strongly influences oscillatory activity in CA3 area (Bragin et al., 1995; Montgomery et al., 2008). Together with CA3 area-specific reduction of theta oscillations in $\text{Ca}_v3.2$ KO mice, the finding that the increase in gamma power in the DG is not associated with corresponding enhancement of gamma oscillations in CA3 in mice lacking $\text{Ca}_v3.2$ supported the suggestion of impairment in communication between granule cells in the DG and their downstream targets in CA3 area.

To further evaluate the connectivity between the DG and CA3 in control and KO mice, we calculated the transfer function for theta and gamma oscillations (Figure 24). This approach allowed me to characterize the transfer of oscillatory activity from the DG (taken as 100%) to CA3 area for particular frequencies. We found that in $\text{Ca}_v3.2$ KO mice the ratio of spectral power of theta and gamma oscillatory bands in CA3 to corresponding values in the DG (theta $42.1 \pm 1.8\%$; gamma $60.0 \pm 0.6\%$) was dramatically lower mice as compared with wild type animals (theta $71.4 \pm 2.7\%$; gamma $79.0 \pm 0.8\%$; both $P < 0.0001$ ANOVA & Bonferroni test) (Figure 24A and 24C). Remarkably, analysis of oscillations' transfer by frequencies revealed rather uniform loss of spectral power across the theta range in $\text{Ca}_v3.2$ KO (Figure 24B), whereas the decrease in the gamma oscillations' transfer was particularly prominent in low gamma (30 - 60 Hz) oscillatory band.

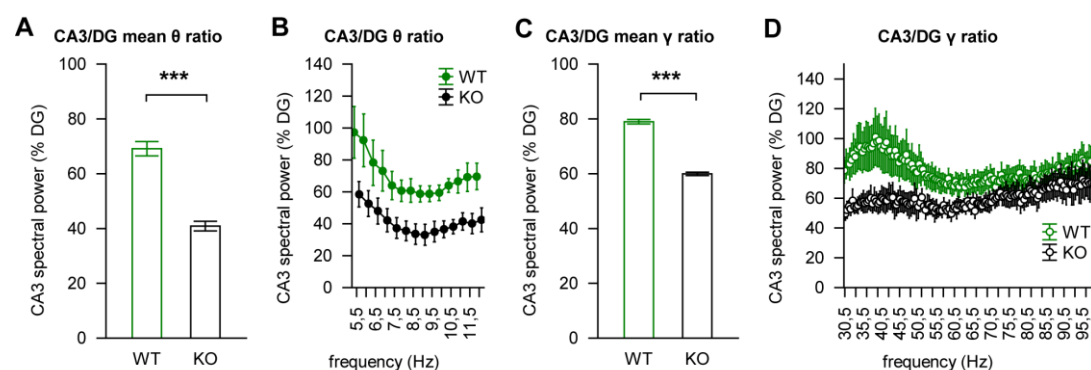


Figure 24: The ratio of spectral power of theta and gamma oscillations in CA3 and the DG. **A:** Mean theta spectral power in CA3 in relation to theta spectral power in the DG (taken as 100%). **B:** The impairment of theta transfer from the DG to CA3 area is uniform for theta frequency range. **C:** Mean ratio of spectral power of gamma oscillations in the CA3 to that in the DG (taken as 100%). **D:** The impairment of gamma oscillations' transfer in $\text{Ca}_v3.2$ KO mice is particularly prominent for low gamma band (30-60 Hz). *** $P < 0.001$ (protected ANOVA followed by Bonferroni test). Error bars indicate s.e.m. Data was quantified with the help of Dr. Arthur Bikbaev (LIN, Magdeburg, Germany).

The aforementioned results of *in vitro* analysis demonstrated that blockade or genetic deletion of $\text{Ca}_v3.2$ strongly affects the bursting of mGCs. To address the question whether absence of $\text{Ca}_v3.2$ is associated with comparable effect *in vivo*, we evaluated the rate and the

temporal features of principal cells' firing in WT and Ca_v3.2 KO mice. We found that genetic deletion of Ca_v3.2 led to significant reduction of the spontaneous firing rate of excitatory units both in the DG (Figure 25A; 1.89 ± 0.52 Hz, $p = 0.0258$ Mann-Whitney U-test) and CA3 (Figure 25B; 1.69 ± 0.28 Hz, $P = 0.0022$ Mann-Whitney U-test), as compared to respective values in control animals (DG: 2.94 ± 0.42 Hz; CA3: 3.36 ± 0.43 Hz). Importantly, the mean inter-burst interval in Ca_v3.2 KO mice was markedly longer (Figure 25C; 16.97 ± 5.19 s; $P = 0.0334$ Mann-Whitney U-test) than that in WT mice (6.12 ± 1.25 s). This supported the results obtained *in vitro* reflecting a significantly lower frequency of occurrence of spontaneous bursts in the DG of mice lacking Ca_v3.2. Although occurring at lower rate, the bursts in the DG of Ca_v3.2 KO mice showed similar pattern to those recorded in WT animals, reflected by the similar number of spikes per burst (Figure 25D; WT: 3.76 ± 0.22 , KO: 3.54 ± 0.45 ; $P = 0.11$ Mann-Whitney U-test) and the duration of consecutive ISIs from 1 to 4 (Figure 25E; 1st ISI: WT: 4.02 ± 0.16 ms, KO: 3.95 ± 0.20 ms; $P = 0.77$; 2nd ISI: WT: 11.93 ± 0.60 ms, KO: 13.00 ± 0.84 ms; $P = 0.39$; 3rd ISI: WT: 9.54 ± 0.52 ms, KO: 11.69 ± 1.24 ms; $P = 0.19$; 4th ISI: WT: 10.87 ± 1.00 ms, KO: 11.85 ± 1.89 ms; $P = 0.70$ Mann-Whitney U-test for all).

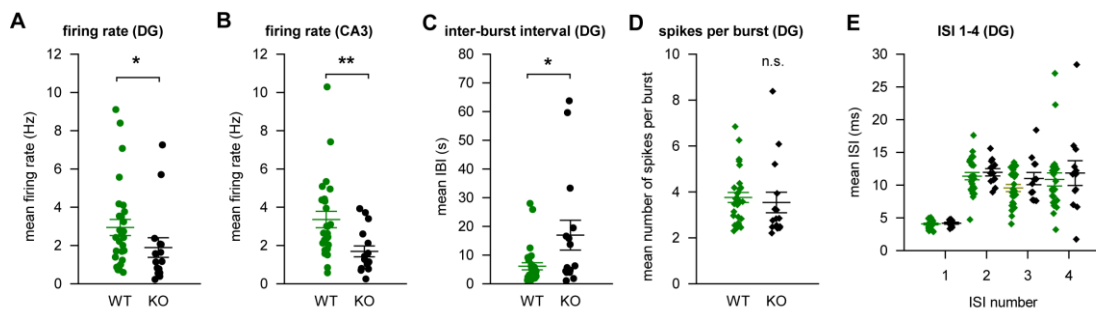


Figure 25: Spontaneous firing and bursting rate for excitatory single units is decreased in freely behaving Ca_v3.2 KO mice ($n = 15$ units) in comparison with WT animals ($n = 28$ units). **A-B:** Mean firing rate in the DG (A) and CA3 (B) is markedly lower in Ca_v3.2 KO mice. **C:** The mean inter-burst interval for excitatory neurons is markedly reduced in Ca_v3.2 KO mice. **D-E:** Freely moving WT and Ca_v3.2 KO mice have similar average number of spikes per burst and the structure of burst. * $P < 0.05$, ** $P < 0.01$, n.s. non-significant (Mann-Whitney U-test). Error bars indicate s.e.m. Data was quantified with the help of Dr. Arthur Bikbaev (LIN, Magdeburg, Germany).

Thus, results of *in vivo* electrophysiological analysis provided additional evidence of impairment of bursting in the DG of Ca_v3.2 KO mice. Furthermore, evaluation of strain-specific differences in theta and gamma oscillations strongly supported the suggestion of Ca_v3.2 genetic deletion-induced impairment of information transfer from the granule cells in the DG to their targets in CA3 area.

3.2.2. Ca_v3.2 KO mice show behavioral deficits in contextual fear conditioning

To obtain behavioral phenotypes of WT and Ca_v3.2 KO mice that I could parallel with mGCs firing, I tested the response of WT and Ca_v3.2 KO mice to a task of contextual fear conditioning known to be dentate gyrus-dependent (Johnston et al., 2008; Madroñal et al., 2016; Bernier et al., 2017). Mice implanted with the *in vivo* recording apparatus (Figure 26A) were placed in a modular conditioning chamber configured in a neutral context (CC-: plain grey walls, plastic floor, odor A; see material and methods) and a negative context (CC+: black and white squared walls, metal shock-delivering grid floor, odor B; see material and methods) (Figure 26B). The conditioning protocol was classical and divided in two days, with a training phase and a test phase (Figure 26C). During training day, mice were exposed subsequently to CC+ and CC- and exposure to CC+ was paired with foot shock conditioning. One day later, animals were first exposed to CC+ and then CC-.

Figure 26D present the results of the quantification of WT and Ca_v3.2 KO mice freezing expressed as percentage of total session time (WT n = 7; Ca_v3.2 KO n = 5). The first outcome of these experiments is that Ca_v3.2 KO animals exhibited more freezing than WT in every session and for both training and test days (black lines and black '*' symbols). Both WT and KO animals were affected by the electrical shock, as reflected by the increased freezing in training CC+ as compared to training CC- (brown '#' symbols). Similarly, animals from both strains were able to recall the trauma of the foot shock by contextual cues as evidenced by the increased freezing in test day as compared to training day (red '!' symbols). Finally, the most interesting result was that WT animals froze significantly more when exposed to the CC+ as compared to CC- during the training day (blue lines and blue '\$' symbol, P = 0,0207; Mann-Whitney U-test) whereas Ca_v3.2 KO did not (blue lines and blue "ns", P = 0,0952; Mann-Whitney U-test). While the limited number of animals tested in this experiment doesn't allow a strong statement, this data nevertheless suggest an impairment of Ca_v3.2 KO mice performance in discriminating the neutral and negatively reinforced context. The behavioral phenotype of Ca_v3.2 KO characterized in my experiments correlates well with the established behavioral reports on these animals in the literature which evidenced their increased anxiety (Gangarossa et al., 2014); their normal acquisition of fear response in foot-shock conditioning paradigms (Chen et al., 2012a) and their deficits in context-related cognition (Chen et al., 2012a). However, the context-unspecific freezing of Ca_v3.2 KO could also reflect a generalization of the fear response of these animals rather than improper discrimination of CC+ and CC- contexts.

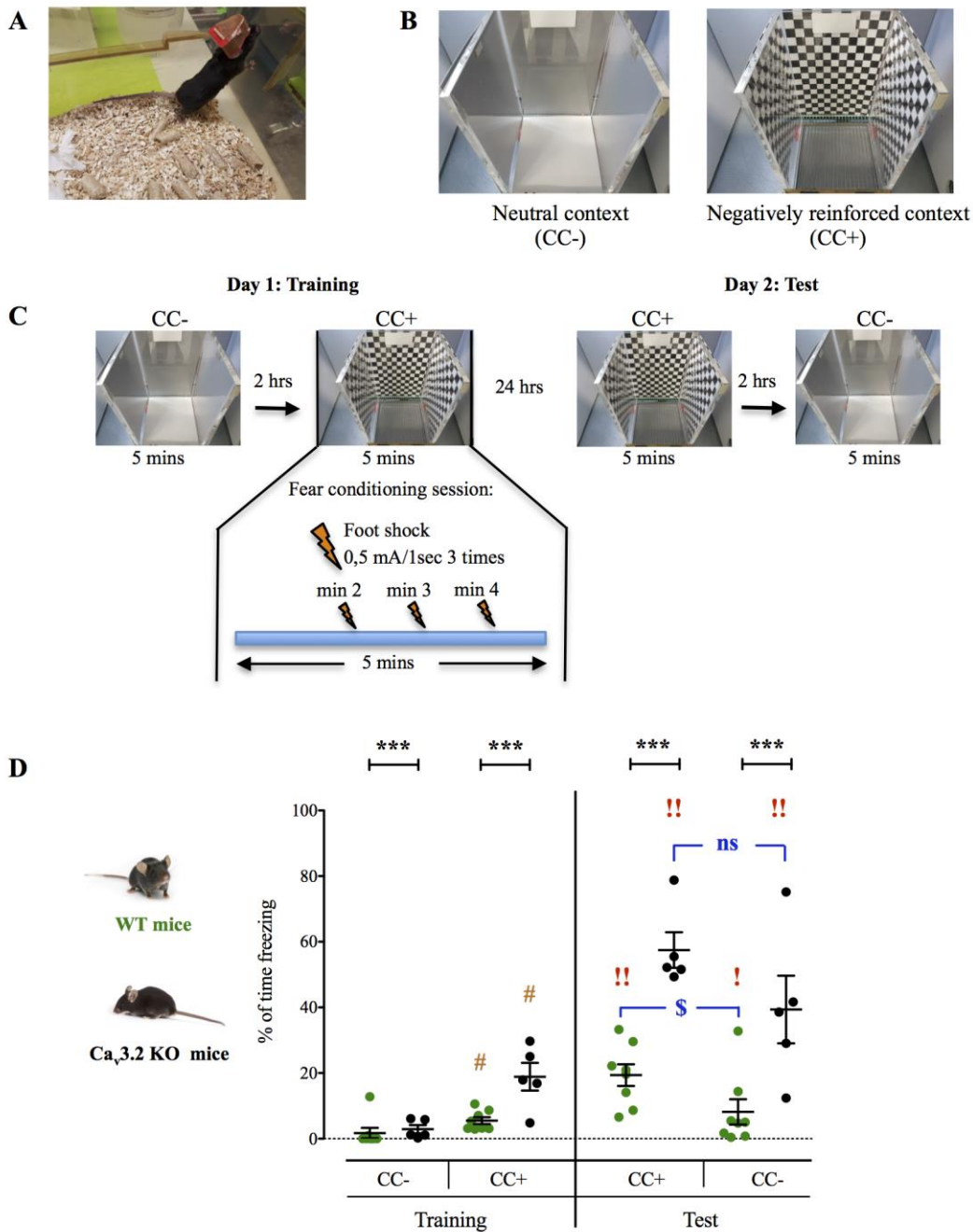


Figure 26: Performance of implanted WT and Ca_v3.2 KO in a task of contextual fear conditioning. **A:** Illustrative picture of a mouse carrying the *in vivo* recording apparatus. **B:** Pictures of the modular conditioning chamber used in the experiments, in neutral context configuration (left, CC-) and in negatively reinforced context configuration (right, CC+). **C:** Time schedule and design of the contextual fear-conditioning paradigm. **D:** Freezing response of WT (green full circles) and Ca_v3.2 KO (black full circles) during the course of the experiment, quantified as percentage of total session time (5 minutes). All tests used for analysis were Mann-Whitney U-tests. Different symbols illustrate the results of Mann-Whitney U-tests to multiple comparisons among groups. Black ‘*’ symbols represent the comparison WT versus KO, for each session. Light brown ‘#’ symbols represent the comparison between training day CC+ and training day CC- within strains and characterizes the immediate response to foot shock. Red ‘!’ symbols represent the comparison between test day and training day, for both contexts and both strains and characterizes the memorization of the trauma. Blue ‘\$’ symbol and blue “ns” represent the comparison between test day CC+ and test day CC- for each strain and characterizes the context-dependency of the response. Error bars indicate s.e.m.

Taken together, the outcomes of behavioral experiments provided me a phenotype base of Ca_v3.2 KO versus WT mice to interpret the *in vivo* recordings, and demonstrated that genetic deletion of Ca_v3.2 impaired performance of freely behaving animals in the DG-dependent cognitive task.

4. Discussion

4.1. mGCs burst firing

In this study, I characterized a burst firing phenotype of mGCs. Burst firing of mGCs is not an extensively studied phenomenon and tends to be associated with pathological plasticity of the dentate gyrus such as in models of epilepsy (Buckmaster and Dudek, 1997; Scharfman, 2011; Shao and Dudek, 2011; Dengler and Coulter, 2016; Kelly and Beck, 2017). However, it has also been documented *in vitro* in non-pathological conditions (Scharfman et al., 2003, 2007). More importantly, it was recently shown that mGCs *in vivo* fire preferentially in the form of very high-frequency bursts of several APs when they become active (Pernía-Andrade and Jonas, 2014). In my hands, this burst-firing of mGCs was notably sensitive to the washout of the intracellular content by medium sized patch pipettes (4-6 M Ω) and was strongly enhanced at 32°C (Figure 18), consistent with *in vivo* observations (Pernía-Andrade and Jonas, 2014). With the help of relatively small patch pipettes in the range of 10-30 M Ω , to limit intracellular washout, I was able to consistently observe burst-firing of mGCs, supporting the idea that this represents a physiological firing mode of these cells. In addition, I showed that mGCs burst-firing is supported by an intrinsic excitability mechanism and is not mediated by network interactions.

4.2. mGCs burst firing is controlled by T-type channels in the axon initial segment

T-type channels do not produce obvious low-threshold calcium spike measurable in mGCs without pharmacological isolation, in contrast to those observed in iGCs (Blaxter et al., 1989; Schmidt-Hieber et al., 2004a; Pedroni et al., 2014). Furthermore, pharmacological blockade of T-type channels does not acutely affect the mGCs firing (Schmidt-Hieber et al., 2004a; Martinello et al., 2015). In line with this, I found no effect of T-type blockers and/or of Ca_v3.2 gene deletion on overall excitability of mGCs, as quantified by the average number of spikes produced by cells in response to somatic current injection, the AP thresholds and the rheobase current. However, I showed that blocking T-type channels resulted in a strong change in the firing pattern of the cells, switching them from a high-frequency bursting mode to a tonic mode of APs generation at lower frequencies. Such control of burst firing by T-type channels is consistent with their stereotypical action evidenced in thalamic relay cells and brainstem cartwheel cells (Kim et al., 2001; Zhan et al., 1999; Bender et al., 2012), but for mGCs the bursting behavior has been so far controversial and the underlying mechanisms have not been

explored. I hypothesize that the apparent fragility of mGCs burst-firing in whole-cell patch-clamp recordings, due to the washout effect already mentioned, might be a reason for its under-exploration.

T-type channels are present at the level of the axon initial segment of cartwheel cells (Bender and Trussell, 2009b; Bender et al., 2012) and of dentate gyrus mGCs, as recently reported (Martinello et al., 2015). With the help of 2-photon microscopy, I evidenced T-type channels-mediated calcium fluxes in a region around 15 μm away from the soma at the level of the proximal axon (Figure 13). This location correlates very well with the position of the axon initial segment as it has been determined in mGCs (Schmidt-Hieber and Bischofberger, 2010). Furthermore, we showed that local blockade of T-type channels in this axonal domain resulted in impairment of the bursting phenotype of mGCs (Figure 15 and 17).

4.3. Axon initial segment T-type channels and control of AP threshold

Martinello and colleagues (Martinello et al., 2015) showed T-type channels localized at the level of the axon initial segment in mGCs are involved in a cholinergic-induced plasticity of AP threshold, even though T-type channels pharmacological blockade did not produce any evident acute changes in mGCs firing activity. Rather, the “indirect” effect of T-type channels on AP threshold occurs by downstream inhibition of M-type currents leading to an increase in AP threshold after cholinergic-induced upregulation of T-type channels basal activity at resting potential (*i.e.* a larger window current). In brainstem cartwheel cells, local blockade of axon initial segment T-type channels with high concentrations of mibefradil or Ni^{2+} increased the AP threshold (Bender and Trussell, 2009b). Using comparable concentrations of Ni^{2+} (10 mM) and application of gradually increasing long puffs of Ni^{2+} immediately prior to spike-triggering stimulation, I also observed changes in AP threshold (Figure 14 and 15). This effect was, however, not consistent with the lack of effect on general excitability, including AP threshold, of T-type blockers applied in the bath or the genetic ablation of the $\text{Ca}_v3.2$ channel subtype (Figure 8 and 19). Furthermore, using a protocol consisting in empirically adjusting the length of the puff and the time interval between the puff and the stimulation, I obtained strong block of burst firing with negligible effect on AP threshold (Figure 16 and 17). My interpretation of these results is that, in agreement with Martinello and others (Schmidt-Hieber et al., 2004b), the primary effect of T-type channels in axon initial segment of mGCs is not to control AP threshold or general excitability but to control burst firing and that the observed influences on AP threshold in my puff experiments might be due to unspecific action of Ni^{2+} on other voltage-gated channels like sodium channels. However, I do not completely rule out a possible dual effect of axon initial segment T-type channels on mGCs firing, namely an initial control of AP

threshold followed by a slower re-adjustment of AP threshold accompanied by an impairment of burst firing.

4.4. Ca_v3.2 has major impact on the burst-firing in mGCs

Most of mGCs recorded in Ca_v3.2 KO mice were strongly impaired in their ability to fire bursts of APs, similar to the effect of T-type blockers on mGCs from Wistar Han rats and WT mice. These results show that Ca_v3.2 is a major component in modulation of mGCs burst-firing and correlate with the predominant expression of this subtype in DGGCs (Talley et al., 1999; McKay et al., 2006; Francois, 2013; Aguado et al., 2016; Bernal Sierra et al., 2017). Nevertheless, burst-firing was observed in a small proportion of Ca_v3.2 KO mGCs. Remarkably, this proportion was not affected by additional application of T-type blockers (Figure 21). In WT mice and Wistar Han rats, there were also some cells that fired high-frequency APs upon application of T-type blockers (see for example the ISIs <10 ms in Figure 6D, 7 and 18F). However, the possibility that persistence of burst-firing was caused by insufficient blockade of Ca_v3.2 due to poor penetration of the blocker in the slice tissue in these cases cannot be ruled out. Another possibility is that Ca_v3.2 might not be the sole determinant of mGCs burst firing and that other T-type channels could also contribute to burst firing in a subset of mGCs. In line with this, Ca_v3.1 is less sensitive to Ni²⁺ and would get little or not affected by the concentration I used (Zamponi et al., 1996; Lee et al., 1999; Kang et al., 2006). Another explanation would be that Ca_v3.2 is not a simple on/off switch of burst firing, but rather an enhancing mechanism that is not required *per se* to produce burst firing but helps to trigger it or to sustain it. The results of the medial perforant path stimulation experiments, in which mGCs from Ca_v3.2 KO mice were impaired in their production of several APs at high frequencies following synaptic stimulation, but could still reach such firing with stronger EPSPs as compared to WT, support this suggestion (Figure 22F).

4.5. T-type mediated burst firing of mGCs impacts on DG-CA3 communication

mGCs should fire APs at high frequencies to be able to trigger their postsynaptic CA3 target cells (Henze et al., 2002). However, mGCs have “adverse” electrophysiological and structural properties that make them apparently lowly excitable and unlikely subject to undergo strong depolarization theoretically required to make them fire at these high frequencies (Mongiat and Schinder, 2011; Krueppel et al., 2011; Drew et al., 2013; Lopez-Rojas and Kreutz, 2016). In this regard, T-type channels might be critical determinants of mGCs function by allowing these cells to produce low-threshold high frequency firing which would be

compatible with both, the low excitability of mGCs and the requirement to fire at high frequency bursts of AP in order to trigger CA3 pyramidal cells. Indeed, T-type channels are low-voltage activated channels and start to open at hyperpolarized potentials close to the resting potential of mGCs (Perez-Reyes, 2003) (Figure 5C), consistent with my findings that bursting robustly appears from stimulations as low as the first one producing firing of the cell (rheobase). In addition, the intra-burst APs frequency was high and reached around 140 Hz in recordings made at 32°C, strikingly similar to the burst of mGCs evidenced in the *in vivo* study of Pernía-Andrade and Jonas (Pernía-Andrade and Jonas, 2014). This range of firing frequency theoretically allows such bursts of APs to robustly trigger CA3 pyramidal cells (Henze et al., 2002) (Figure 4).

In this scenario, activation of Ca_v3.2 seems to represent a mechanism that increases the frequency of the firing output of granule cells, thereby increasing the probability of activation of their postsynaptic targets, i.e., CA3 pyramidal neurons. As a consequence, the contribution of Ca_v3.2 ensures a more reliable transfer of sensory information downstream into hippocampal circuitry. The analysis of *in vivo* recordings in WT and Ca_v3.2 KO mice provided further evidence of the Ca_v3.2 importance in information transfer from the DG to CA3. First, the significant difference in the inter-burst intervals between WT and Ca_v3.2 KO mice demonstrated that genetic deletion resulted in significant reduction of the burst occurrence rate, hence corroborated my results obtained *in vitro* in presence of T-type calcium channel antagonists. Second, we found markedly lower spontaneous firing rate in Ca_v3.2 KO mice both in the DG and CA3 (Figure 25A and 25B), confirming the role of DGGCs firing frequency in activation of CA3 pyramidal cells. The analysis of theta and gamma network oscillations allowed us to address the question of information transfer from the DG to CA3: Ca_v3.2 KO showed a dissociation between the DG and CA3 for both oscillatory bands that indicated an impaired communication between these regions. Theta and gamma power in the DG are strongly influenced by extra-hippocampal sensory inputs, whereas oscillations in the CA3 are to a large degree determined by the mossy fiber input (Bragin et al., 1995; Buzsáki, 2002; Csicsvari et al., 2003). In Ca_v3.2 KO animals, we found that comparable levels of theta power in the DG was accompanied by markedly lower theta power in CA3, while elevated gamma in the DG was not associated with corresponding increase in the gamma power in CA3 (Figure 23). More precise quantification of such oscillatory relationship between the DG and CA3 provided additional evidence of impaired transmission from the DG to CA3. For both theta and gamma frequency ranges, highly significant reduction in the transfer was evident in Ca_v3.2 KO mice, which was particularly prominent for low (30 - 50 Hz) gamma oscillations (Figure 24). Previously, low (30 - 60 Hz) gamma oscillations in the hippocampus were proposed to reflect retrieval of memories, whereas the power of high (60 - 90 Hz) gamma was increased during encoding of new memories (Colgin et al., 2009), upon sensory stimulation (Lu et al., 2011) or

induction of synaptic plasticity (Bikbaev and Manahan-Vaughan, 2017). Thus, the selective impairment of the transfer of low gamma oscillatory band that was evident in Ca_v3.2 KO mice might indicate the contribution of this subtype of T-type calcium channels to oscillatory mechanisms in the DG.

4.6. Contextual foot-shock fear conditioning

In this study, I assessed the behavioral response of WT and Ca_v3.2 KO mice in a task of contextual foot-shock fear conditioning. Since T-type channels are key players in pain perception (Bourinet et al., 2016), concerns have raised that Ca_v3.2 KO differential response to the contextual foot-shock fear conditioning might be at least partially caused by differential sensitivity to the electric shock (delivered to the animals feet through a metallic grid floor). First of all, foot-shock fear conditioning has been successively used with Ca_v3.2 KO mice and KO animals in this study showed normal conditioning and similar learning performance as WT (Chen et al., 2012b). In addition, the main reported effect of Ca_v3.2 KO on pain sensation is an analgesic effect (Bourinet et al., 2016) and Ca_v3.2 KO mice in my experiments showed always a stronger freezing than WT mice (Figure 26D). Moreover, Ca_v3.2 KO reacted to the foot shock by squeaking and jumping in a similar manner as WT mice, suggesting that they felt the pain. Finally, WT and Ca_v3.2 KO mice similarly started to freeze following the first foot shock during conditioning, suggesting similar conditioning in WT and Ca_v3.2 KO as in Chen et al. (Chen et al., 2012b).

In my experiment, we found no significantly preferential freezing in the negative context as compared to neutral context in Ca_v3.2 KO mice following conditioning, whereas WT mice froze significantly more in the negative context (Figure 26D). One explanation of this is that Ca_v3.2 KO mice are unable to discriminate the negative context from the neutral context. This hypothesis would be in line with the model function of DGGCs to mediate pattern separation of sensory information (Deng et al., 2010; Johnston et al., 2016). Context-related cognitive deficits have been suggested by Chen and colleagues in their study of Ca_v3.2 KO mice (Chen et al., 2012b). They compared the performance of WT and Ca_v3.2 KO mice in a context-cued and tone trace-fear foot shock conditioning. They found no differences in freezing percentage between both strains and a normal fear response of Ca_v3.2 KO evoked by the tone, but a deficit on contextual-evoked Ca_v3.2 KO freezing response when animals were put in the conditioning chamber. I, however, observed more freezing of Ca_v3.2 KO than WT, in response to the negatively reinforced context (CC+) after conditioning during the test day, but also in every session of both training and test days (Figure 26D). The apparent discrepancy between my results and those from Chen et al. could be explained by the fact that in their experiments,

Chen and colleagues habituated mice to the conditioning chamber for three days prior to conditioning while I did not habituate my animals. Moreover, they used only one context in their experiment, the conditioning chamber, whereas we used two similar yet different contexts consisting in differential configurations of the modular conditioning chamber (Figure 26B). This could indicate that animals in their experiment got more engaged in a pattern completion process while animals in my experiment got more engaged in a pattern separation mechanism. These mechanisms might be affected in different manner by the deletion of the $Ca_v3.2$ gene and could also explain the discrepancy between my results and theirs.

4.7. Proposed model

Based on my results and existing literature, I propose the model illustrated in figure 27 in which $Ca_v3.2$ channels localized at the level of the axon initial segment of mGCs control, enhance or sustain a stereotypical low-threshold, high-frequency burst-firing phenotype of these cells. This mechanism would then allow mGCs to produce the high frequency firing required to robustly activate their postsynaptic targets, the CA3 pyramidal cells, in response to weak somatic depolarization underlined by their low excitability and strong dendritic voltage attenuation (Drew et al., 2013; Henze et al., 2002; Krueppel et al., 2011; Lopez-Rojas and Kreutz, 2016; Mongiat and Schinder, 2011).

4.1. Perspectives

In this study, I characterized the impact of T-type channels on the pattern of APs production by mGCs. It would be of further interest to precisely delineate the mechanisms that allow T-type channels to control or enhance mGCs burst-firing phenotype. One explanation would be that T-type channels produce a local membrane depolarization at the level of the axon initial segment that can, due to the small size of this axonal domain, produce a strong local depolarization. This local change in voltage would in turn produce a sufficiently strong depolarization to keep reaching the voltage threshold for AP generation during high-frequency repetitive firing, when voltage-gated sodium channels get increasingly inactivated, translating in increasing high AP threshold. Accordingly, the fast voltage-dependent inactivation of T-type channels would then impose a temporal limitation of this high-frequency firing output of mGCs compatible with both the sparse coding model DGGCs activity (Aimone et al., 2011) and the need for them to fire at high frequency to trigger CA3 cells (Henze et al., 2002).

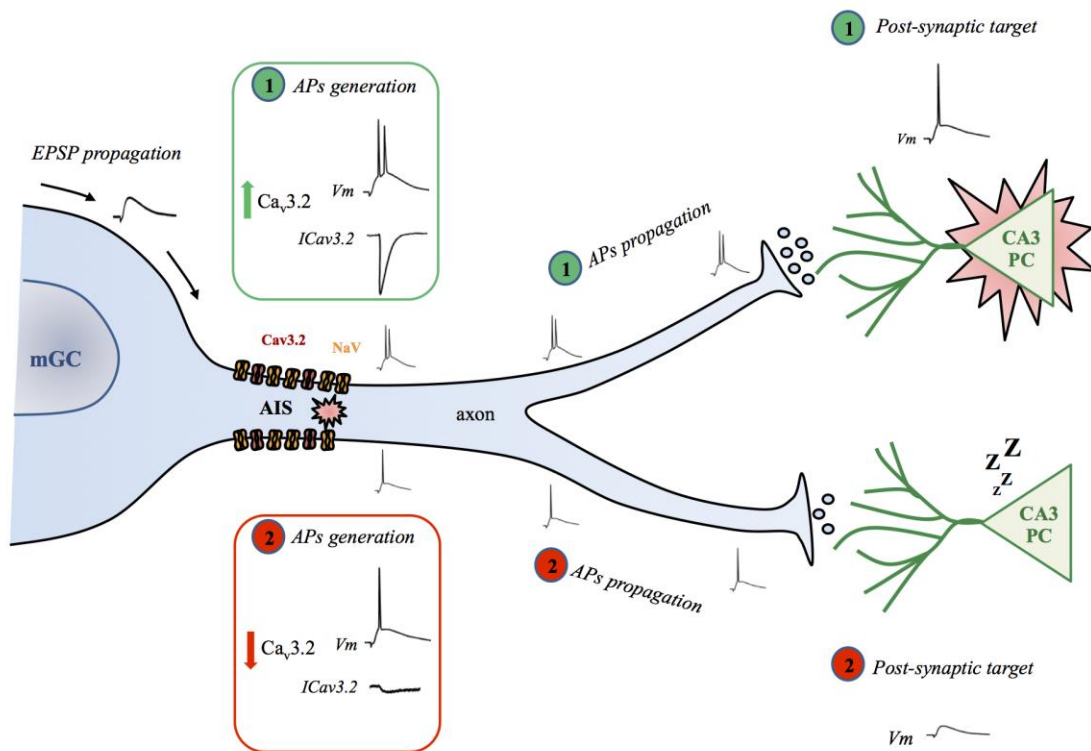


Figure 27: Proposed model of $Ca_v3.2$ channels localized at the level of the axon initial segment of mGCs acting as determining factors of mGC-CA3 pyramidal cells transmission of neuronal activity. In response to limited somatic depolarization underlined by mGCs intrinsic characteristics, the neurons generate different pattern of APs depending on the activity of T-type channels localized at the level of the axon initial segment (AIS), principally the $Ca_v3.2$ isoform. A schematic mGCs is represented sending axonal projections to two different CA3 pyramidal cells to represent two stereotypical conditions of $Ca_v3.2$ channels activity. *Top half and green color-code:* $Ca_v3.2$ current ($ICa_v3.2$) enhances the ability of mGCs to generate APs at high frequency and determines a short time-frame of mGCs activity due to the fast voltage-dependent inactivation of the channels. This in turn can produce sufficiently strong stimulation of the postsynaptic CA3 pyramidal cell (CA3 PC) to trigger its activity while maintaining mGCs overall mostly silent. *Bottom half and red color-code:* Low amounts of $Ca_v3.2$ channels or down-regulation of their activity results in a reduced $ICa_v3.2$ current. As a consequence, mGCs are impaired in their ability to produce this short time-framed repetitive firing of APs at high frequency. This in turn translates in inefficient stimulation of the postsynaptic CA3 PC.

Another possibility is that T-type channels' impact of mGCs burst firing is mediated by their regulatory action on potassium channels localized at the level of the axon initial segment such as it has been demonstrated for M-type channels in the study of Martinello and colleagues (Martinello et al., 2015). T-type channels have been notably shown to interact with BK potassium channels and allow them to activate at low voltages and with fast kinetics (Engbers et al., 2012; Turner and Zamponi, 2014). BK channels are big conductance potassium channels and were reported to control a fast component of AP after-hyperpolarization that supports membrane repolarization during high frequency repetitive firing (Gu et al., 2007; Matthews et al., 2009; Springer et al., 2014). Interestingly, BK channels have been shown to be expressed at the level of the axon initial segment of ferret layer 5 pyramidal cells in

prefrontal cortex (Yu et al., 2010). Experiments with voltage-sensitive dyes and local blockade of BK channels at the level of the axon initial segment could address these questions.

It would also be of great interest to further explore the impact of mGCs' T-type channels and the Ca_v3.2 isoform in regulating DG-CA3 communication and the cognitive processes underlined by the dentate gyrus. Ca_v3.2 has been shown to be expressed more densely in the dendrites of mGCs (Martinello et al., 2015) and I found T-type mediated calcium fluxes in the dendrites, with a possible increasing gradient towards distal dendrites (Figure 12C). In conjunction with our results obtained in freely moving mice (Figure 23 and 24), experiments addressing the impact of mGCs' dendritic T-type channels can shed new light on the somato-dendritic integration of synaptic inputs and corresponding computational processes, similarly to the impact of I_h current in CA1 pyramidal cells (Vaidya and Johnston, 2013). Furthermore, T-type channels can interact with A-type potassium channels of the Kv4 family (Turner and Zamponi, 2014) which have been recently suggested to endow mGCs dendrites with segment-specific plasticity of AP back-propagation and associated calcium signals (Lopez-Rojas et al., 2016). Deepening of our *in vivo* characterization of mGCs and dentate gyrus defects in Ca_v3.2 KO, characterization of the impact of dendritic T-type channels on A-type currents and studying the participation of T-type channels on mGCs membrane resonance properties and integration of synaptic inputs could provide additional information on these topics.

Finally, determining if mGCs burst firing mediated by axon initial segment T-type channels is an intrinsic excitability mechanism that can be regulated by neuromodulation and learning processes is a promising topic of exploration (Bender and Trussell, 2009b; Martinello et al., 2015; Yamada and Kuba, 2016).

5. References

- Aguado, C., García-Madrona, S., Gil-Minguez, M., and Luján, R. (2016). Ontogenic Changes and Differential Localization of T-type Ca²⁺ Channel Subunits Cav3.1 and Cav3.2 in Mouse Hippocampus and Cerebellum. *Front. Neuroanat.* *10*.
- Aimone, J.B., Deng, W., and Gage, F.H. (2011). Resolving New Memories: A Critical Look at the Dentate Gyrus, Adult Neurogenesis, and Pattern Separation. *Neuron* *70*, 589–596.
- Alviña, K., Ellis-Davies, G., and Khodakhah, K. (2009). T-type calcium channels mediate rebound firing in intact deep cerebellar neurons. *Neuroscience* *158*, 635–641.
- Amaral, D.G., Ishizuka, N., and Claiborne, B. (1990). Chapter 1 Chapter Neurons, numbers and the hippocampal network. *Prog. Brain Res.* *83*, 1–11.
- Amaral, D.G., Scharfman, H.E., and Lavenex, P. (2007). The dentate gyrus: fundamental neuroanatomical organization (dentate gyrus for dummies). *Prog. Brain Res.* *163*, 3–22.
- Andersen, P. (2007). *The Hippocampus Book* (Oxford University Press, USA).
- Bakker, A., Kirwan, C.B., Miller, M., and Stark, C.E.L. (2008). Pattern separation in the human hippocampal CA3 and dentate gyrus. *Science* *319*, 1640–1642.
- Beck, H., Steffens, R., Heinemann, U., and Elger, C.E. (1997). Properties of voltage-activated Ca²⁺ currents in acutely isolated human hippocampal granule cells. *J. Neurophysiol.* *77*, 1526–1537.
- Becker, S. (2017). Neurogenesis and pattern separation: time for a divorce. *Wiley Interdiscip. Rev. Cogn. Sci.* *8*.
- Bender, K.J., and Trussell, L.O. (2009a). Axon initial segment Ca²⁺ channels influence action potential generation and timing. *Neuron* *61*, 259–271.
- Bender, K.J., and Trussell, L.O. (2009b). Axon initial segment Ca²⁺ channels influence action potential generation and timing. *Neuron* *61*, 259–271.
- Bender, K.J., and Trussell, L.O. (2012). The physiology of the axon initial segment. *Annu. Rev. Neurosci.* *35*, 249–265.
- Bender, K.J., Ford, C.P., and Trussell, L.O. (2010). Dopaminergic modulation of axon initial segment calcium channels regulates action potential initiation. *Neuron* *68*, 500–511.
- Bender, K.J., Uebele, V.N., Renger, J.J., and Trussell, L.O. (2012). Control of firing patterns through modulation of axon initial segment T-type calcium channels. *J. Physiol.* *590*, 109–118.

- Bernal Sierra, Y.A., Haseleu, J., Kozlenkov, A., Bégay, V., and Lewin, G.R. (2017). Genetic Tracing of Cav3.2 T-Type Calcium Channel Expression in the Peripheral Nervous System. *Front. Mol. Neurosci.* *10*.
- Bernier, B.E., Lacagnina, A.F., Ayoub, A., Shue, F., Zemelman, B.V., Krasne, F.B., and Drew, M.R. (2017). Dentate gyrus contributes to retrieval as well as encoding: Evidence from context fear conditioning, recall, and extinction. *J. Neurosci. Off. J. Soc. Neurosci.*
- Berron, D., Schütze, H., Maass, A., Cardenas-Blanco, A., Kuijf, H.J., Kumaran, D., and Düzel, E. (2016). Strong Evidence for Pattern Separation in Human Dentate Gyrus. *J. Neurosci. Off. J. Soc. Neurosci.* *36*, 7569–7579.
- Bijlenga, P., Liu, J.-H., Espinos, E., Haenggeli, C.-A., Fischer-Lougheed, J., Bader, C.R., and Bernheim, L. (2000). T-type α_1H Ca²⁺ channels are involved in Ca²⁺ signaling during terminal differentiation (fusion) of human myoblasts. *Proc. Natl. Acad. Sci. U. S. A.* *97*, 7627–7632.
- Bikbaev, A., and Manahan-Vaughan, D. (2017). Metabotropic glutamate receptor, mGlu5, regulates hippocampal synaptic plasticity and is required for tetanisation-triggered changes in theta and gamma oscillations. *Neuropharmacology* *115*, 20–29.
- Blaxter, T.J., Carlen, P.L., and Niesen, C. (1989). Pharmacological and anatomical separation of calcium currents in rat dentate granule neurones in vitro. *J. Physiol.* *412*, 93–112.
- Bourinet, E., Stotz, S.C., Spaetgens, R.L., Dayanithi, G., Lemos, J., Nargeot, J., and Zamponi, G.W. (2001). Interaction of SNX482 with domains III and IV inhibits activation gating of alpha(1E) (Ca(V)2.3) calcium channels. *Biophys. J.* *81*, 79–88.
- Bourinet, E., Francois, A., and Laffray, S. (2016). T-type calcium channels in neuropathic pain. *Pain* *157 Suppl 1*, S15-22.
- Bragin, A., Jando, G., Nadasdy, Z., Hetke, J., Wise, K., and Buzsaki, G. (1995). Gamma (40-100 Hz) oscillation in the hippocampus of the behaving rat. *J. Neurosci.* *15*, 47–60.
- Breustedt, J., Vogt, K.E., Miller, R.J., Nicoll, R.A., and Schmitz, D. (2003). α_1E -Containing Ca²⁺ channels are involved in synaptic plasticity. *Proc. Natl. Acad. Sci. U. S. A.* *100*, 12450–12455.
- Brini, M., and Carafoli, E. (2009). Calcium pumps in health and disease. *Physiol. Rev.* *89*, 1341–1378.
- Brogden, R.N., and Markham, A. (1997). Mibefradil. A review of its pharmacodynamic and pharmacokinetic properties, and therapeutic efficacy in the management of hypertension and angina pectoris. *Drugs* *54*, 774–793.

- Buckmaster, P.S., and Dudek, F.E. (1997). Network properties of the dentate gyrus in epileptic rats with hilar neuron loss and granule cell axon reorganization. *J. Neurophysiol.* *77*, 2685–2696.
- Buzsáki, G. (2002). Theta oscillations in the hippocampus. *Neuron* *33*, 325–340.
- Buzsáki, G., and Draguhn, A. (2004). Neuronal oscillations in cortical networks. *Science* *304*, 1926–1929.
- Cameron, H.A., and McKay, R.D. (2001). Adult neurogenesis produces a large pool of new granule cells in the dentate gyrus. *J. Comp. Neurol.* *435*, 406–417.
- Canto, C.B., Wouterlood, F.G., and Witter, M.P. (2008). What Does the Anatomical Organization of the Entorhinal Cortex Tell Us? *Neural Plast.* *2008*.
- Chavez-Colorado, E., Herrera-Carrillo, Z., and Gomora, J.C. (2016). Blocking of T-Type Calcium Channels by TTA-A2 Reveals a Conservative Binding Site for State-Dependent Antagonists. *Biophys. J.* *110*, 439a–440a.
- Chen, C.-C., Lamping, K.G., Nuno, D.W., Barresi, R., Prouty, S.J., Lavoie, J.L., Cribbs, L.L., England, S.K., Sigmund, C.D., Weiss, R.M., et al. (2003). Abnormal coronary function in mice deficient in alpha1H T-type Ca²⁺ channels. *Science* *302*, 1416–1418.
- Chen, C.-C., Shen, J.-W., Chung, N.-C., Min, M.-Y., Cheng, S.-J., and Liu, I.Y. (2012a). Retrieval of Context-Associated Memory is Dependent on the Cav3.2 T-Type Calcium Channel. *PLoS ONE* *7*.
- Chen, C.-C., Shen, J.-W., Chung, N.-C., Min, M.-Y., Cheng, S.-J., and Liu, I.Y. (2012b). Retrieval of Context-Associated Memory is Dependent on the Cav3.2 T-Type Calcium Channel. *PLOS ONE* *7*, e29384.
- Chen, W.-K., Liu, I.Y., Chang, Y.-T., Chen, Y.-C., Chen, C.-C., Yen, C.-T., Shin, H.-S., and Chen, C.-C. (2010). Ca(v)3.2 T-type Ca²⁺ channel-dependent activation of ERK in paraventricular thalamus modulates acid-induced chronic muscle pain. *J. Neurosci. Off. J. Soc. Neurosci.* *30*, 10360–10368.
- Clapham, D.E. (2007). Calcium Signaling. *Cell* *131*, 1047–1058.
- Colgin, L.L., and Moser, E.I. (2010). Gamma oscillations in the hippocampus. *Physiol. Bethesda Md* *25*, 319–329.
- Colgin, L.L., Denninger, T., Fyhn, M., Hafting, T., Bonnevie, T., Jensen, O., Moser, M.-B., and Moser, E.I. (2009). Frequency of gamma oscillations routes flow of information in the hippocampus. *Nature* *462*, 353–357.
- Csicsvari, J., Jamieson, B., Wise, K.D., and Buzsáki, G. (2003). Mechanisms of gamma oscillations in the hippocampus of the behaving rat. *Neuron* *37*, 311–322.

Cui, Y., Liu, X., Yang, T., Mei, Y.-A., and Hu, C. (2014). Exposure to extremely low-frequency electromagnetic fields inhibits T-type calcium channels via AA/LTE4 signaling pathway. *Cell Calcium* 55, 48–58.

Dayer, A.G., Ford, A.A., Cleaver, K.M., Yassaee, M., and Cameron, H.A. (2003). Short-term and long-term survival of new neurons in the rat dentate gyrus. *J. Comp. Neurol.* 460, 563–572.

Deng, W., Aimone, J.B., and Gage, F.H. (2010). New neurons and new memories: how does adult hippocampal neurogenesis affect learning and memory? *Nat. Rev. Neurosci.* 11, 339–350.

Dengler, C.G., and Coulter, D.A. (2016). Normal and epilepsy-associated pathologic function of the dentate gyrus. *Prog. Brain Res.* 226, 155–178.

Dieni, C.V., Nietz, A.K., Panichi, R., Wadiche, J.I., and Overstreet-Wadiche, L. (2013). Distinct Determinants of Sparse Activation during Granule Cell Maturation. *J. Neurosci.* 33, 19131–19142.

Drew, L.J., Fusi, S., and Hen, R. (2013). Adult neurogenesis in the mammalian hippocampus: why the dentate gyrus? *Learn. Mem. Cold Spring Harb. N* 20, 710–729.

Eller, P., Berjukov, S., Wanner, S., Huber, I., Hering, S., Knaus, H.G., Toth, G., Kimball, S.D., and Striessnig, J. (2000). High affinity interaction of mibefradil with voltage-gated calcium and sodium channels. *Br. J. Pharmacol.* 130, 669–677.

Engbers, J.D.T., Anderson, D., Asmara, H., Rehak, R., Mehaffey, W.H., Hameed, S., McKay, B.E., Kruskic, M., Zamponi, G.W., and Turner, R.W. (2012). Intermediate conductance calcium-activated potassium channels modulate summation of parallel fiber input in cerebellar Purkinje cells. *Proc. Natl. Acad. Sci. U. S. A.* 109, 2601–2606.

Espósito, M.S., Piatti, V.C., Laplagne, D.A., Morgenstern, N.A., Ferrari, C.C., Pitossi, F.J., and Schinder, A.F. (2005). Neuronal differentiation in the adult hippocampus recapitulates embryonic development. *J. Neurosci. Off. J. Soc. Neurosci.* 25, 10074–10086.

Fernández, J.A., McGahon, M.K., McGeown, J.G., and Curtis, T.M. (2015). CaV3.1 T-Type Ca²⁺ Channels Contribute to Myogenic Signaling in Rat Retinal Arterioles. *Invest. Ophthalmol. Vis. Sci.* 56, 5125–5132.

Francois, A. (2013). Distributions et fonctions du canal Calcique Cav3.2 dans les voies somatosensorielles (Montpellier 2).

Francois, A., Kerckhove, N., Meleine, M., Alloui, A., Barrere, C., Gelot, A., Uebele, V.N., Renger, J.J., Eschaliere, A., Ardid, D., et al. (2013). State-dependent properties of a new T-type calcium channel blocker enhance Ca(V)3.2 selectivity and support analgesic effects. *Pain* 154, 283–293.

- Gabso, M., Neher, E., and Spira, M.E. (1997). Low mobility of the Ca²⁺ buffers in axons of cultured Aplysia neurons. *Neuron* 18, 473–481.
- Gage, F.H. (2002). Neurogenesis in the Adult Brain. *J. Neurosci.* 22, 612–613.
- Gangarossa, G., Laffray, S., Bourinet, E., and Valjent, E. (2014). T-type calcium channel Cav3.2 deficient mice show elevated anxiety, impaired memory and reduced sensitivity to psychostimulants. *Front. Behav. Neurosci.* 8.
- Ge, S., Yang, C.-H., Hsu, K.-S., Ming, G.-L., and Song, H. (2007a). A critical period for enhanced synaptic plasticity in newly generated neurons of the adult brain. *Neuron* 54, 559–566.
- Ge, S., Yang, C.-H., Hsu, K.-S., Ming, G.-L., and Song, H. (2007b). A critical period for enhanced synaptic plasticity in newly generated neurons of the adult brain. *Neuron* 54, 559–566.
- Ge, S., Sailor, K.A., Ming, G., and Song, H. (2008). Synaptic integration and plasticity of new neurons in the adult hippocampus. *J. Physiol.* 586, 3759–3765.
- Gilbert, P.E., Kesner, R.P., and Lee, I. (2001). Dissociating hippocampal subregions: double dissociation between dentate gyrus and CA1. *Hippocampus* 11, 626–636.
- Gonçalves, J.T., Schafer, S.T., and Gage, F.H. (2016). Adult Neurogenesis in the Hippocampus: From Stem Cells to Behavior. *Cell* 167, 897–914.
- Goodrich-Hunsaker, N.J., Hunsaker, M.R., and Kesner, R.P. (2008). The interactions and dissociations of the dorsal hippocampus subregions: how the dentate gyrus, CA3, and CA1 process spatial information. *Behav. Neurosci.* 122, 16–26.
- Gould, E., Beylin, A., Tanapat, P., Reeves, A., and Shors, T.J. (1999). Learning enhances adult neurogenesis in the hippocampal formation. *Nat. Neurosci.* 2, 260–265.
- Gu, N., Vervaeke, K., and Storm, J.F. (2007). BK potassium channels facilitate high-frequency firing and cause early spike frequency adaptation in rat CA1 hippocampal pyramidal cells. *J. Physiol.* 580, 859–882.
- Gu, Y., Arruda-Carvalho, M., Wang, J., Janoschka, S.R., Josselyn, S.A., Frankland, P.W., and Ge, S. (2012). Optical controlling reveals time-dependent roles for adult-born dentate granule cells. *Nat. Neurosci.* 15, 1700–1706.
- Henze, D.A., Wittner, L., and Buzsáki, G. (2002). Single granule cells reliably discharge targets in the hippocampal CA3 network in vivo. *Nat. Neurosci.* 5, 790–795.
- Huang, L., Keyser, B.M., Tagmose, T.M., Hansen, J.B., Taylor, J.T., Zhuang, H., Zhang, M., Ragsdale, D.S., and Li, M. (2004). NNC 55-0396 [(1S,2S)-2-(2-(N-[(3-benzimidazol-2-yl)propyl]-N-methylamino)ethyl)-6-fluoro-1,2,3,4-tetrahydro-1-

isopropyl-2-naphtyl cyclopropanecarboxylate dihydrochloride]: a new selective inhibitor of T-type calcium channels. *J. Pharmacol. Exp. Ther.* 309, 193–199.

Huang, W., Lu, C., Wu, Y., Ouyang, S., and Chen, Y. (2015). T-type calcium channel antagonists, mibefradil and NNC-55-0396 inhibit cell proliferation and induce cell apoptosis in leukemia cell lines. *J. Exp. Clin. Cancer Res.* CR 34.

Iftinca, M. (2011). Neuronal T-type calcium channels: What's new? Iftinca: T-type channel regulation. *J. Med. Life* 4, 126–138.

Iftinca, M., McKay, B.E., Snutch, T.P., McRory, J.E., Turner, R.W., and Zamponi, G.W. (2006). Temperature dependence of T-type calcium channel gating. *Neuroscience* 142, 1031–1042.

Jensen, M.S., Azouz, R., and Yaari, Y. (1996). Spike after-depolarization and burst generation in adult rat hippocampal CA1 pyramidal cells. *J. Physiol.* 492, 199–210.

Johnston, D., and Narayanan, R. (2008). Active dendrites: colorful wings of the mysterious butterflies. *Trends Neurosci.* 31, 309–316.

Johnston, J., Griffin, S.J., Baker, C., Skrzypiec, A., Chernova, T., and Forsythe, I.D. (2008). Initial segment Kv2.2 channels mediate a slow delayed rectifier and maintain high frequency action potential firing in medial nucleus of the trapezoid body neurons. *J. Physiol.* 586, 3493–3509.

Johnston, S.T., Shtrahman, M., Parylak, S., Gonçalves, J.T., and Gage, F.H. (2016). Paradox of pattern separation and adult neurogenesis: A dual role for new neurons balancing memory resolution and robustness. *Neurobiol. Learn. Mem.* 129, 60–68.

Joksovic, P.M., Bayliss, D.A., and Todorovic, S.M. (2005). Different kinetic properties of two T-type Ca²⁺ currents of rat reticular thalamic neurones and their modulation by enflurane. *J. Physiol.* 566, 125–142.

Jung, M.W., and McNaughton, B.L. (1993). Spatial selectivity of unit activity in the hippocampal granular layer. *Hippocampus* 3, 165–182.

Kang, H.-W., Park, J.-Y., Jeong, S.-W., Kim, J.-A., Moon, H.-J., Perez-Reyes, E., and Lee, J.-H. (2006). A molecular determinant of nickel inhibition in Cav3.2 T-type calcium channels. *J. Biol. Chem.* 281, 4823–4830.

Kelly, T., and Beck, H. (2017). Functional properties of granule cells with hilar basal dendrites in the epileptic dentate gyrus. *Epilepsia* 58, 160–171.

Kempermann, G., Kuhn, H.G., and Gage, F.H. (1997). Genetic influence on neurogenesis in the dentate gyrus of adult mice. *Proc. Natl. Acad. Sci. U. S. A.* 94, 10409–10414.

Kim, D., Song, I., Keum, S., Lee, T., Jeong, M.J., Kim, S.S., McEnery, M.W., and Shin, H.S. (2001). Lack of the burst firing of thalamocortical relay neurons and

resistance to absence seizures in mice lacking alpha(1G) T-type Ca(2+) channels. *Neuron* 31, 35–45.

Kimm, T., and Bean, B.P. (2014). Inhibition of A-Type Potassium Current by the Peptide Toxin SNX-482. *J. Neurosci.* 34, 9182–9189.

Kochlamazashvili, G., Senkov, O., and Dityatev, A. (2012). Extracellular Recordings of Synaptic Plasticity and Network Oscillations in Hippocampal Slices. In *Neuronal Network Analysis*, T. Fellin, and M. Halassa, eds. (Humana Press), pp. 127–147.

Kraus, R.L., Li, Y., Gregan, Y., Gotter, A.L., Uebele, V.N., Fox, S.V., Doran, S.M., Barrow, J.C., Yang, Z.-Q., Reger, T.S., et al. (2010). In vitro characterization of T-type calcium channel antagonist TTA-A2 and in vivo effects on arousal in mice. *J. Pharmacol. Exp. Ther.* 335, 409–417.

Kropff, E., Yang, S.M., and Schinder, A.F. (2015). Dynamic role of adult-born dentate granule cells in memory processing. *Curr. Opin. Neurobiol.* 35, 21–26.

Krueppel, R., Remy, S., and Beck, H. (2011). Dendritic integration in hippocampal dentate granule cells. *Neuron* 71, 512–528.

Laplagne, D.A., Kamienkowski, J.E., Espósito, M.S., Piatti, V.C., Zhao, C., Gage, F.H., and Schinder, A.F. (2007). Similar GABAergic inputs in dentate granule cells born during embryonic and adult neurogenesis. *Eur. J. Neurosci.* 25, 2973–2981.

Lee, I., and Kesner, R.P. (2004). Differential contributions of dorsal hippocampal subregions to memory acquisition and retrieval in contextual fear-conditioning. *Hippocampus* 14, 301–310.

Lee, J.H., Gomora, J.C., Cribbs, L.L., and Perez-Reyes, E. (1999). Nickel block of three cloned T-type calcium channels: low concentrations selectively block alpha1H. *Biophys. J.* 77, 3034–3042.

Li, M., Hansen, J.B., Huang, L., Keyser, B.M., and Taylor, J.T. (2005). Towards selective antagonists of T-type calcium channels: design, characterization and potential applications of NNC 55-0396. *Cardiovasc. Drug Rev.* 23, 173–196.

Lipscombe, D., Helton, T.D., and Xu, W. (2004). L-type calcium channels: the low down. *J. Neurophysiol.* 92, 2633–2641.

Liu, X., Ramirez, S., Pang, P.T., Puryear, C.B., Govindarajan, A., Deisseroth, K., and Tonegawa, S. (2012). Optogenetic stimulation of a hippocampal engram activates fear memory recall. *Nature* 484, 381–385.

Lopez-Rojas, J., and Kreutz, M.R. (2016). Mature granule cells of the dentate gyrus--Passive bystanders or principal performers in hippocampal function? *Neurosci. Biobehav. Rev.* 64, 167–174.

Lopez-Rojas, J., Heine, M., and Kreutz, M.R. (2016). Plasticity of intrinsic excitability in mature granule cells of the dentate gyrus. *Sci. Rep.* 6.

- Lu, C.B., Jefferys, J.G.R., Toescu, E.C., and Vreugdenhil, M. (2011). In vitro hippocampal gamma oscillation power as an index of in vivo CA3 gamma oscillation strength and spatial reference memory. *Neurobiol. Learn. Mem.* 95, 221–230.
- Ly, R., Bouvier, G., Szapiro, G., Prosser, H.M., Randall, A.D., Kano, M., Sakimura, K., Isope, P., Barbour, B., and Feltz, A. (2016). Contribution of postsynaptic T-type calcium channels to parallel fibre-Purkinje cell synaptic responses. *J. Physiol.* 594, 915–936.
- Madroñal, N., Delgado-García, J.M., Fernández-Guizán, A., Chatterjee, J., Köhn, M., Mattucci, C., Jain, A., Tsetsenis, T., Illarionova, A., Grinevich, V., et al. (2016). Rapid erasure of hippocampal memory following inhibition of dentate gyrus granule cells. *Nat. Commun.* 7, 10923.
- Marr, D. (1971). Simple memory: a theory for archicortex. *Philos. Trans. R. Soc. Lond. B. Biol. Sci.* 262, 23–81.
- Martin, R.L., Lee, J.H., Cribbs, L.L., Perez-Reyes, E., and Hanck, D.A. (2000). Mibefradil block of cloned T-type calcium channels. *J. Pharmacol. Exp. Ther.* 295, 302–308.
- Martinello, K., Huang, Z., Lujan, R., Tran, B., Watanabe, M., Cooper, E.C., Brown, D.A., and Shah, M.M. (2015). Cholinergic afferent stimulation induces axonal function plasticity in adult hippocampal granule cells. *Neuron* 85, 346–363.
- Matthews, E.A., Linardakis, J.M., and Disterhoft, J.F. (2009). The fast AHP and the slow AHP are differentially modulated in hippocampal neurons by aging and by learning. *J. Neurosci. Off. J. Soc. Neurosci.* 29, 4750–4755.
- McDonough, S.I., and Bean, B.P. (1998). Mibefradil inhibition of T-type calcium channels in cerebellar purkinje neurons. *Mol. Pharmacol.* 54, 1080–1087.
- McKay, B.E., McRory, J.E., Molineux, M.L., Hamid, J., Snutch, T.P., Zamponi, G.W., and Turner, R.W. (2006). Ca(V)3 T-type calcium channel isoforms differentially distribute to somatic and dendritic compartments in rat central neurons. *Eur. J. Neurosci.* 24, 2581–2594.
- McNulty, M.M., and Hanck, D.A. (2004). State-dependent mibefradil block of Na⁺ channels. *Mol. Pharmacol.* 66, 1652–1661.
- Metz, A.E., Jarsky, T., Martina, M., and Spruston, N. (2005). R-type calcium channels contribute to afterdepolarization and bursting in hippocampal CA1 pyramidal neurons. *J. Neurosci. Off. J. Soc. Neurosci.* 25, 5763–5773.
- Ming, G., and Song, H. (2011). Adult Neurogenesis in the Mammalian Brain: Significant Answers and Significant Questions. *Neuron* 70, 687–702.
- Minge, D., Senkov, O., Kaushik, R., Herde, M.K., Tikhobrazova, O., Wulff, A.B., Mironov, A., van Kuppevelt, T.H., Oosterhof, A., Kochlamazashvili, G., et al. (2017).

Heparan Sulfates Support Pyramidal Cell Excitability, Synaptic Plasticity, and Context Discrimination. *Cereb. Cortex* N. Y. N 1991 *27*, 903–918.

Mongiat, L.A., and Schinder, A.F. (2011). Adult neurogenesis and the plasticity of the dentate gyrus network. *Eur. J. Neurosci.* *33*, 1055–1061.

Mongiat, L.A., Espósito, M.S., Lombardi, G., and Schinder, A.F. (2009). Reliable activation of immature neurons in the adult hippocampus. *PloS One* *4*, e5320.

Montgomery, S.M., Sirota, A., and Buzsáki, G. (2008). Theta and gamma coordination of hippocampal networks during waking and rapid eye movement sleep. *J. Neurosci. Off. J. Soc. Neurosci.* *28*, 6731–6741.

Moreno, C.M., Dixon, R.E., Tajada, S., Yuan, C., Opitz-Araya, X., Binder, M.D., and Santana, L.F. (2016). Ca(2+) entry into neurons is facilitated by cooperative gating of clustered CaV1.3 channels. *eLife* *5*.

Myoga, M.H., and Regehr, W.G. (2011). Calcium microdomains near R-type calcium channels control the induction of presynaptic long-term potentiation at parallel fiber to purkinje cell synapses. *J. Neurosci. Off. J. Soc. Neurosci.* *31*, 5235–5243.

Nakashiba, T., Cushman, J.D., Pelkey, K.A., Renaudineau, S., Buhl, D.L., McHugh, T.J., Rodriguez Barrera, V., Chittajallu, R., Iwamoto, K.S., McBain, C.J., et al. (2012). Young dentate granule cells mediate pattern separation, whereas old granule cells facilitate pattern completion. *Cell* *149*, 188–201.

Nanry, K.P., Mundy, W.R., and Tilson, H.A. (1989). Colchicine-induced alterations of reference memory in rats: role of spatial versus non-spatial task components. *Behav. Brain Res.* *35*, 45–53.

Newcomb, R., Szoke, B., Palma, A., Wang, G., Chen, X. h, Hopkins, W., Cong, R., Miller, J., Urge, L., Tarczy-Hornoch, K., et al. (1998). Selective peptide antagonist of the class E calcium channel from the venom of the tarantula *Hysterocrates gigas*. *Biochemistry (Mosc.)* *37*, 15353–15362.

Ninkovic, J., Mori, T., and Götz, M. (2007). Distinct modes of neuron addition in adult mouse neurogenesis. *J. Neurosci. Off. J. Soc. Neurosci.* *27*, 10906–10911.

Obejero-Paz, C.A., Gray, I.P., and Jones, S.W. (2008). Ni²⁺ Block of CaV3.1 (α 1G) T-type Calcium Channels. *J. Gen. Physiol.* *132*, 239–250.

Overstreet-Wadiche, L.S., Bensen, A.L., and Westbrook, G.L. (2006). Delayed development of adult-generated granule cells in dentate gyrus. *J. Neurosci. Off. J. Soc. Neurosci.* *26*, 2326–2334.

Paxinos, G., and Franklin, K.B.J. (2012). Paxinos and Franklin's the Mouse Brain in Stereotaxic Coordinates, Fourth Edition (Amsterdam: Academic Press).

Paz, J.T., and Huguenard, J.R. (2015). Microcircuits and their interactions in epilepsy: is the focus out of focus? *Nat. Neurosci.* *18*, 351–359.

- Pedroni, A., Minh, D.D., Mallamaci, A., and Cherubini, E. (2014). Electrophysiological characterization of granule cells in the dentate gyrus immediately after birth. *Front. Cell. Neurosci.* *8*.
- Perez-Reyes, E. (2003). Molecular physiology of low-voltage-activated t-type calcium channels. *Physiol. Rev.* *83*, 117–161.
- Pernía-Andrade, A.J., and Jonas, P. (2014). Theta-Gamma-Modulated Synaptic Currents in Hippocampal Granule Cells In Vivo Define a Mechanism for Network Oscillations. *Neuron* *81*, 140–152.
- Pourbadie, H.G., Naderi, N., Delavar, H.M., Hosseinzadeh, M., Mehranfard, N., Khodaghali, F., Janahmadi, M., and Motamedi, F. (2017). Decrease of high voltage Ca(2+) currents in the dentate gyrus granule cells by entorhinal amyloidopathy is reversed by calcium channel blockade. *Eur. J. Pharmacol.* *794*, 154–161.
- Ramirez, S., Liu, X., Lin, P.-A., Suh, J., Pignatelli, M., Redondo, R.L., Ryan, T.J., and Tonegawa, S. (2013). Creating a false memory in the hippocampus. *Science* *341*, 387–391.
- Rangel, L.M., Alexander, A.S., Aimone, J.B., Wiles, J., Gage, F.H., Chiba, A.A., and Quinn, L.K. (2014). Temporally selective contextual encoding in the dentate gyrus of the hippocampus. *Nat. Commun.* *5*, ncomms4181.
- Sabatini, B.L., Oertner, T.G., and Svoboda, K. (2002). The life cycle of Ca(2+) ions in dendritic spines. *Neuron* *33*, 439–452.
- Scharfman, H.E. (2011). *The Dentate Gyrus: A Comprehensive Guide to Structure, Function, and Clinical Implications* (Elsevier).
- Scharfman, H.E. (2016). The enigmatic mossy cell of the dentate gyrus. *Nat. Rev. Neurosci.* *17*, 562–575.
- Scharfman, H., Goodman, J., and McCloskey, D. (2007). Ectopic granule cells of the rat dentate gyrus. *Dev. Neurosci.* *29*, 14–27.
- Scharfman, H.E., Sollas, A.L., Berger, R.E., and Goodman, J.H. (2003). Electrophysiological evidence of monosynaptic excitatory transmission between granule cells after seizure-induced mossy fiber sprouting. *J. Neurophysiol.* *90*, 2536–2547.
- Schmidt, B., Marrone, D.F., and Markus, E.J. (2012). Disambiguating the similar: The dentate gyrus and pattern separation. *Behav. Brain Res.* *226*, 56–65.
- Schmidt-Hieber, C., and Bischofberger, J. (2010). Fast sodium channel gating supports localized and efficient axonal action potential initiation. *J. Neurosci. Off. J. Soc. Neurosci.* *30*, 10233–10242.
- Schmidt-Hieber, C., Jonas, P., and Bischofberger, J. (2004a). Enhanced synaptic plasticity in newly generated granule cells of the adult hippocampus. *Nature* *429*, 184–187.

- Schmidt-Hieber, C., Jonas, P., and Bischofberger, J. (2004b). Enhanced synaptic plasticity in newly generated granule cells of the adult hippocampus. *Nature* 429, 184–187.
- Senkov, O., Sun, M., Weinhold, B., Gerardy-Schahn, R., Schachner, M., and Dityatev, A. (2006). Polysialylated neural cell adhesion molecule is involved in induction of long-term potentiation and memory acquisition and consolidation in a fear-conditioning paradigm. *J. Neurosci. Off. J. Soc. Neurosci.* 26, 10888–10989.
- Senkov, O., Mironov, A., and Dityatev, A. (2015). A novel versatile hybrid infusion-multielectrode recording (HIME) system for acute drug delivery and multisite acquisition of neuronal activity in freely moving mice. *Front. Neurosci.* 9, 425.
- Senkov, O., Mironov, A., and Dityatev, A. (2016). An Advanced 3D Printed Design of the Hybrid Infusion-Multielectrode Recording System for Local Field Potential and Single Unit Acquisition and Intrabrain Drug Delivery in Freely Moving Mice. *Med. Technol. Med. Tehnol. V Med.* 8.
- Shao, L.-R., and Dudek, F.E. (2011). Repetitive perforant-path stimulation induces epileptiform bursts in minislices of dentate gyrus from rats with kainate-induced epilepsy. *J. Neurophysiol.* 105, 522–527.
- Shen, J.-B., Jiang, B., and Pappano, A.J. (2000). Comparison of L-Type Calcium Channel Blockade by Nifedipine and/or Cadmium in Guinea Pig Ventricular Myocytes. *J. Pharmacol. Exp. Ther.* 294, 562–570.
- Sierra, A., Encinas, J.M., Deudero, J.J.P., Chancey, J.H., Enikolopov, G., Overstreet-Wadiche, L.S., Tsirka, S.E., and Maletic-Savatic, M. (2010). Microglia shape adult hippocampal neurogenesis through apoptosis-coupled phagocytosis. *Cell Stem Cell* 7, 483–495.
- Snyder, J.S., Kee, N., and Wojtowicz, J.M. (2001). Effects of adult neurogenesis on synaptic plasticity in the rat dentate gyrus. *J. Neurophysiol.* 85, 2423–2431.
- Sochivko, D., Pereverzev, A., Smyth, N., Gissel, C., Schneider, T., and Beck, H. (2002). The CaV2.3 Ca²⁺ channel subunit contributes to R-Type Ca²⁺ currents in murine hippocampal and neocortical neurones. *J. Physiol.* 542, 699–710.
- Springer, S.J., Burkett, B.J., and Schrader, L.A. (2014). Modulation of BK channels contributes to activity-dependent increase of excitability through MTORC1 activity in CA1 pyramidal cells of mouse hippocampus. *Front. Cell. Neurosci.* 8, 451.
- Stocca, G., Schmidt-Hieber, C., and Bischofberger, J. (2008). Differential dendritic Ca²⁺ signalling in young and mature hippocampal granule cells. *J. Physiol.* 586, 3795–3811.

- Strege, P.R., Bernard, C.E., Ou, Y., Gibbons, S.J., and Farrugia, G. (2005). Effect of mibefradil on sodium and calcium currents. *Am. J. Physiol. Gastrointest. Liver Physiol.* *289*, G249-253.
- Sutherland, R.J., Whishaw, I.Q., and Kolb, B. (1983). A behavioural analysis of spatial localization following electrolytic, kainate- or colchicine-induced damage to the hippocampal formation in the rat. *Behav. Brain Res.* *7*, 133–153.
- Talley, E.M., Cribbs, L.L., Lee, J.H., Daud, A., Perez-Reyes, E., and Bayliss, D.A. (1999). Differential distribution of three members of a gene family encoding low voltage-activated (T-type) calcium channels. *J. Neurosci. Off. J. Soc. Neurosci.* *19*, 1895–1911.
- Temprana, S.G., Mongiat, L.A., Yang, S.M., Trincherio, M.F., Alvarez, D.D., Kropff, E., Giacomini, D., Beltramone, N., Lanuza, G.M., and Schinder, A.F. (2015). Delayed Coupling to Feedback Inhibition during a Critical Period for the Integration of Adult-Born Granule Cells. *Neuron* *85*, 116–130.
- Todorovic, S.M., and Jevtovic-Todorovic, V. (2011). T-type voltage-gated calcium channels as targets for the development of novel pain therapies. *Br. J. Pharmacol.* *163*, 484–495.
- Todorovic, S.M., Jevtovic-Todorovic, V., Meyenburg, A., Mennerick, S., Perez-Reyes, E., Romano, C., Olney, J.W., and Zorumski, C.F. (2001). Redox modulation of T-type calcium channels in rat peripheral nociceptors. *Neuron* *31*, 75–85.
- Toni, N., and Schinder, A.F. (2015). Maturation and Functional Integration of New Granule Cells into the Adult Hippocampus. *Cold Spring Harb. Perspect. Biol.* *8*, a018903.
- Treves, A., Tashiro, A., Witter, M.P., and Moser, E.I. (2008). What is the mammalian dentate gyrus good for? *Neuroscience* *154*, 1155–1172.
- Tsien, R.W., and Barrett, C.F. (2013). *A Brief History of Calcium Channel Discovery* (Landes Bioscience).
- Turner, R.W., and Zamponi, G.W. (2014). T-type channels buddy up. *Pflugers Arch.* *466*, 661–675.
- Urban, N.N., Henze, D.A., and Barrionuevo, G. (1998). Amplification of perforant-path EPSPs in CA3 pyramidal cells by LVA calcium and sodium channels. *J. Neurophysiol.* *80*, 1558–1561.
- Vaidya, S.P., and Johnston, D. (2013). Temporal synchrony and gamma-to-theta power conversion in the dendrites of CA1 pyramidal neurons. *Nat. Neurosci.* *16*, 1812–1820.
- Walsh, T.J., Schulz, D.W., Tilson, H.A., and Schmechel, D.E. (1986). Colchicine-induced granule cell loss in rat hippocampus: selective behavioral and histological alterations. *Brain Res.* *398*, 23–36.

- Wang, G., Dayanithi, G., Newcomb, R., and Lemos, J.R. (1999). An R-type Ca(2+) current in neurohypophysial terminals preferentially regulates oxytocin secretion. *J. Neurosci. Off. J. Soc. Neurosci.* *19*, 9235–9241.
- Wang, S., Scott, B.W., and Wojtowicz, J.M. (2000). Heterogenous properties of dentate granule neurons in the adult rat. *J. Neurobiol.* *42*, 248–257.
- Weiss, N., and Zamponi, G.W. (2013). Control of low-threshold exocytosis by T-type calcium channels. *Biochim. Biophys. Acta BBA - Biomembr.* *1828*, 1579–1586.
- Wormuth, C., Lundt, A., Henseler, C., Müller, R., Broich, K., Papazoglou, A., and Weiergräber, M. (2016). Review: Cav2.3 R-type Voltage-Gated Ca²⁺ Channels - Functional Implications in Convulsive and Non-convulsive Seizure Activity. *Open Neurol. J.* *10*, 99–126.
- Wu, K., and Leung, L.S. (1998). Monosynaptic activation of CA3 by the medial perforant path. *Brain Res.* *797*, 35–41.
- Wu, S., Zhang, M., Vest, P.A., Bhattacharjee, A., Liu, L., and Li, M. (2000). A mibefradil metabolite is a potent intracellular blocker of L-type Ca(2+) currents in pancreatic beta-cells. *J. Pharmacol. Exp. Ther.* *292*, 939–943.
- Yamada, R., and Kuba, H. (2016). Structural and Functional Plasticity at the Axon Initial Segment. *Front. Cell. Neurosci.* *10*, 250.
- Yamamoto, Y., Fukuta, H., and Suzuki, H. (1993). Blockade of sodium channels by divalent cations in rat gastric smooth muscle. *Jpn. J. Physiol.* *43*, 785–796.
- Yasuda, R., Nimchinsky, E.A., Scheuss, V., Pologruto, T.A., Oertner, T.G., Sabatini, B.L., and Svoboda, K. (2004). Imaging calcium concentration dynamics in small neuronal compartments. *Sci. STKE Signal Transduct. Knowl. Environ.* *2004*, pl5.
- Yu, Y., Maureira, C., Liu, X., and McCormick, D. (2010). P/Q And N Channels Control Baseline and Spike-Triggered Calcium Levels in Neocortical Axons And Synaptic Boutons. *J. Neurosci. Off. J. Soc. Neurosci.* *30*, 11858–11869.
- Zamponi, G.W., Bourinet, E., and Snutch, T.P. (1996). Nickel block of a family of neuronal calcium channels: subtype- and subunit-dependent action at multiple sites. *J. Membr. Biol.* *151*, 77–90.
- Zhan, X.J., Cox, C.L., Rinzel, J., and Sherman, S.M. (1999). Current clamp and modeling studies of low-threshold calcium spikes in cells of the cat's lateral geniculate nucleus. *J. Neurophysiol.* *81*, 2360–2373.
- Zhang, X., Velumian, A.A., Jones, O.T., and Carlen, P.L. (2000). Modulation of high-voltage-activated calcium channels in dentate granule cells by topiramate. *Epilepsia* *41 Suppl 1*, S52-60.

Zhang, Y., Bekku, Y., Dzhashiashvili, Y., Armenti, S., Meng, X., Sasaki, Y., Milbrandt, J., and Salzer, J.L. (2012). Assembly and maintenance of nodes of ranvier rely on distinct sources of proteins and targeting mechanisms. *Neuron* 73, 92–107.

Zhou, Z., and January, C.T. (1998). Both T- and L-type Ca²⁺ channels can contribute to excitation-contraction coupling in cardiac Purkinje cells. *Biophys. J.* 74, 1830–1839.

6. Abbreviations

3D	Three-dimensional
ADP	After-depolarization
AIS	Axon initial segment
AP	Action potential
CA1	Cornu Ammonis 1 subfield of the hippocampus
CA3	Cornu Ammonis 3 subfield of the hippocampus
CA3 PC	CA3 pyramidal cell
Cav	Voltage-gated calcium channel
Ca _v 3	T-type, low-voltage activated family of voltage-gated calcium channels
Ca _v 3.1-3	The three different isoforms composing the T-type channels family
Ca _v 3.2 KO	Ca _v 3.2 Knockout
CC+	Negatively reinforced conditioning context
CC-	Neutral conditioning context
CTR	Control
DG	Dentate gyrus
DGGC	Dentate gyrus granule cell
DMSO	Dimethyl sulfoxide
DZNE	Deutsches zentrum für neurodegenerative erkrankungen
E-S	EPSP slope versus Spike probability
E50 _{slope}	Half-maximal effective EPSP slope
EC	Entorhinal cortex
EPSP	Excitatory post-synaptic potential
FFT	Fast Fourier transform
GABA	<i>Gamma</i> -Aminobutyric acid
GCL	Granule cell layer
HIL	Hilus
HVA	High voltage-activated
Hz	Hertz
ICa _v 3.2	Current underlined by Ca _v 3.2 isoform of T-type channel
iGC	Immature granule cell
IML	Inner molecular layer
ISI	Inter-spike interval
LFP	Local field potential
LIN	Leibniz institute für Neurobiologie
LTS	Low-treshold spike
LVA	Low voltage-activated
mA	Milliampère

mGC	Mature granule cell
min	Minute
mM	Millimolar
MML	Middle molecular layer
MPP	Medial perforant path
ms	Millisecond
mV	Millivolt
MΩ	Megaohm
nM	Nanomolar
ns	Non-significant
OML	Outer molecular layer
pA	Picoampère
R+0	Rheobase current / depolarizing stimulation
R+1	Current / depolarizing stimulation equal to rheobase plus 40 pA
s	Second
s.e.m.	Standard error of the mean
SGZ	Sub-granular zone
TTX	Tetrodotoxin
WT	Wild type
γ	<i>Gamma</i> oscillatory activity frequency range (30-100 Hertz)
θ	<i>Theta</i> oscillatory activity frequency range (5-12 Hertz)
μm	Micrometer
μM	Micromolar

Curriculum Vitae

Personal information:

Name: Maël Florent Duménieu
Date of birth: 21/04/1989
Place of birth: Le Creusot, France
Nationality: French

Education:

- 2013-current: **Doctoral student.** Department of Neurochemistry and Molecular Biology. Research group Neuroplasticity, research group Molecular Physiology, Leibniz Institute for Neurobiology. Otto Von-Guericke University. Magdeburg, Germany.
- 2011-2013: **M.Sc. Physiology and Neurosciences.** Claude Bernard University Lyon I, Lyon, France.
- 2007-2011: **B.Sc. Biology and Physiology.** Claude Bernard University Lyon I, Lyon, France.
- 2007: **High School Diploma.** “Baccalauréat scientifique”. Lycée professionnel Joseph Marie Carriat, Bourg-en-Bresse, France.

Fellowships:

Ph.D. fellowship granted by the Leibniz Institute for Neurobiology, Magdeburg, Germany, from September 2013 to September 2017, under supervision of Jeffrey Lopez-Rojas, research group Neuroplasticity; and Arthur Bikbaev, research group Molecular physiology.

M.Sc. Scholarship granted by the Lyon Neurosciences Center from January 2013 to June 2013, under the supervision of Nicola Kuczewski and Brigitte Palouzier-Paulignan, research group Olfactory coding and memory.

Scientific publications:

- 1) **Duménieu, M., Oulé, M., Kreutz, M.R., and Lopez-Rojas, J. (2017).** “The Segregated Expression of Voltage-Gated Potassium and Sodium Channels in Neuronal Membranes: Functional Implications and Regulatory Mechanisms.” **Frontiers in Cellular Neuroscience. 11**, 115. DOI: 10.3389/fncel.2017.00115
- 2) **Bikbaev, A., Duménieu, M., Lopez-Rojas, J., and Heine, M. (2016).** “Localizing Receptors and Channels Across the Dendritic Arbour.” In **Dendrites**, K. Emoto, R. Wong, E. Huang, and C. Hoogenraad, eds. (Springer Japan), pp. 387–424.
- 3) **Duménieu, M., Fourcaud-Trocmé, N., Garcia, S., and Kuczewski, N. (2015).** “Afterhyperpolarization (AHP) regulates the frequency and timing of action potentials in the mitral cells of the olfactory bulb: role of olfactory experience.” **Physiological Reports 3**. DOI: 10.14814/phy2.12344

Selbstständigkeitserklärung

Hiermit erkläre ich, dass ich die von mir eingereichte Dissertation zu dem Thema **“Ca_v3.2 T-type calcium channels modulate burst firing of mature granule cells of the dentate gyrus”** selbständig verfasst, nicht schon als Dissertation verwendet habe und die benutzten Hilfsmittel und Quellen vollständig angegeben wurden.

Weiterhin erkläre ich, dass ich weder diese noch eine andere Arbeit zur Erlangung des akademischen Grades doctor rerum naturalium (Dr. rer. Nat.) an anderen Einrichtungen eingereicht habe.

(Ort, Datum)

(Maël Florent Duménieu)